Near-Field Radiative Thermal Transport and Energy Conversion

by

Anthony Fiorino

A dissertation submitted in partial fulfillment
of the requirements for the degree of
Doctor of Philosophy
(Mechanical Engineering)
in the University of Michigan
2018

Doctoral Committee:

Professor Edgar Meyhofer, Co-Chair
Associate Professor Pramod Sangi Reddy, Co-Chair
Professor Stephen Forrest
Assistant Professor Andrej Lenert
Assistant Professor Xiaogan Liang

Anthony Fiorino

fiorino@umich.edu

ORCID iD: 0000-0001-7823-6898

Acknowledgments

First, I wish to thank Professors Pramod Reddy and Edgar Meyhofer, who served as co-advisors of my graduate work here at the University of Michigan, for their intellectual and moral support, and for suggesting an interesting and challenging research topic. I also wish to thank those professors who served on my dissertation committee, namely Professors Stephen Forrest, Andrej Lenert, and Xiaogan Liang, for their guidance and wisdom.

Further, I am grateful to my colleagues here at Michigan for their contributions to the work I describe in this dissertation. In particular, I will mention Dakotah Thompson and Linxiao Zhu for their contributions not only to my experiments, but to my approach to research in general. Their specific contributions are too numerous to name here, and while I try throughout this document to credit them where appropriate, I am certain that I cannot convey how essential they have been to my research progress. I also wish to thank Rohith Mittapally for his part in fabricating the microscale devices described in chapters 3 and 4. Finally, although they have each since graduated and moved on from the University of Michigan, I do wish to thank Bai Song, Yashar Ganjeh, and Behzad Sadat for laying the groundwork for my own research.

Next, I wish to acknowledge my collaborators overseas for their contributions to my work. Odile Bezencenet, Nadia El-Bondry, and Shailendra Banspropun provided the VO_2 samples for the work I describe in chapter 4, and Svend-Age Biehs and Philippe Ben-Abdallah performed the computational modeling for the same. I owe them my gratitude.

I received financial support from the Department of Mechanical Engineering (1 year), from the National Science Foundation Graduate Research Fellowship Program (3 years), and from the Rackham Graduate School Predoctoral Fellowship (1 year). I am grateful for their support.

Finally, I wish to thank a number of people in my personal life. I thank my parents, Bob and Lori Fiorino, for affording me the opportunities that have enabled me to get to this point. I thank my wife, Kelly Fiorino, for her love, patience, and moral support. And I thank my aunt, Mary Jo DiCristofaro, an Ohio State alumnus whose distaste for all things Michigan is outweighed only by her love for her nephews and, apparently, her enthusiasm for “nanos.”

Table of Contents

List of Figures

Abstract

Thermal radiation occurs when electromagnetic energy is emitted from one body and absorbed by another body. The net energy transferred between bodies, called radiative heat transfer, is well-understood when the distance between them is large compared to the wavelength of the electromagnetic waves. However, a question of fundamental interest is: what happens when the distance between the radiating bodies is smaller than or comparable to the wavelength of the radiation? That is, what happens when the bodies are brought into the "near-field?" Countless theoretical treatments now exist in the literature indicating that the radiative heat transfer can increase by orders of magnitude when the spacing between bodies is reduced to tens or hundreds of nanometers, and these predictions are largely supported by a handful of experimental studies. Moreover, computational work suggests that near-field radiation between parallel plates can have important, novel applications. However, their realization has thus far been prohibited by the technical difficulty in positioning parallel plates across nanoscale gaps.

My first research objective was to measure near-field radiative heat transfer between parallel plates separated by less than a single micrometer, a goal which had eluded researchers for nearly half a century. Using a pair of microscale devices and a custom-built nanopositioner, we systematically demonstrated heat flux enhancements of 100-fold compared to the far-field by decreasing the inter-plate distance between parallel silica plates from 10 μm to approximately 60 nm. I then modified this approach to utilize a single planar microdevice situated across a vacuum gap from a macroscopic planar surface. By using devices with lesser curvature and higher

mechanical stiffness, I reduced the minimum attainable gap size between silica plates to approximately 25 nanometers and measured a near-field heat flow 1,200 times higher than that of the far field, representing a significant improvement over the previous demonstration. Most importantly, replacing one of the microdevices with a macroscopic surface enabled a greater degree of flexibility in materials processing, opening up new opportunities for novel measurements.

My second objective was to use this new technique to demonstrate novel near-field-enabled thermal diode using a doped silicon microdevice and an extended vanadium dioxide thin film. Because the emissive and absorptive properties of vanadium dioxide change dramatically when it undergoes an insulator-metal transition at 68 degrees Celsius, the radiative heat flow can change depending on the direction of the temperature difference. For a vacuum gap size of approximately 140 nanometers, I measured that the heat flow from metallic vanadium dioxide to doped silicon exceeds the heat flow from doped silicon to insulating vanadium dioxide by a factor of approximately two. Computational modeling showed that this rectification could be further improved by decreasing the thickness of the vanadium dioxide film.

Finally, I demonstrated the first near-field power output enhancement in a thermophotovoltaic system. For a doped silicon emitter at 655 kelvin radiating at an indium arsenide-based cell, I measured a 40-fold increase in the electrical output power from the cell by reducing the vacuum gap spacing from 10 micrometers to approximately 60 nanometers. Additional experiments were carried out with a cell having a different bandgap energy, and its performance was compared to the first cell. Moreover, a detailed mathematical model was developed to identify ways to improve the device efficiency in the future. These studies represent an important milestone in near-field-enabled energy conversion.

Chapter 1: Near-Field Radiative Thermal Transport: From Theory to Experiment

Sections 1.1 through 1.7 are reproduced with permission from *AIP Advances*. See Ref.[1]

Bai Song, Anthony Fiorino, Edgar Meyhofer, and Pramod Reddy

Section 1.8 is reproduced with permission from *Nature Nanotechnology*. See Ref.[2]

Bai Song, Dakotah Thompson, Anthony Fiorino, Yashar Ganjeh, Pramod Reddy, and Edgar Meyhofer

1.1 Introduction

Thermal radiation is universal to all objects at non-zero absolute temperatures as electromagnetic radiative emissions necessarily accompany thermally driven random motions of electric charges. Historically, rudimentary yet at times intensive inquiries into the nature of radiant heat transfer between macroscopic bodies and its governing laws spanned hundreds of years.[3] These efforts were greatly boosted by William Hershel's discovery of the infrared in 1800[4-6] and ultimately culminated in Max Planck's law of blackbody radiation at the turn of the 20th century.[7-9] Quantum physics largely originated from the efforts of Planck and his

contemporaries to better understand experimental results on blackbody radiation,[10-12] and in return helped in the establishment of a more general and advanced theory of thermal radiation. The quantum mechanical derivation of various fluctuation-dissipation theorems (FDT),[13-16] and more importantly the formulation of Sergei M. Rytov's fluctuational electrodynamics around the early 1950s,[17, 18] allowed for the first time direct and detailed mathematical descriptions that related thermal radiation to its origin in the random fluctuations of charges, which represented a significant step beyond discussions of equilibrium distribution of radiation from unspecified sources.

Further, the need for better insulation at cryogenic temperatures[19] and the rapid development of technologies at the micrometer scale created an emerging need to understand thermal radiation in systems with length scales comparable to or smaller than the peak radiation wavelength. In this regime, two effects become important:[20-29] First, the interference of electromagnetic waves causes discernible differences in radiative heat transfer. Second, the evanescent contributions to heat transfer become dominant (Fig. 1.1a, b). The near-field outside an object is a natural extension of the electromagnetic field inside, as demanded by the continuity of field amplitudes across an interface.[30] For evanescent waves, the amplitude of the fields decays exponentially with increasing distance from the interface. However, when the spatial separation between surfaces is small (i.e. they are in the near-field of each other) there is a dramatic increase in energy density and flow due to evanescent contributions.[20-29] The description of near-field radiation requires ideas and concepts that go beyond those required for far-field radiation. In terms of applications, near-field radiative heat transfer (NFRHT) is expected to be key to developing novel technologies such as thermal lithography,[20] coherent thermal sources,[31-38] scanning thermal microscopy,[39-41] heat-assisted magnetic recording,[42-44]

advanced thermal management and thermal logic devices,[45-67] as well as thermophotovoltaic[68-80] and other[81-84] energy conversion devices.

1.2 Planck's Law of Blackbody Radiation

Planck's law of blackbody thermal radiation describes the spectral energy density of electromagnetic radiation $u_{\mathrm{BB},\lambda}(T)$ in a cavity in thermal equilibrium and was first presented by Planck[7] at the German Physical Society meeting in October 1900 as

$$u_{\mathrm{BB},\lambda}(T) = \frac{C_1 \lambda^{-5}}{e^{\frac{C_2}{\lambda T}} - 1}, \tag{1.1}$$

where λ is the free space wavelength, T is the absolute temperature, while C_1 and C_2 denote empirical fitting constants. A large enclosed opaque cavity that features a tiny hole is an excellent practical realization of an all-absorbing blackbody, as light entering the hole is either reflected indefinitely or absorbed in the cavity and is unlikely to re-emerge. Consequently, discussions of blackbody radiation frequently refer to the idea of a cavity. Planck derived the relation given in Eqn. 1.1 using his deterministic concept of oscillator entropy, but also considered it "eine glücklich erratene Interpolationsformel", that is, a lucky guessed interpolation. It seamlessly bridges Wien's formula effective at short wavelengths and that of Lord Rayleigh valid only at long wavelengths, and is in excellent agreement with experimental data across the spectrum. Soon afterwards, as a determined effort to go beyond his inspired first guess and reveal more fundamental physics, Planck reluctantly turned to Boltzmann's probabilistic picture of entropy.[12] Only about two months later, in December 1900 and again to the German Physical Society, Planck[8] presented his new derivation and expression:

$$u_{\mathrm{BB},\nu}(T) = \frac{8\pi h_{\mathrm{p}} \nu^3}{c^3} \frac{1}{e^{\frac{h_{\mathrm{p}}\nu}{k_{\mathrm{B}}T}} - 1}, \tag{1.2}$$

where ν is the frequency, and the empirical fitting constants have been superseded by what are now known as three of the most important fundamental physical constants, i.e., the free space speed of light c, the Boltzmann constant k_{B} and most importantly the constant h_{P}, which was explicitly introduced for the first time by Planck, with a proposed value of 6.55×10^{-27} erg sec. Despite the many and more advanced derivations and interpretations that came about thereafter, Planck's law in the form of Eqn. 1.2 has since withstood the test of time. And more profoundly, this seminal work has been widely credited as having initiated the quantum era.[10-12]

Planck's law is of fundamental importance to the study of radiative heat transport between many bodies in addition to thermal radiation from isolated objects. It depicts a broadband emission spectrum, which implies temporal incoherence. Also, the spatial coherence of thermal radiation has traditionally been considered poor due to its origin in the random currents distributed throughout the volume of an object. Variations of Eqn. 1.2 that express the spectral energy density in terms of wavelength λ or wavenumber η are also used. Apart from the energy density, the closely-related spectral emissive power has been frequently discussed. With respect to the wavelength, the hemispherical spectral emissive power (energy emitted into a half-space per unit time per unit area per unit wavelength at a given wavelength) of a blackbody $E_{\mathrm{BB},\lambda}$ is related to the spectral energy density via $E_{\mathrm{BB},\lambda} = cu_{\mathrm{BB},\lambda}/4$,[11, 85] where $u_{\mathrm{BB},\lambda}$ is the wavelength representation of Eqn. 1.2. As illustrated in Fig. 1.1c, the Planck spectrum features a maximum spectral emissive power at a temperature-dependent wavelength. One can derive from $E_{\mathrm{BB},\lambda}$ that for any given temperature T, the peak wavelength is given by $\lambda_{\mathrm{BB,max}} \cong 2900/T$ (μm). This relationship is historically called the Wien's displacement law[85] and at room temperature (~300

K), the peak wavelength is about 10 μm. Further, Planck's law naturally leads to the Stefan-Boltzmann law[85] which states that the total emissive power of a blackbody E_{BB} is proportional to T^4, with a proportionality constant σ given by $\sigma = 2\pi^5 k_B^4 / 15c^2h^3 \approx 5.67\times10^{-8}\ \mathrm{W m^{-2} K^{-4}}$. In deriving this equation one simply integrates $E_{BB,\lambda}$ over all wavelengths and shows that the total emissive power of a blackbody is indeed $E_{BB,\lambda} = \sigma T^4$. For a real object the spectral emissive power is usually written as $E_\lambda = e_\lambda E_{BB,\lambda}$ where e_λ is its emissivity at a wavelength of λ and $e_\lambda \in [0,1]$. Consequently, the Stefan-Boltzmann law was considered to represent the maximum emissive power (frequently referred to as the blackbody limit) that is possible for any object at temperature *T*. Also, note that only the object's temperature and material properties are involved, and no dependence on any spatial separation is present. As outlined above, the Wien's displacement law and Stefan-Boltzmann law are direct consequences of Planck's law, and together they provide the foundation for far-field radiative heat transfer theories.[85, 86]

Nevertheless, Planck's law is not without limitations. As pointed out by Planck himself in his book on the Theory of Heat Radiation,[9] the spectrum as given by Eqn. 1.2 and consequently the Wien's displacement law and Stefan-Boltzmann law, are only valid when all relevant spatial length scales are much larger than the peak wavelengths. The effect of this underlying assumption on thermal radiation seems to have been noted first by Bijl[87] in the context of small cavities at cryogenic temperatures. Specifically, it was highlighted that at very low temperatures, where the characteristic wavelength of thermal radiation becomes comparable to the size of the cavity, classical far-field radiative heat transfer theories would fail to adequately describe heat transfer via radiation. The failure of radiative heat transfer theories at smaller length scales attracted very little attention for many decades, possibly due to lack of theoretical and technical

relevance. Indeed, this situation remained true for a good portion of the 20th century, until around the 1950s.

1.3 Radiation between Closely Spaced Bodies

One may speculate that the desire and necessity to go beyond Planck's law and to inquire into various size effects in thermal radiation became increasingly tangible on two fronts. Theoretically, progress in the study of proximity forces, especially the closely related Casimir effect (1948),[88] could have inspired similar research on thermal radiation. More importantly, the general framework of fluctuational electrodynamics capable of consistently describing both Casimir effect and thermal radiation was proposed by Rytov[17, 18] in 1953, combining Maxwell's equations with the fluctuation-dissipation theorem governing electromagnetic fields. In fact, Rytov even solved an example problem of radiative heat transfer between two closely-spaced parallel plane surfaces, with one being an arbitrary dissipative medium and the other being a mirror of good electrical conductivity. He suggested that the "energy flow density into the mirror" could increase "without limit" as the spatial separation between the two planes vanishes, due to contribution from the "quasi-stationary field, localized in the layer close to the radiating surface".[17] This result represents a dramatic deviation from the constant heat flow independent of the separation as predicted by Planck's (Stefan-Boltzmann) law. However, no sequel to this remarkable episode was to be found until the beginning of the 1960s, when the practical need for managing radiative thermal transport across distances comparable to or smaller than the characteristic wavelength appeared.

In 1961, at the AFOSR/ADL Conference on Aerodynamically Heated Structures, A. G. Emslie[19] presented his analysis of radiative heat transfer in the multifoil radiation shields for thermal protection of cryogenic fuels in space. He estimated that at a temperature of 20 K the

peak of the Planck radiation distribution corresponds to a wavelength of $\lambda_{BB,\max}$ = 0.15 mm, which is of the same order of magnitude as the separation of the foils. The radiation transfer rate between metal foils with constant complex refraction index was predicted to increase with decreasing separation and attains a maximum of over 10 times the large-distance value at a separation of $0.2\lambda_{BB,\max}$ due to constructive interference of propagating waves. For even smaller gaps, however, the heat transfer rate was predicted to reduce to smaller values. Being aware of the evanescent waves, Emslie also noted that "radiation tunneling" could contribute to heat transfer across small gaps, causing further deterioration of the insulation performance of the shields. However, he did not quantitatively estimate the effect of such contribution as he felt that "an exact quantitative analysis of the magnitude of the energy transfer between two metals by the tunneling process is quite difficult to carry out."

A few years later investigations on radiative thermal transport across small gaps started gaining real momentum, with significant progress made in both theory and experiment. In 1967, Cravalho, Tien and Caren,[89] citing Emslie,[19] considered wave interference and radiation tunneling between two plane dielectrics of constant real refractive index at cryogenic temperatures. They were able to treat both effects in a unified approach and predicted an increase in heat flow with decreasing gap size as high as an order of magnitude. However, the assumption of lossless and non-dispersive dielectrics renders the work marginally relevant. It should be noted that a similar paper was published by Olivei in 1968, in which the concept of critical angle played a key role.[90] Later in 1970, Boehm and Tien[91] discussed the case of two metals separated by a transparent dielectrics with constant real refractive index, showing that the radiative heat transfer across small gaps is enhanced by many orders of magnitude, at cryogenic temperatures as well as room temperature. In order to account for nonlocal effects in metals, their use of the

anomalous skin effect theory for prediction of the optical properties is noteworthy. Despite yielding many qualitatively sound conclusions, their approach was considered unsatisfactory.

It was not until January 1971 when Polder and Van Hove presented their widely recognized theory of radiative heat transfer between closely spaced bodies.[92] The approach was based on Rytov's fluctuational electrodynamics, but instead of using fluctuating electromagnetic fields in Maxwell's equations as the source terms, they considered the thermally driven fluctuating currents. As a result, the solution was simplified.[92] They focused specifically on the case of two parallel semi-infinite bodies separated by a vacuum gap, where the two bodies are identical with isotropic, nonmagnetic but otherwise arbitrarily dispersive and absorptive properties (Fig. 1.1b). Specifically, radiative heat transfer between two chromium (Cr) half spaces was studied. Contributions to heat transfer across the vacuum gap from both the propagating and evanescent electromagnetic waves, as well as both the transverse electric (TE, or *s*-mode) and transverse magnetic (TM, or *p*-mode) polarizations were consistently considered, with each individual combination (say propagating TE or TM modes) naturally separated from the others (Fig. 1.1d-f). A comparison of the spectrum of radiated power in a small vacuum gap with that in an infinitely large gap clearly demonstrated the effect of constructive and destructive wave interferences (Fig. 1.1d). More importantly, contribution from evanescent TM modes was shown to be dominant for small gaps (Fig. 1.1e). In contrast to the constant heat transfer rate given by Planck's law, several orders of magnitude enhancement in heat transfer between two Cr surfaces across nanometer gaps was predicted at room temperature (Fig. 1.1f). Besides, the temperature dependence of various modes contributing to heat flow was analyzed. Note that the general expressions obtained from this work were semi-analytical, in the sense that they are not in a closed-form and involved integrals that require numerical integration.

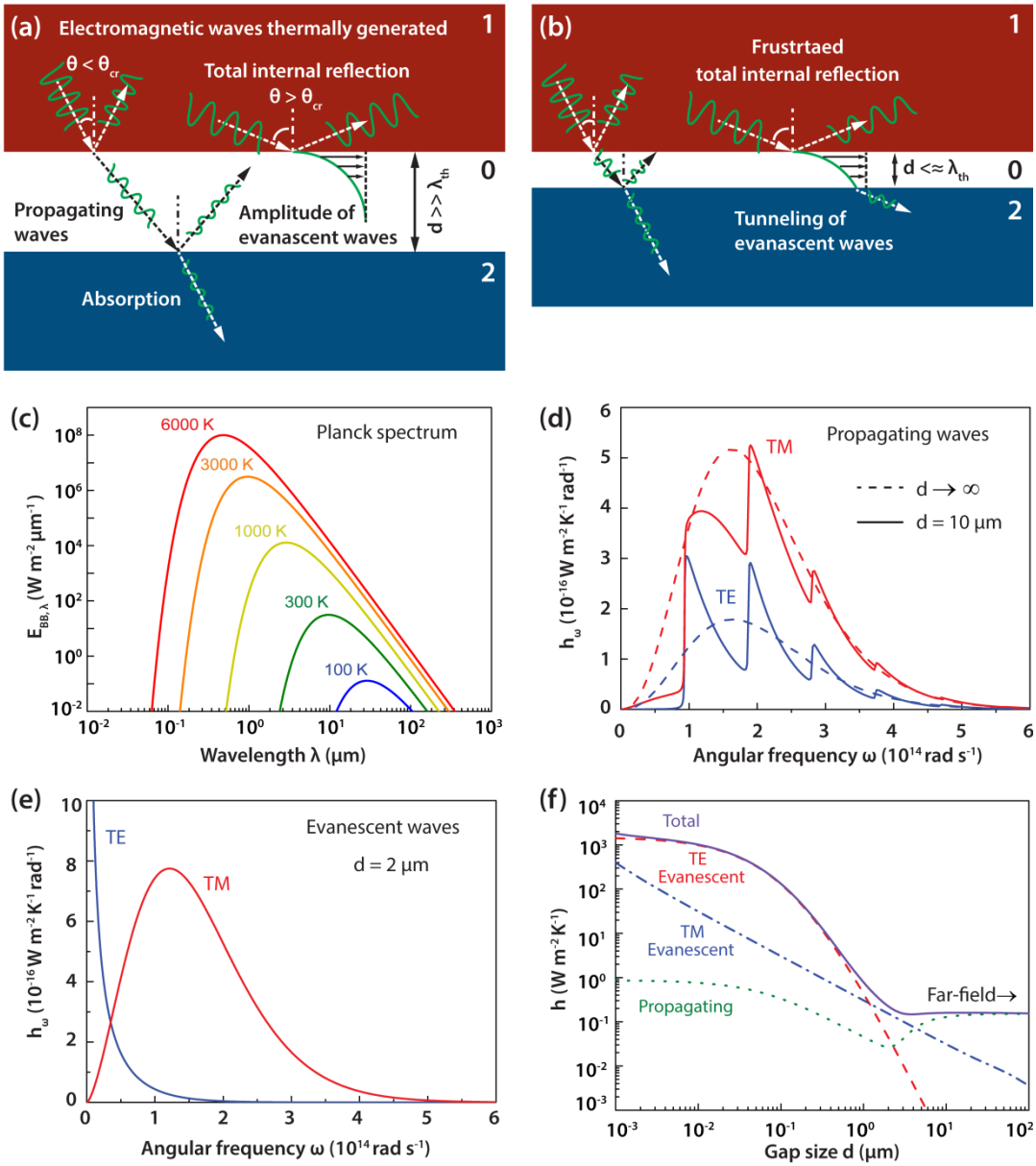

Figure 1.1: Fundamentals of Thermal Radiation and Radiative Heat Transfer in the Far- and Near-Field. (a) Schematic for far-field radiation between two parallel semi-infinite bodies denoted as "1" and "2", separated by a large vacuum gap denoted by "0". (b) Radiative heat transfer across a vacuum gap comparable to or smaller than the peak thermal wavelength. (c) Blackbody spectral emissive power given by Planck's law. (d) Spectral heat transfer coefficient due to propagating waves calculated for two Cr semi-bodies. (e) Spectral heat transfer coefficient due to evanescent waves. (f) Heat transfer coefficients showing contributions by different modes and polarizations. (d)-(f) are our calculation results using the same Cr dielectric function and other relevant parameters as found in Polder and van Hove.[92]

A few more theoretical papers were published in the following years.[16, 93-97] Similar to previous studies these works also focused on the one-dimensional (1D) configuration of two

parallel planes separated by a gap (mostly vacuum) due to both the computational ease as well as scope for a clear demonstration of the underlying physics. Of particular interest is a paper published in 1980 by Levin, Polevoi and Rytov[96] in which, expressions for the heat flux were given in terms of generalized surface impedance tensors, in principle covering anisotropic media with spatial dispersions. Again, a dramatic increase in heat transfer was predicted for small gaps. Please see Hargreaves[94] and Levin *et al.*[92] for detailed comments on these early studies.

Accompanying the early theoretical endeavors around the 1970s were a few carefully designed experiments.[98-103] Utilizing the parallel-plane configuration, all of which demonstrated a definitive dependence of radiative heat transfer on the spatial separations between emitting and receiving bodies from cryogenic to room temperatures, observing mostly few-fold enhancement of heat transfer at small gaps within the micrometer range. A detailed discussion is given in section 1.7.

1.4 Calculating Near-Field Radiative Heat Transfer between Parallel Planes

Central to most modern studies of thermal radiation is the intuitive picture of thermally driven fluctuating electromagnetic currents and fields. According to the fluctuation-dissipation theorem (FDT) of Callen and Welton,[13] the correlation between random temperature-driven electrical currents is directly related to the dielectric properties of a medium. When the macroscopic Maxwell's equations are solved with the random currents as sources (modeled using the FDT), the thermally excited energy flux (energy flow per unit time per unit area) is obtained from the ensemble-averaged Poynting vector. This basic framework for computing NFRHT is called the fluctuational electrodynamics (FE) formalism.[17, 18] Since heat transfer occurs between bodies at different temperatures, a key assumption of FE is that the current fluctuations are solely characterized by the FDT at the corresponding local thermodynamic

temperature, and are independent of the incident radiation from the other objects. Several widely available books and reviews[21-29, 104-108] describe the theoretical approaches and numerical methods based on FE that are used to study NFRHT, therefore here we provide only a concise summary. However, before we begin, it should be noted that theoretical considerations other than the FE formalism have also been proposed.[109-111]

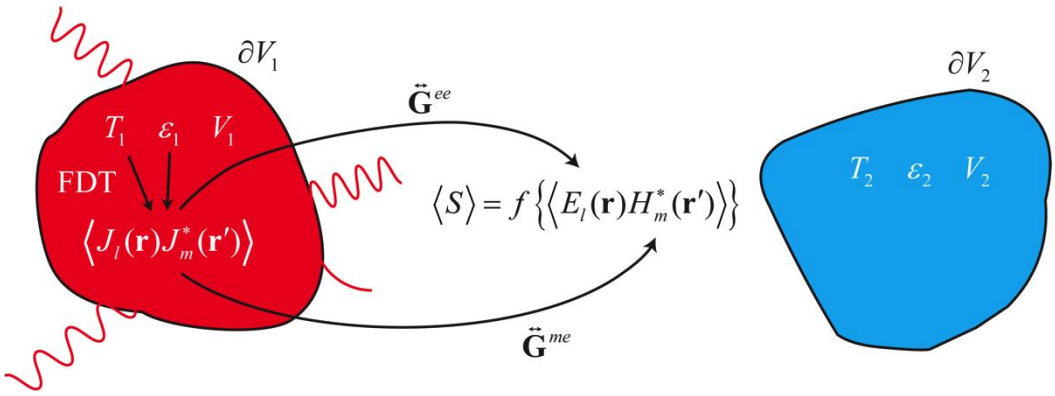

Figure 1.2: Schematic of Radiative Heat Transfer in a Two-Body System in Vacuum.
The bodies have uniform temperatures T_1 and T_2 throughout their volumes V_1 and V_2. The material properties are described by the frequency dependent complex dielectric functions ε_1 and ε_2. Electromagnetic fields **E** and **H** are generated by the random currents **J** in the bodies due to their non-vanishing correlations given by the FDT. The field correlations are related to the current correlations via the corresponding Green's dyads, and a linear combination of them yields the Poynting vector, which gives the heat current of interest.

Consider a system comprising of only two separated bodies, as illustrated in Fig. 1.2. Assuming a time convention of $e^{-i\omega t}$, the frequency domain macroscopic Maxwell's equations[112, 113] with random currents as the source[92] of thermal radiation can be written as

$$\nabla \times \mathbf{E}(\mathbf{r},\omega) = i\omega \mathbf{B}(\mathbf{r},\omega), \tag{1.3}$$

$$\nabla \times \mathbf{H}(\mathbf{r},\omega) = -i\omega \mathbf{D}(\mathbf{r},\omega) + \mathbf{J}(\mathbf{r},\omega). \tag{1.4}$$

Here, **E** and **B** are the complex electric and magnetic field vectors, **r** is the position vector and ω is the angular frequency, **D** and **H** are the electric displacement and magnetic induction, respectively, and are related to **E** and **B** via constitutive relations. For example, in isotropic media $\mathbf{D} = \varepsilon_0 \varepsilon \mathbf{E}$ and $\mathbf{B} = \mu_0 \mu \mathbf{H}$, where ε_0 and μ_0 are the vacuum permittivity and permeability,

$\varepsilon(\omega) = \varepsilon'(\omega)+i\varepsilon''(\omega)$ is the frequency-dependent complex dielectric function (relative permittivity) and $\mu(\omega) = \mu'(\omega)+i\mu''(\omega)$ is the relative permeability. All the fields above and below are functions of ω unless otherwise stated. Note that we do not explicitly incorporate any random magnetic current term in the curl equation for the electric field. For more general expressions please see Refs. [107, 114, 115]. We also assume non-magnetic materials with $\mu = 1$. Equation (1.3) and (1.4) leads to the following vector Helmholtz equations governing the electromagnetic waves:

$$\nabla\times\nabla\times\mathbf{E}(\mathbf{r},\omega)-\varepsilon(\omega)\left(\frac{\omega}{c}\right)^2\mathbf{E}(\mathbf{r},\omega)=i\omega\mu_0\mathbf{J}(\mathbf{r},\omega), \tag{1.5}$$

$$\nabla\times\nabla\times\mathbf{H}(\mathbf{r},\omega)-\varepsilon(\omega)\left(\frac{\omega}{c}\right)^2\mathbf{H}(\mathbf{r},\omega)=\nabla\times\mathbf{J}(\mathbf{r},\omega). \tag{1.6}$$

In practice only one of the two equations needs to be solved given the relation $\nabla\times\mathbf{E}(\mathbf{r},\omega)=i\omega\mu_0\mathbf{H}(\mathbf{r},\omega)$.

The free electric currents **J** are associated with fluctuating charges in the medium of interest and satisfy the statistical correlation function below given by the fluctuation-dissipation theorem:[13]

$$\left\langle J_l(\mathbf{r},\omega)J_m^*(\mathbf{r}',\omega)\right\rangle=\frac{4}{\pi}\varepsilon_0\varepsilon''(\omega)\omega\Theta_0(\omega,T)\delta_{lm}\delta(\mathbf{r}-\mathbf{r}'), \tag{1.7}$$

where $\Theta_0(\omega,T)=\hbar\omega\left(\frac{1}{2}+\frac{1}{e^{\hbar\omega/k_BT}-1}\right)$ is the mean energy of a harmonic oscillator including the zero point contribution; $\hbar = h_P/2\pi$ is the reduced Planck constant; T is the absolute temperature and the superscript * denotes the complex conjugate. The Kronecker delta $\delta_{l,m}$ indicates no cross coupling between currents in orthogonal directions represented by the subscripts l and m, while the Dirac delta $\delta(\mathbf{r} - \mathbf{r}')$ reflects the assumption of locality, excluding spatial dispersions in the

media. Note that a factor of 4 is included in Eqn. 1.7 so only positive frequencies are considered subsequently.[24, 26, 27, 108] Other variations of Eqn. 1.7 with differences only in the constant have also been used in the literature.[22, 23, 107]

When combined with the proper boundary conditions of a given problem, Eqs. (1.3)-(1.7) allow for calculation of the spectral radiative heat flux as the ensemble-averaged Poynting vector $\langle \mathbf{S}(\mathbf{r},\omega)\rangle = \mathrm{Re}\langle \mathbf{E}\times\mathbf{H}^{*}\rangle/2$. It can be expressed in terms of the known $\langle J_l(\mathbf{r},\omega)J_m^{*}(\mathbf{r}',\omega)\rangle$ by using the dyadic Green functions[116] $\ddot{\mathbf{G}}^{ee}(\mathbf{r},\mathbf{r}',\omega)$ and $\ddot{\mathbf{G}}^{he}(\mathbf{r},\mathbf{r}',\omega)$ via the relations[22]

$$\mathbf{E}(\mathbf{r},\omega) = i\omega\mu_0\int_V d\mathbf{r}'\ddot{\mathbf{G}}^{ee}(\mathbf{r},\mathbf{r}',\omega)\cdot\mathbf{J}(\mathbf{r}',\omega), \tag{1.8}$$

$$\mathbf{H}(\mathbf{r},\omega) = \int_V d\mathbf{r}'\ddot{\mathbf{G}}^{me}(\mathbf{r},\mathbf{r}',\omega)\cdot\mathbf{J}(\mathbf{r}',\omega). \tag{1.9}$$

Key to this approach is then finding analytically the dyadic Green functions which satisfy the wave equations below with Dirac delta sources for a given configuration:

$$\nabla\times\nabla\times\ddot{\mathbf{G}}^{ee}(\mathbf{r},\mathbf{r}',\omega) - \varepsilon(\omega)\left(\frac{\omega}{c}\right)^2\ddot{\mathbf{G}}^{ee}(\mathbf{r},\mathbf{r}',\omega) = \ddot{\mathbf{I}}\delta(\mathbf{r}-\mathbf{r}'), \tag{1.10}$$

$$\nabla\times\nabla\times\ddot{\mathbf{G}}^{me}(\mathbf{r},\mathbf{r}',\omega) - \varepsilon(\omega)\left(\frac{\omega}{c}\right)^2\ddot{\mathbf{G}}^{me}(\mathbf{r},\mathbf{r}',\omega) = \nabla\times\left[\ddot{\mathbf{I}}\delta(\mathbf{r}-\mathbf{r}')\right], \tag{1.11}$$

where $\ddot{\mathbf{I}}$ is the identity dyad. Similar to Eqn. 1.5 and 1.6, only one of the two equations needs to be solved. Note that the Green dyads for many simple geometries have been obtained in the electromagnetism community and can be readily used.[116, 117] The expression of the field correlations in terms of the current correlations and the Green dyads[22] is

$$\left\langle E_i(\mathbf{r},\omega)H_j^{*}(\mathbf{r}',\omega)\right\rangle = i\omega\mu_0\left\langle\int_V d\mathbf{r}'G_{il}^{ee}(\mathbf{r},\mathbf{r}',\omega)G_{jm}^{me*}(\mathbf{r},\mathbf{r}'',\omega)\int_V d\mathbf{r}''J_l(\mathbf{r}',\omega)J_m^{*}(\mathbf{r}'',\omega)\right\rangle, \tag{1.12}$$

where the subscripts *i* and *j* denote spatial directions. Using Eqn. 1.7 and the Delta functions therein, Eqn. 1.12 can be further written as[22]

$$\left\langle E_i(\mathbf{r},\omega)H_j^*(\mathbf{r}',\omega)\right\rangle = i\frac{4\varepsilon''(\omega)\omega^2}{\pi c^2}\Theta_0(\omega,T)\int_V d\mathbf{r}' G_{il}^{ee}(\mathbf{r},\mathbf{r}',\omega)G_{jl}^{me*}(\mathbf{r},\mathbf{r}',\omega), \tag{1.13}$$

where the equality $\varepsilon_0\mu_0 c^2 = 1$ has been used. Since the spectral heat flux $\langle\mathbf{S}(\mathbf{r},\omega)\rangle$ is a linear combination of these field correlations, the radiative heat flux can be readily obtained. An integral of $\langle\mathbf{S}(\mathbf{r},\omega)\rangle$ with respect to the angular frequency yields the total heat flux $\langle\mathbf{S}(\mathbf{r})\rangle$; and integration of the normal component of $\langle\mathbf{S}(\mathbf{r})\rangle$ over the entire surface of the object of interest gives the net heat current (energy flow per unit time).

Based on the concepts and the general procedure outlined above, thermal emission of isolated bodies as well as radiative thermal transport between different objects can be described. As an example, the solution of radiative heat transfer between two parallel semi-infinite bodies separated by a vacuum gap (Fig. 1.1a, b) can be obtained by making use of the well-known Green function for this geometry.[22, 117] Due to its simplicity, the parallel-plane configuration became one of the first NFRHT problems to be analytically solved. The study of such parallel configurations has since allowed numerous physical insights to be obtained. Written in a Landauer-type expression, the total heat flux across a vacuum gap d is given by

$$q(T_1,T_2,d) = \int_0^\infty \frac{d\omega}{4\pi^2}\left[\Theta(\omega,T_1)-\Theta(\omega,T_2)\right]\int_0^\infty dkk\left[\tau_s(\omega,k)+\tau_p(\omega,k)\right], \tag{1.14}$$

where $\Theta(\omega,T) \equiv \hbar\omega/[\exp(\hbar\omega/k_BT)-1]$ is the mean energy of a harmonic oscillator less the zero point contribution; T_i are the absolute temperatures, with subscripts 1 and 2 denoting the emitter and receiver, respectively; the vacuum gap is denoted with subscript 0; *k* is the wave vector component parallel to the planar surfaces, and τ_s and τ_p are the transmission probabilities for the

TE and TM modes, respectively. These probabilities can be expressed in terms of the Fresnel coefficients of the interfaces as follows,[118]

$$\tau^{12}_{\alpha=s,p}(\omega,k)=\begin{cases}\dfrac{(1-\left|r_\alpha^{01}\right|^2)(1-\left|r_\alpha^{02}\right|^2)}{\left|D_\alpha\right|^2}, & \text{if } k<\omega/c, \text{ propagating waves}\\ \dfrac{4\,\mathrm{Im}\left(r_\alpha^{01}\right)\mathrm{Im}\left(r_\alpha^{02}\right)e^{-2\,\mathrm{Im}(\zeta_0)d}}{\left|D_\alpha\right|^2}, & \text{if } k>\omega/c, \text{ evanascent waves}\end{cases} \tag{1.15}$$

In Eqn. 1.15, r_α^{ij} are the Fresnel reflection coefficients at the interfaces between vacuum and the two half spaces, and are given by $r_s^{ij}=\left(\zeta_i-\zeta_j\right)/\left(\zeta_i+\zeta_j\right)$ and $r_p^{ij}=\left(\varepsilon_j\zeta_i-\varepsilon_i\zeta_j\right)/\left(\varepsilon_j\zeta_i+\varepsilon_i\zeta_j\right)$, where $\zeta_i=\sqrt{\varepsilon_i(\omega)\omega^2/c^2-k^2}$ is the transverse component (perpendicular to the planes) of the wave vector in layer *i* and $\varepsilon_i(\omega)$ is the corresponding frequency-dependent complex dielectric function. $D_\alpha=1-r_\alpha^{01}r_\alpha^{02}e^{2i\zeta_2 d}$ is the Fabry-Pérot-like denominator.

As useful as Eqs. (1.14) and (1.15) are, they have been derived only to calculate radiative heat flux between half spaces (or thick objects in practice) and are not adequate to describe systems featuring thin films and layers which are of significant technical importance. When the emitter and/or receiver are not semi-infinite, but instead are multilayer systems (including thin films) with internal interfaces and finite thicknesses, a direct calculation of the radiative heat flux proves difficult as many emission sources (the layers) and/or multiple reflections at interfaces have to be properly accounted for. Alternatively, one can focus instead only on the field inside the vacuum gap and obtain formally the same expression as given in Eqn. 1.14, only that Eqn. 1.15 is now replaced with the one below:[107, 119]

$$\tau^{12}_{\alpha=s,p}(\omega,k)=\begin{cases}\dfrac{(1-\left|R^1_\alpha\right|^2)(1-\left|R^2_\alpha\right|^2)}{\left|D_\alpha\right|^2}, & \text{if } k<\omega/c, \text{ propagating waves}\\ \dfrac{4\,\mathrm{Im}\left(R^1_\alpha\right)\mathrm{Im}\left(R^2_\alpha\right)e^{-2\,\mathrm{Im}(\zeta_0)d}}{\left|D_\alpha\right|^2}, & \text{if } k>\omega/c, \text{ evanascent waves}\end{cases} \tag{1.16}$$

where the Fresnel coefficients r^{ij}_α are replaced by R^i_α, which are the total reflection coefficients of the multilayer systems as seen from inside the vacuum gap, and can be calculated using textbook[113] procedures from all the interface Fresnel coefficients. In the case of half spaces $R_\alpha{}^{\mathrm{i}}$ reduce to the vacuum interface Fresnel coefficients, thus reproducing Eqn. 1.15.

In order to present results in a form that enables direct comparisons with experiments performed under a small temperature differential, the linear thermal conductance (heat current per unit temperature difference) or heat transfer coefficient (thermal conductance per unit area, h) at a mean temperature T can be obtained from:

$$h(T,d)\equiv\lim_{(T_1-T_2)\to 0}\left|\frac{q(T_1,T_2,d)}{T_1-T_2}\right|=\int_0^\infty\frac{d\omega}{4\pi^2}\frac{\partial\Theta(\omega,T)}{\partial T}\int_0^\infty dk k\left[\tau_s(\omega,k)+\tau_p(\omega,k)\right]\equiv\int_0^\infty d\omega h_\omega(T,d), \tag{1.17}$$

where the spectral heat transfer coefficient h_ω is also introduced.

The planar configuration as solved above using the GF formalism has proven suitable for analyzing a wide variety of media.[47, 48, 92, 96, 97, 107, 114, 115, 118-171] Equations (1.14)-(1.17) can even be readily used for structured and composite materials with their dielectric responses modeled using the effective medium theories (EMT).[21] Apart from computing NFRHT between parallel planes, the GF formalism has also been used for a range of other basic configurations including dipole-plane, dipole-dipole, sphere-sphere, sphere-plane and cylinder-cylinder.[20, 129, 172-182]

1.5 Potential of Near-Field Thermal Radiation in Energy Conversion

A variety of near-field thermal radiation-based devices for energy conversion have been proposed by many researchers.[68-84] For example, Park *et al.*[71] have suggested that near-field radiation could be employed to enhance the power output of thermophotovoltaic (TPV) devices. Recent computational studies have also discussed the possibility of using graphene based near-field thermophotovoltaic (NFTPV) devices to achieve extremely large efficiencies. While advances[77] in TPV devices have demonstrated the feasibility of using nanostructured surfaces for improved thermophotovoltaic energy conversion, to date there has not been any experimental demonstration of a highly-efficient NFTPV device despite the many appealing computational proposals. Apart from thermophotovoltaic energy conversion, Yang *et al.*[81] have computationally explored the potential of a thermoelectric device where the hot side of the device is coupled to a hot thermal reservoir across a vacuum gap via near-field thermal radiation. The authors suggested that in such a device it is possible to establish a higher non-equilibrium temperature for the electrons than for the phonons thus effectively attenuating the deleterious contributions of phonons to thermoelectric performance. The effect of NFRHT on thermionic energy conversion devices was also discussed.[83, 84] In addition to the possibility of creating novel energy conversion devices, Pendry[20] has suggested that near-field radiation could potentially be employed for achieving high-resolution thermal lithography. Finally, it also seems that understanding NFRHT, especially in the 1-10 nm gap regime, may be important for optimizing the performance of heat-assisted magnetic recording (HAMR) technologies[42-44] where a plasmonic antenna (which localizes the electric fields) is used to heat a magnetic recording medium[43] so as to lower the magnetic coercivities in localized regions. In these devices, it is expected that NFRHT can play an important role in the steady-state temperature achieved in the magnetic medium and hence understanding NFRHT could help optimize the performance of HAMR technologies.

1.6 Near-Field Radiation for Creating Thermal Diodes

Rectification of heat flow refers to the situation where the magnitude of heat current depends on the direction of applied thermal bias.[183, 184] A device that rectifies heat flow is often referred to as a thermal diode in analogy to an electrical diode. The defining characteristic of a thermal diode is the degree of asymmetry in the forward (Q_f) and reverse (Q_r) heat currents when an identical temperature differential is applied in two different directions, where forward typically corresponds to the direction that results in a larger Q_f than Q_r. Slightly different definitions of the rectification capacity have been used by different research groups in the past. Here, we use the definition of thermal rectification coefficient, $\eta = (Q_\mathrm{f} - Q_\mathrm{r})/Q_\mathrm{f}$. Because $\eta \leq 1$ always, we express it as a percentage. Although thermal diodes based on heat conduction and convection have long been proposed and studied, radiative thermal diodes were only proposed in recent years, exploring both near-field[54-56, 58-60, 62] and far-field thermal radiation.[57, 61, 63]

The first proposal and many subsequent ones are based on the temperature dependence of material dielectric functions, which causes spectral mismatch between the peak wavelengths of the emitter and the receiver.[54, 55, 59] Specifically, Otey *et al.*[54] calculated rectification between 3C-SiC and 6H-SiC half spaces, considering the temperature dependence of the surface phonon polaritons supported by SiC. A maximum rectification coefficient of η = 29% was obtained for gaps from ~10 nm to ~200 nm, with the high and low temperatures being T_h = 600 K and T_l = 300 K, respectively.[54] Recent computational studies of NFRHT between a lightly (10^{18} cm^{-3}) doped Si film and a heavily (10^{21} cm^{-3}) doped Si half space have demonstrated that for small gaps (1 nm to 50 nm), rectification ratios greater than 33% can be achieved.[55] In that study, the thin film was chosen to take advantage of hybridization of surface plasmon polaritons on the front and back surfaces. In another study by Wang and Zhang,[59] NFRHT between intrinsic Si

and doped Si and between intrinsic Si and SiO_2 (T_h = 1000 K and T_l = 300 K) was studied and rectification coefficients of 90% and 73%, respectively, were reported when the gap size was 5 nm. In the same work NFRHT was studied between intrinsic Si and Au and a smaller rectification coefficient of 44% was obtained, albeit for a much larger gap size range (10 nm – 500 nm) with T_h = 600 K and T_l = 300 K.

Apart from near-field thermal diodes, far-field rectification schemes have also been proposed.[57, 61, 63] One such scheme is based on two 1D periodic layered structures each featuring one Fabry-Perot cavity which function as selective emitters with sharp emission peaks.[63] The temperature dependence of the dielectric properties of the Au mirror layers and the highly-doped Si mirror layers is key to the obtained thermal rectification. Specifically, for a T_h = 670 K and T_l = 300 K, a rectification of ~19% was reported. One benefit of this design is in its potential for optimization depending on the temperature of the emitter and receiver as the spectral characteristics of the selective emitters can be tuned via suitable choice of the materials and dimensions of parameters of the composing layers. Further, rectification based on metal-insulator transition materials was also investigated.[57, 58] In one case,[57] VO_2 and SiO_2 were used. For far-field radiation, a rectification greater than 41% was obtained with emitter and receiver temperatures near the critical temperature T_C of VO_2. In another case, NFRHT between VO_2 and a second MIT material, $La_{0.7}Ca_{0.15}Sr_{0.15}MnO_3$ (LCSMO, T_C = ~301 K), was exploited and a rectification ratio of 89% was obtained at a gap of 10 nm, with T_h = 80 K and T_l = 26 K.[58]

Finally, ultrahigh-contrast and large-bandwidth thermal rectification between a large and a small nanosphere was suggested, exploiting the scale invariance properties of the resonance modes of the spheres, which result in a large difference in the coupling constants between

relevant modes in the forward and reverse scenarios.[60] Rectification ratios greater than 90% were reported for two 3C-SiC nanospheres.

1.7 Past Experiments between Parallel Plates

The first measurements of near-field radiative heat transfer between parallel plates were reported by Cravalho, Domoto and Tien in an AIAA conference[98] and in a subsequent paper.[100] Their apparatus consisted of two parallel copper disks with a diameter of 85 mm that were located in an ultra-high vacuum chamber (10^{-12} torr), which was cooled to ~4.2 K by complete immersion in a bath of liquid helium (Fig. 1.3a). The top disk serves as a radiative emitter with its temperature raised by a few kelvin via Joule heating by attached carbon resistors. The radiative heat currents received by the bottom disk (receiver) were estimated by measuring the increase of the receiver's temperature. The spatial separation between the disks was changed from as large as 2 mm to as small as 10 μm by displacing the emitter disk using an external micrometer adjuster. Mechanical contact between the disks was detected by monitoring the electrical conductance between the disks. However, a controlled approach for tuning the parallelism or quantitatively estimating it seems to be lacking. Their experimental data (Fig. 1.3b) showed "definite gap-size dependence of radiative transfer" with as large as a factor of five increase in radiative heat flow at small gaps (~10 μm). The overall enhancement in the measured heat flow was an order of magnitude larger than what they computationally predicted by accounting for wave interference and tunneling.[89] They attributed this discrepancy to the deviation from parallelism and to uncertainties in both the surface conditions of the copper disks in the experiments and in the optical properties used in their calculations.

A similar experiment with copper disks (107 mm diameter) was also carried out later by Kutateladze, Rubtsov and Baltsevich[102] where the spatial separation between the disks was

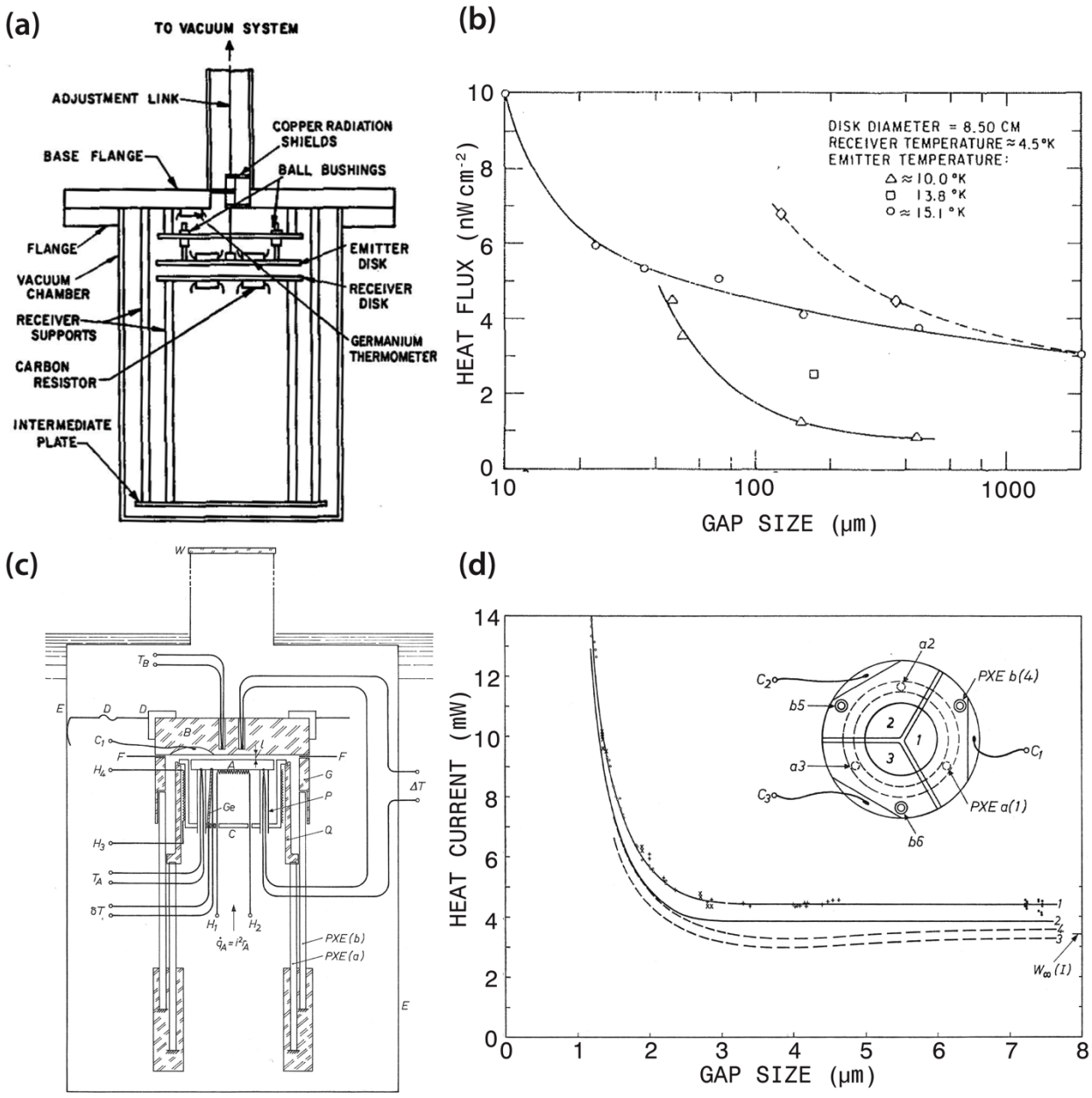

Figure 1.3: Early Experimental Investigations of NFRHT between Parallel Planes.
(a) Schematic of the plate-plate setup used by Cravalho *et al.*[98] (b) Results[100] for radiative heat flux versus the spacing between copper disks using the setup in (a) for temperature differences ΔT of 10.0 K, 13.8 K and 15.1 K. (c) Schematic of the plate-plate setup used by Hargreaves.[101] (d) Results[101] for heat current versus gap size between Cr-coated surfaces near room temperature. Curves (solid lines) have been fit to the experimental data before (1) and after (2) accounting for heat losses. Theoretical curves calculated using Drude model values from the literature[92] (3) and empirically fitted values (4) are also shown. Inset: Schematic top view of the pyrex disk with its three sectors of evaporated Cr. The entire surface serves as the receiver, while the three sectors form three independent capacitors with the Cr coating on the emitter. Panels (c) and (d) were adapted from the Ph.D. thesis of Hargreaves.[101]

varied from ~250 μm to ~10 μm and a range of temperature differentials and absolute temperatures were investigated at about 2×10^{-7} torr. These measurements confirmed the strong

distance dependence of NFRHT in all cases, demonstrating a five-fold enhancement at small gaps, although no comparison with theory was provided. Their results also showed that the threshold gap size beyond which heat transfer enhancements are observed is ~$3\lambda_{BB,\max}$, where the peak wavelength was estimated from Wien's displacement law and the known temperature of the emitter.

The first plate-plate NFRHT studies at room temperature were reported by Hargreaves in 1969.[99] The experimental setup as reported in his thesis[101] features a chamber, which is pumped to about 10^{-5} torr (Fig. 1.3c), and can be immersed in liquid baths of different temperatures. In that setup, the macroscopic emitter and receiver plates (25 mm diameter) were each supported by three independent piezoelectric ceramic tubes, enabling precise tuning of the gap size as well as the parallelism between the plates. The parallelism of the plates was evaluated using both optical interferometry and by measuring the electrical capacitance of three individual capacitors created by three pairs of metallic plates integrated into the emitter and receiver disks (Fig. 1.3d inset). Specifically, the differences in the three capacitances indicated the level of parallelism, whereas the sum signal served as a measure of the absolute gap size. Mechanical contact between the plates could also be detected by monitoring the electrical conductance between the plates. Chromium was selected as the surface coating (100 nm thick) for both plates as it features a relatively low reflectivity and high hardness, with the former property contributing to higher heat currents and the latter providing robustness against surface damage during the parallelization of the plates, for which inadvertent contacts occur. Individual plate temperatures were measured with embedded thermistors, while their difference was measured using copper-constantan thermocouples. With the emitter heated resistively, the radiative heat flow to the receiver was

estimated as the additional heat input required to maintain the temperature of the emitter at a constant value as the gap size was varied from ~8 μm - 1 μm.

Preliminary results reported[99] by Hargreaves in 1969 clearly showed a strong distance dependence of radiative heat transfer at room temperature (emitter temperature 323 K and receiver temperature 306 K), with a noticeable increase starting at a gap size of ~2.5 μm (the figure in the original paper mislabeled the range in the x-axis[101]). However, computational results permitting a comparison were only obtained later in 1971 by Polder and van Hove.[92] And despite the broad agreement, the measured heat currents at bigger gaps were a factor of three larger than the predicted value. This discrepancy was attributed to errors in the optical properties of Cr used in the computational analysis, and challenges in making accurate thermal measurements.[101] Hargreaves reported refined measurements (emitter at 313 K and receiver at 295 K) later in his thesis,[101] which showed much better agreement with theory as well as a large enhancement in heat transfer (~4 fold) at the smallest gaps (Fig. 1.3d). In addition to the room temperature measurements, studies were also performed at low temperatures, for example with the emitter at 160 K and the receiver at 132 K, and larger enhancements were observed. Temperature dependence of the threshold gap size, as well as that of radiative heat transfer at various gap sizes was also discussed. A quantitative comparison of these improved measurements[101] with Polder and van Hove's theory showed that the predicted results were consistently smaller than the measured ones (Fig. 1.3d); nevertheless, the overall agreement was improved. The discrepancy was again largely attributed to the optical properties of the Cr layers.

Following these pioneering measurements no new experimental results on heat flow between closely-spaced parallel planes were published until the early 2000s when the growing field of micro- and nanotechnology necessitated that heat transfer between closely-spaced bodies

be better understood. In 2008, Hu *et al.*[185] revisited the topic by measuring NFRHT between parallel glass optical flats (127 mm diameter) which support SPhPs in the mid-infrared as discussed in previous sections. They observed much larger enhancements in radiative heat flow than had been measured between metal surfaces in the past. Hu's experimental platform consisted of a hot glass emitter separated from a room temperature glass receiver located underneath by means of dispersed polystyrene microspheres as spacers. The emitter temperature was elevated to tens of Kelvin above room temperature and controlled to within 1 K using a heating pad attached atop it, while a 1×1 in^2 heat flux meter was placed beneath the receiver so that the radiative heat current could be measured. The vacuum gap (~6×10^{-5} torr) paired with the low thermal conductivity of the polystyrene spacers was expected to ensure that radiative heat transport dominated the total heat flux. Using spheres with a nominal diameter of 1 μm, Hu *et al.* were able to measure heat flow consistent with theoretical predictions for glass plates separated by a 1.6 μm gap. They observed that the heat flow across the micrometer gap is about twice as large as the far-field data recorded at 2 mm separation, and is about 50% larger than the blackbody limit. However, measurement with systematically varied gap size was not possible with this platform.

Subsequently, two different studies[186, 187] sought to investigate NFRHT for varying gap size. The first study[186] reported NFRHT between two 50×50 mm^2 sapphire plates near room temperature as a function of vacuum (~2×10^{-7} torr) gap size and temperature difference. The experimental apparatus used in this study is illustrated schematically in Fig. 1.4a. In this experiment the gap size and parallelism were measured by monitoring the capacitance of four pairs of copper plates located in the corners of the sapphire plates. The orientation of the emitter as well as the spacing between the plates were controlled via three stepper motors. The

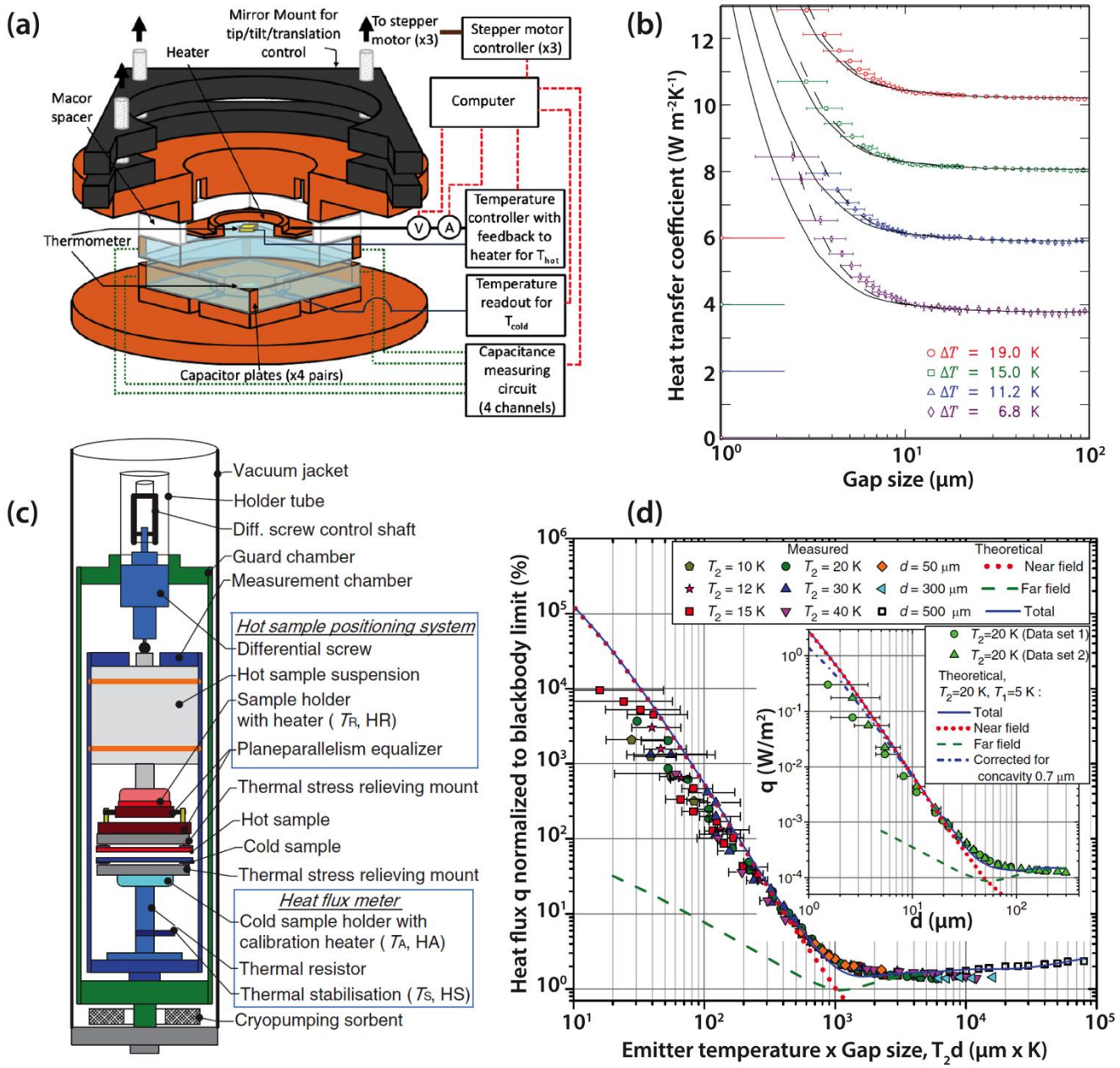

Figure 1.4: Recent Experimental Investigations of NFRHT between Parallel Planes.
(a) Schematic of the experimental apparatus used by Ottens *et al.*[186] to measure NFRHT between sapphire plates. (b) Results[186] for heat transfer coefficient versus vacuum gap size between the sapphire plates for four temperature differences. Each curve is offset by 2 Wm^{-2}K^{-1} from the last for clarity. Experimental data (points) is plotted alongside theory for planar (solid lines) and slightly curved (dashed lines) surfaces. (c) Schematic of the experimental setup used by Kralik *et al.*[188] (d) Their[187] measured heat flux normalized to the blackbody limit. Theoretical curves were calculated for receiver temperature T_1 = 5 K and emitter temperature T_2 = 20 K. Open squares represent far field data taken at higher temperatures with a nominally black surface. Inset: Heat flux versus gap size for the experimental conditions indicated in the legend.

temperature of the hot sapphire plate was controlled by a feedback loop, and the cold plate was attached to a thermal bath. The heat flow was estimated by monitoring the electric current and voltage across the heater and computing the power input required to maintain the desired temperature difference. Heat transfer data for temperature differences ranging from 6.8 K to 19 K were reported as a function of gap size (~2 μm - 100 μm), as shown in Fig. 1.4b. The threshold gap size beyond which appreciable heat transfer enhancements are observed was ~10 μm. And the total heat transfer coefficients monotonically increased with decreasing gap size, reaching a maximum relative enhancement of about two fold. A fairly good agreement was found between the measured and the theoretically predicted heat transfer coefficients. The measured values were found to be slightly higher than the predictions at smaller gaps while having good agreement at larger gaps. This was attributed to the slight curvature (convexity) of the macroscopic sapphire plates, which were measured using Newton rings to have a deviation from flatness of 170 ± 30 nm across the square sapphire plate. Once this curvature was considered in theoretical predictions (dashed lines in Fig. 1.4b), the agreement with experiments improved.

Another study[187,188] reported NFRHT between parallel W layers at cryogenic temperatures (receiver temperature at 5 K) as the vacuum (~10^{-10} torr) gap size varies from 1 μm to 500 μm for several temperature differences (ΔT = 5 K – 35 K). Their setup[188] is illustrated in Fig. 1.4c. In these experiments, a 35 mm-diameter W emitter was placed in close proximity to a W receiver via a differential screw (resolution 100 μm/rev). Parallelization between the emitter and receiver plate was achieved by bringing the two into contact with each other and then maintained after they were separated using a so-called parallelism equalizer which mechanically locks the orientation of the emitter plate by friction.[188] The receiver was mounted on a heat flux

meter, which consists of two temperature sensors separated by a calibrated thermal resistance, so that the heat flow could be estimated. The results from this work[187] are shown in Fig. 1.4d, where the measured heat flow is normalized to that expected from blackbodies and is plotted with respect to the product of the emitter temperature and gap size. A threshold gap size of ~50 μm was observed when the emitter temperature was 20 K. The data agreed well with the theoretical prediction except at the smallest gaps for which the measured values are noticeably lower than the theoretical lines. Similar to the sapphire-plate work discussed above, this discrepancy was attributed to the reported concavity of 700 nm across the W plates (see inset of Fig. 1.4d for corrected theoretical prediction). Remarkably, the measured heat flow at a gap size of 2 μm still exceeded that of a blackbody by two orders of magnitude despite the concavity. This factor of 100 represents the largest near-field enhancement observed to date in parallel-plane geometry. As to relative heat flow increase from large to small gaps, about three to four orders of magnitude enhancement was demonstrated.

In addition to experimental schemes featuring independent, macroscopic emitter and receiver plates, several recent studies[189-191] have reported MEMS-based approaches to studying NFRHT between suspended microstructures that are part of a monolithic device. In one group of studies,[189, 190] a small gap of fixed size (550 nm[189] and 1 μm[190]) was formed between two nominally parallel SiO_2 membranes (say 200 nm and 400 nm thick, size is ~80 × 80 μm^2)[190] via etching of a sacrificial Al layer in between. The thermal measurement was performed in high vacuum (~10^{-6} torr) by resistively (poly-Si[189] or Pt[190] resistor) heating and monitoring the temperature of the emitter SiO_2 surface, both in the presence of the receiver SiO_2 surface and when it is removed with a microprobe. For the same known electric heating current, the emitter reaches different steady-state temperatures with or without the receiver; and this temperature

difference is then used to evaluate the near-field thermal conductance between the two membranes. It was concluded[190] that for a gap size of 1 μm the near-field conductance was ~10 times larger than the blackbody limit when the emitter temperature was within 300 - 400 K. Although no comparison with any near-field calculation was given, the observed enhancement seems to be much higher than available theoretical predictions for bulk materials.[156] Another recent MEMS-enabled experiment[191] explored NFRHT between parallel nanobeams (1.1 μm wide, 500 nm thick, 200 μm long) coated with 100 nm-thick SiO_2. With one beam fixed and the other controlled using electrostatic actuation, they were able to cover nominal vacuum (1.5×10^{-4} torr) gap sizes between 250 nm and 750 nm with a single device. The observed near-field conductance exceeded the blackbody limit as the gap size became smaller than ~600 nm and reached a maximum of ~7 times the limit. This approach could have potential for detailed NFRHT studies if it can be adapted to study NFRHT between parallel planes instead of beams which have relatively small and poorly-defined surfaces. Note that the absolute size of the emitter and receiver could have a large impact on NFRHT considering the dominant role of surface modes and their long wavelength and propagation distance along the surfaces.[118]

As shown above, the experimental investigation of parallel-plane NFRHT boasts a long history of almost half a century and a range of ingenious instrumentation efforts and achievements. Nonetheless, many challenges remain in order to explore and exploit the rich physics in the thermal near-field. All the existing macroscopic approaches have been limited to micrometer gaps due to imperfect parallelism, surface curvature and inevitable particulate contaminations. Taking advantage of the ever maturing microfabrication technology, the MEMS-based studies represent an important experimental advancement especially since they allow the creation of nanoscale gaps and have no need for complex precision positioning and control

platform. Nevertheless, the smallest gap size observed still remains in the hundreds of nanometer range; and further improvements are required to evaluate the parallelism, the surface roughness and curvature, as well as to enable measurements between a wider variety of materials/structures and across controllable gap size. At last, we note that the sub- micrometer film thickness could potentially complicate the numerical modeling process especially for larger gaps.

1.8 Recent Experiments between Parallel Plates Conducted in our Lab

In our own experiments,[2] we reported 100 to 1000-fold enhancements in the radiative conductance between parallel-planar surfaces at gap sizes below 100 nm, in agreement with the predictions of near-field theories[192, 193]. Our measurements of near-field radiative heat transfer in vacuum gaps between prototypical materials (SiO_2-SiO_2, Au-Au, and SiO_2-Au) were performed using novel microdevices and a custom-built nanopositioning platform[194], which allows precise control over a broad range of gap sizes (<100 nm to 10 μm).

To enable direct, systematic measurements of radiative heat currents between two parallel-planar surfaces separated by a nanoscale vacuum gap we fabricated Si-based microdevices that feature thermally isolated flat regions with characteristic dimensions of ~48 μm and are coated with a desired dielectric (SiO_2) or metal (Au). Figures 1.5a and b show scanning electron microscope (SEM) images of the devices, which are called the receiver and the emitter, respectively. The emitter device (Fig. 1.5b) features a 20 μm tall, 48 μm × 48 μm Si mesa fabricated via a high-aspect-ratio etching process to serve as the emitter. The elevation of the mesa ensures that only its top surface (emitter active area, false colored in Fig. 1.5b) forms nanoscale gaps with the receiver, while the rest of the device remains in the far-field. Both devices feature integrated resistance heater-thermometers that enable us to heat the emitter and measure temperature changes in the receiver. Characterization via atomic force microscopy (Fig.

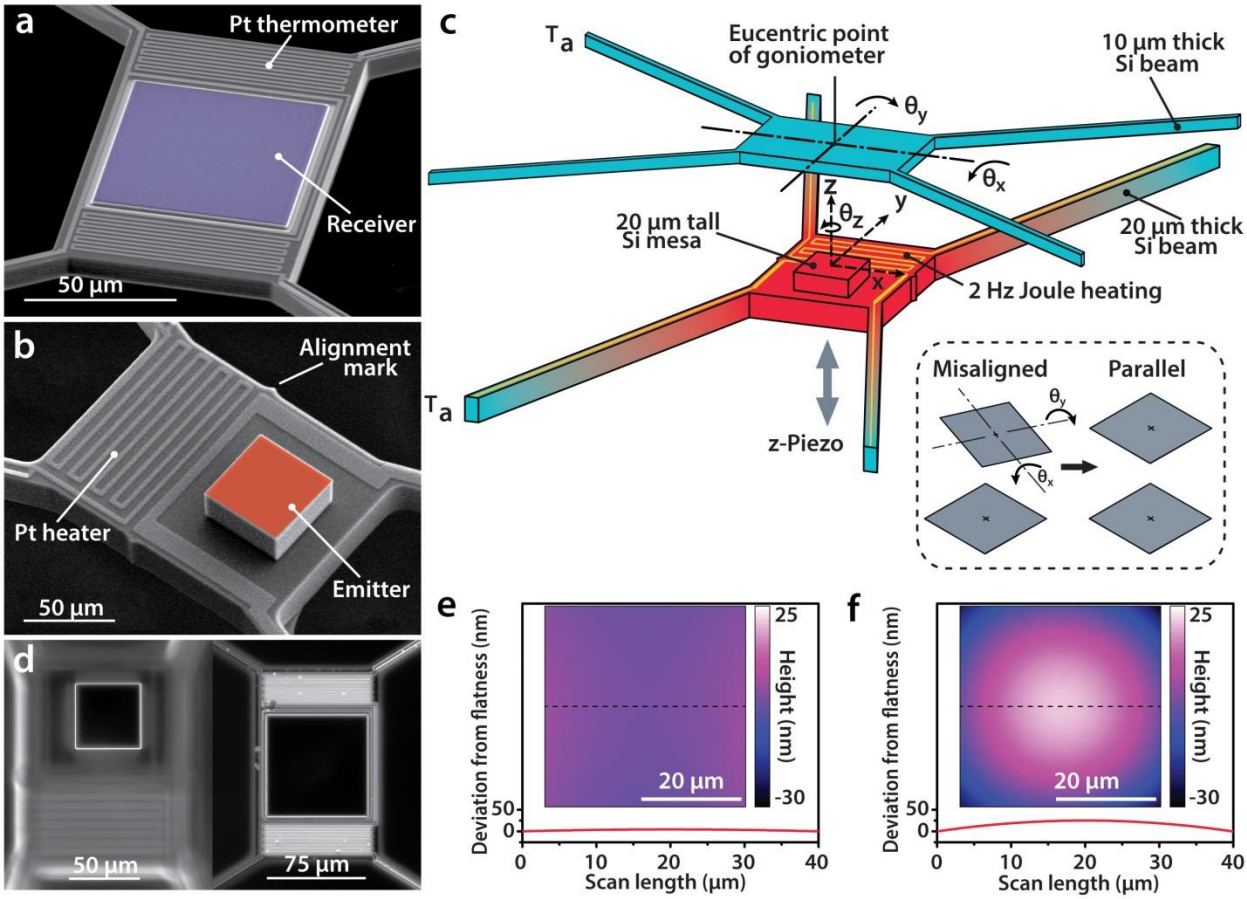

Figure 1.5: Microdevices for Probing Near-Field Radiation between Parallel-Planar Surfaces.
(a) Scanning electron microscope (SEM) image of the receiver device which features a 80 µm × 80 µm region that is coated with a desired dielectric/metallic film (false colored in purple). (b) SEM image of the emitter which features a 48 µm × 48 µm mesa-shaped region coated with SiO_2 or Au (top of mesa false colored in red). Both the emitter and receiver devices are suspended by long and narrow Si beams to achieve excellent thermal isolation. (c) Schematic showing the orientation of the emitter and receiver devices with respect to each other. The relative alignment of the emitter and receiver (inset) can be controlled via a custom-built nanopositioner. (d) Optical images showing the emitter and receiver devices. (e) A line profile of the active region of the emitter showing the negligible deviation from planarity along the dashed line of the inset. The inset presents the topography obtained using atomic force microscopy (AFM). (f) Same as (e) but for the receiver. Small deviations from planarity ~30 – 40 nm over a 40 µm × 40 µm region can be seen (dashed line aligned with the center line parallel to the *x*-axis of the receiver).

1.5e, f) and dark-field optical microscopy (Fig. 1.5d) confirmed that the devices are extremely flat and free of large particles, a critical condition for performing the desired nanoscale radiative heat transfer measurements in parallel-planar devices. Specifically, the largest deviation from planarity is seen in the receiver device, which is ~30 nm over a 40 µm × 40 µm region (see Fig. 1.5f). Further, particles were <40 nm in diameter on both the devices. For radiative heat transfer

measurements we parallelized and laterally aligned the emitter and receiver devices with respect to each other. To achieve this we leveraged a custom-built nanopositioning platform developed in our lab.[194] The degrees of freedom provided by the nanopositioner are shown in Fig. 1.5c and enable the translation of the emitter along the *x*, *y*, *z* directions and rotation about the *z* axis (θ_z), whereas the receiver can be rotated about the *x* and *y* axes (θ_x, θ_y). Manipulating the devices via the nanopositioner while visualizing the devices under an optical microscope enables parallelization to within 100 - 200 nm deviation over the 48 μm × 48 μm overlap region of the emitter and receiver devices. Subsequently, the emitter, which is laterally displaced from the receiver during the initial parallelization, is shifted laterally and placed vertically right beneath (~10 μm) the receiver device (Fig. 1.5a). Finally a high vacuum (1 μtorr) with minimal mechanical vibrations is created via an ion pump to attenuate contributions to heat transfer from air conduction to negligible levels.

In order to characterize radiative heat transfer from the emitter to the receiver we modulated the temperature of the emitter sinusoidally at 2 Hz with an amplitude ΔT_{Emit} = 2 K, via the integrated Pt heater. Next, the emitter device was displaced towards the receiver with nanometer-precise control via a piezoelectric actuator while we simultaneously record the amplitude of sinusoidal (2 Hz) temperature oscillations of the receiver (ΔT_{Rec}) via the Pt temperature sensor integrated onto the receiver device. The gap (*d*) dependent radiative conductance $G_{Rad}(d)$ between the emitter and the receiver is given by:

$$G_{Rad}(d) = G_{Rec} \times \Delta T_{Rec}(d)/(\Delta T_{Emit} - \Delta T_{Rec}(d)), \tag{1.18}$$

where G_{Rec} is the thermal conductance between the isolated region of the receiver and the Si substrate to which it is connected by thin and long beams, which was characterized to be 94.6 μW/K.

We first probed radiative heat transfer between emitter and receiver devices coated with a 2 μm-thick layer of SiO_2, which at nanoscale gaps provides an excellent approximation to bulk SiO_2 as the film thickness is much larger than the gap size[195]. Contact is indicated by a simultaneous jump in both the optical signals and the temperature signal, the latter of which arises due to an increase in thermal conductance associated with heat conduction upon contact.

The gap-dependent radiative conductance for SiO_2-SiO_2 surfaces (Fig. 1.6a, green squares) increases dramatically before contact is established. We found that the maximum measured near-field conductance could be enhanced systematically by tipping and tilting the receiver with respect to the emitter to further improve parallelism. Figure 1.6a shows the improvement that is achieved upon such systematic optimization. It is also apparent that the conductance exceeds the blackbody limit, reaching a value of 1 μW/K just before contact. We estimate from the known angular resolution of our nanopositioner[194] that this optimization approach reduces any deviations from parallelism to be a few nm across the 48 μm × 48 μm regions over which the emitter and receiver devices have near-field interactions.

In order to compare the experimental results with theory we first computed the thermal conductance per unit area $h_{Rad}(d)$, for the SiO_2 thin-film coated plates using Eqn.1.17. Next, we computed the radiative thermal conductance from $G_{Rad}(d) = h_{Rad} \times A_{device}$, where A_{device} is the area of the mesa (48 μm × 48 μm). The computed total conductance for ideal, parallel SiO_2 surfaces is shown as the black line in Fig. 1.6b. In order to more accurately estimate the thermal conductance in our devices, which feature small deviations from planarity, we employed the Derjaguin approximation[1, 195-197] to compute the near-field conductance between the planar

emitter and the receiver. The computed total conductance after accounting for curvature of the receiver is shown in green in Fig. 1.6b.

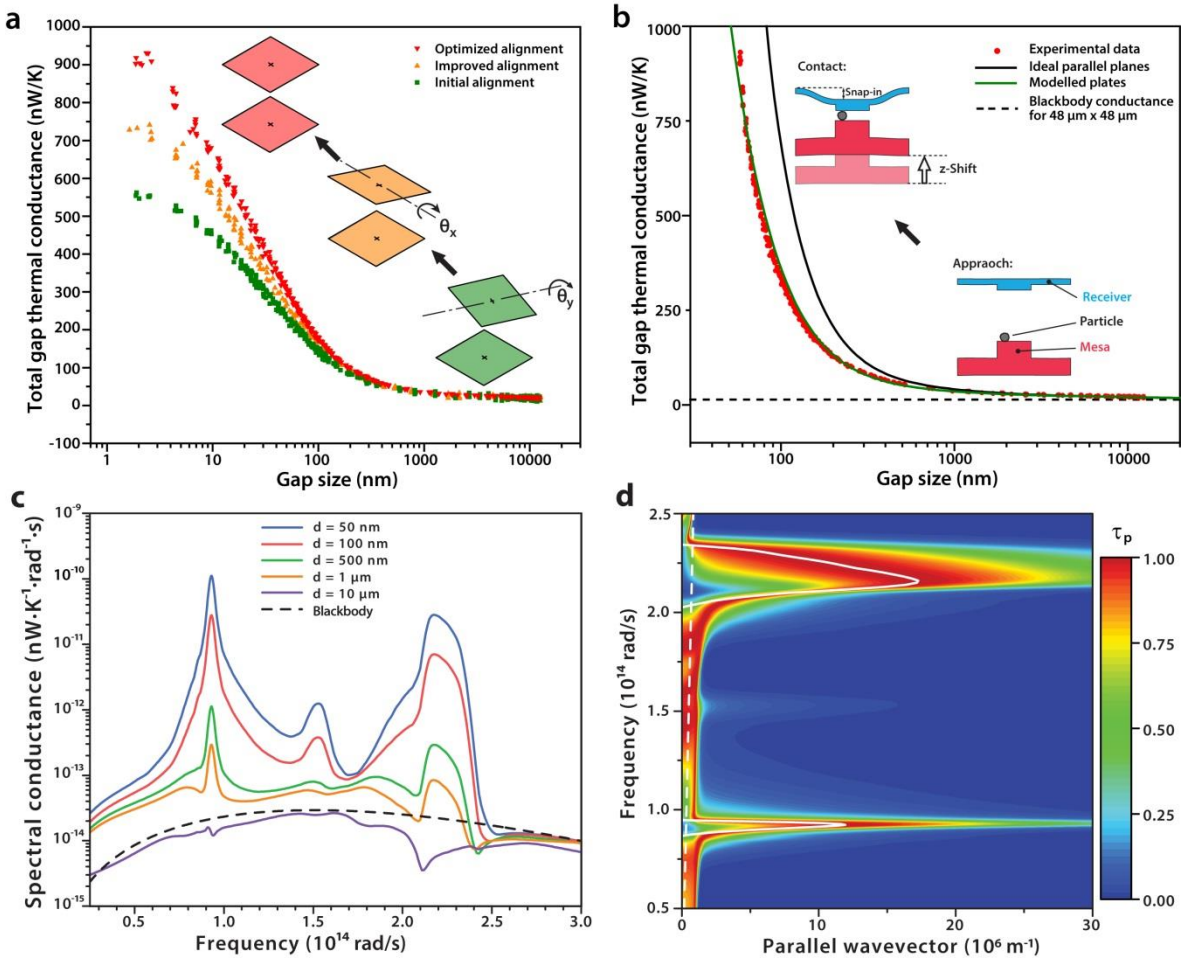

Figure 1.6: Optimization of Parallelization and Demonstration of Enhanced Heat Conductances in Sub-100 Nanometer Gaps between SiO_2 Surfaces.
(a) The observed enhancement in radiative heat transfer upon optimization of the parallelism by angular tilts θ_x, θ_y along the x and y axes, respectively. Insets show the approach followed to improve alignment. (b) Comparison of the experimentally measured radiative thermal conductance with computational data. Black solid line presents computed conductance for ideal parallel planes, whereas the green line presents computed conductance that accounts for small deviations in planarity. The dashed line presents the radiative conductance between two 48 μm × 48 μm planar blackbody surfaces with a view factor of unity. Insets show how the minimum achievable gap size is limited by the presence of nanoscale particles and snap-in. Data is from eight different measurements. (c) Computed spectral heat conductance between 2 μm thick films deposited on Si for various gap sizes. The spectral conductance between blackbodies is also shown for comparison. (d) Computed, normalized transmission for TM modes that dominates radiative heat transfer is shown along with the dispersion for surface phonon polaritons at a gap size of 50 nm (dashed line represents the dispersion of light in vacuum). It can be seen that the transmission is very large in the region where the dispersion curve (white solid line) of surface phonon polaritons (SPhPs) overlaps with the transmission plot, clearly indicating the role of SPhPs in enhancing radiative heat transfer.

To compare the results of our experiments with theory, it is also necessary to account for the presence of small particles of up to 40 nm in size, which are present on the microfabricated emitter and receiver devices. Further, the smallest achievable gap size before contact is also limited by snap-in, which is ~20 nm (inset of Fig. 1.6b). We followed well-established approaches[195-197] to account for the presence of particles and snap-in by noting that these factors limit the smallest possible gap size between the devices, just before contact, to ~60 nm (~40 nm due to particles + ~20 nm due to snap-in). To reflect this minimum gap size, the measured conductance data in Figs. 3b and 4a were displaced by 55 nm and 60 nm, respectively.

It can be readily seen (Fig. 1.6b) that the measured conductances for SiO_2 are in excellent agreement with the computed conductances. Further, it can be seen that the total conductance of the interacting area (48 μm × 48 μm) of the emitter and receiver increases ~100 fold compared to the total far-field conductance, assuming an emissivity of 0.84 for bulk SiO_2[85]. This dramatic enhancement is entirely consistent with theoretical predictions shown in Fig. 1.6c, which presents the spectral conductance for SiO_2 surfaces at various gap sizes. Specifically, it can be seen that large enhancements arise from huge contributions to heat transfer from two relatively narrow frequency ranges. As described in previous works[156, 195], these contributions arise from surface phonon polaritons whose signature can be seen in the computed transmission plot, which is overlaid on their dispersion relation (Fig. 1.6d). It also becomes obvious from this plot that the computed transmission for TM modes, which completely dominate radiative heat transfer, reaches their highest values in regions where cavity surface phonon polaritons are supported.

After demonstrating the large enhancements between SiO_2 plates, we performed experiments in which the emitter and receiver devices were coated with Au. Following the protocol described above, we obtained the radiative conductance for various gap sizes. The

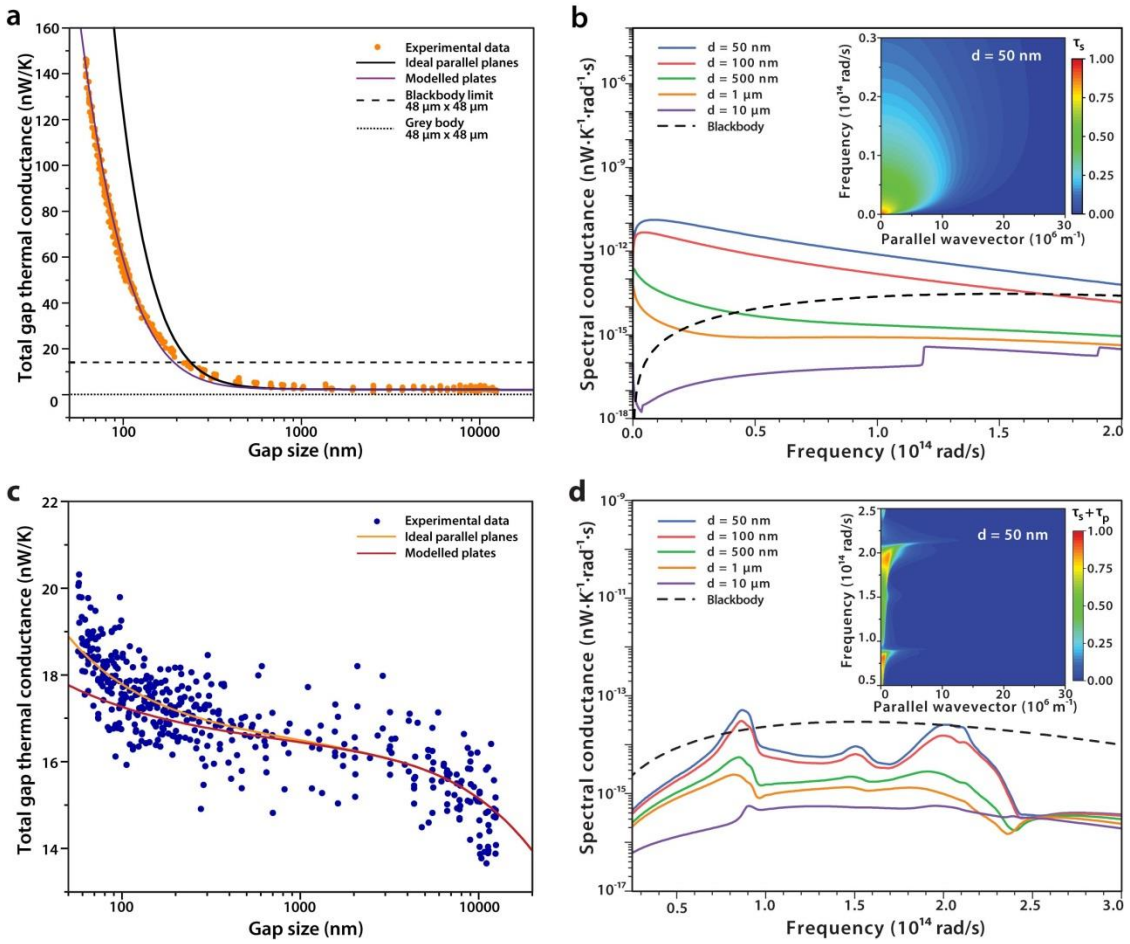

Figure 1.7: Enhanced Heat Conductances in <100 nm Sized Gaps of Au Surfaces and Near-Field Radiation between Dissimilar Surfaces.
(a) Comparison of the experimentally measured radiative thermal conductance for Au-Au with computational data. The black solid line presents computed conductance for ideal parallel planes, whereas the purple line presents computed conductance that accounts for small deviations in planarity. The dashed line presents the radiative conductance between two 48 μm × 48 μm planar black surfaces with a view factor of unity. The dotted line presents the computed far-field conductance for 48 μm × 48 μm planar Au surfaces with a view factor of unity and the appropriate emissivity for Au (0.02). Data is from nine different measurements. (b) Computed spectral conductance curves for Au-Au along with the transmission at a gap size of 50 nm (inset) for TE modes that dominate radiative heat transfer. (c) Measured thermal conductance for mismatched parallel-planar surfaces, SiO_2-Au. Data from 10 different measurements. The solid lines show the computed radiative conductance for ideal planes and for planes that feature small deviations from planarity. (d) Computed spectral conductance for SiO_2-Au gaps and the total transmission probabilities for TE and TM modes, respectively. Note the much smaller heat conductance compared to Au-Au and SiO_2-SiO_2 surfaces.

conductance (at optimized receiver parallelization) obtained after displacing the measured data by 60 nm (similar to the case outlined for SiO_2) is shown in Fig. 1.7a, along with the computed thermal conductance. Again, the agreement between theory and experiment is very good. Further, we obtain an ~1000-fold enhancement (see Fig. 1.7a) in radiative conductance compared

to the far-field conductance between the interacting areas. Moreover, the obtained nanoscale conductances are also found to be ~10 times larger than the blackbody limit.[9] The computed spectral conductances for Au surfaces are shown in Fig. 1.7b, along with the transmission plot for the TE modes (inset). As expected[162], the near-field enhancements for Au surfaces feature contributions from a broad range of frequencies and do not have dominant contributions from resonant surface modes.

Finally, to demonstrate the versatility of our experimental platform and to illustrate the critical role played by dielectric resonances in near-field enhancements, we performed radiative heat transfer measurements between a SiO_2 surface and Au surface. The measured data along with the corresponding calculated near-field conductance (after offsetting the data by 55 nm) is shown in Fig. 1.7c. For the case of surfaces with mismatched dielectric properties, the radiative enhancements are much lower than those for surfaces with matched dielectric properties. These measurements are indeed consistent with computed spectral conductance curves (Fig. 1.7d) and transmission (inset of Fig. 1.7d) for SiO_2-Au surfaces, which suggests that near-field radiative heat transfer for SiO_2-Au surfaces is orders-of-magnitude lower than that for SiO_2-SiO_2 or Au-Au surfaces.

The advances developed as part of this study enabled the systematic studies of a variety of near-field based thermal phenomena and thermophotovoltaic devices described in the subsequent chapters.

1.9 Dissertation Outline

The parallel planar geometry is particularly important for demonstrating some of the applications described previously. Specifically, both thermal diodes and near-field TPVs require

parallel planes separated by vacuum gaps smaller than 100 nm for best performance, but the tools for accomplishing this did not yet exist. In this dissertation, I describe the development of those necessary tools, the demonstration of novel results in prototype systems, and an outlook for future study and prospects for these technologies.

In Chapter 2, I describe a modified approach for measuring near-field radiative heat transfer between parallel plates separated by nanoscale gaps, using only a single microdevice. I report a 1,200-fold enhancement, with respect to the far-field value, in the radiative heat flux between parallel planar SiO_2 surfaces separated by gaps as small as ~25 nm. The experimental methods described in Chapter 2 enable the work for the subsequent chapters.

In Chapter 3, I demonstrate thermal rectification at the nanoscale between doped Si and VO_2 surfaces. I show that the metal-insulator transition of VO_2 enables achieving large contrasts in heat flow near room temperature when the sign of temperature gradients are changed. I further show that the rectification increases at the nanoscale, with a maximum rectification coefficient exceeding 50% at ~140 nm gaps and a temperature difference of 70 K. Computational modeling indicates that this high rectification coefficient arises due to broadband enhancement of heat transfer between metallic VO_2 and doped Si surfaces, as compared to narrower-band exchange that occurs when VO_2 is in its insulating state.

In Chapter 4, I describe the creation of near-field thermophotovoltaic systems to demonstrate, for the first time, how the thermophotovoltaic power output increases dramatically when the gap size is reduced to nanometers. I characterized this enhancement over a range of gap sizes, emitter temperatures, and for photovoltaic cells with two different bandgap energies, and observed a 40-fold enhancement in the power output at 60 nm gaps relative to the far-field.

These results establish how near-field radiation can be used to extract relatively high power from a low-temperature source.

Finally, in Chapter 5, I summarize the work described in this dissertation and speculate on future directions.

Chapter 2: Giant Enhancement in Radiative Heat Transfer in Sub-30 nm Gaps of Plane Parallel Surfaces

Anthony Fiorino, Dakotah Thompson, Linxiao Zhu, Bai Song, Pramod Reddy, and Edgar Meyhofer

2.1 Abstract

Radiative heat transfer rates that exceed the far-field Planckian limit by several orders of magnitude are expected when the gap size between plane parallel surfaces is reduced to the nanoscale. To date, experiments have only realized enhancements of ~100 fold as the smallest gap sizes in radiative heat transfer studies have been limited to ~50 nm by device curvature and particle contamination. Here, I report a 1,200-fold enhancement, with respect to the far-field value, in the radiative heat flux between parallel planar silica surfaces separated by gaps as small as ~25 nm. Achieving such small gap sizes and the resultant dramatic enhancement in near-field energy flux is critical to achieve a number of novel near-field based nanoscale energy conversion systems that have been theoretically predicted but remain experimentally unverified.

2.2 Introduction

Nanoscale thermal radiation has been computationally studied[1, 24, 199] for several decades now to understand the physics of near-field radiative heat transfer (NFRHT). Further, more

recently several groups have computationally explored the utility of nanoscale thermal radiation for near-field thermophotovoltaics[69, 70, 76], near-field based refrigeration[200] and near-field based heat flux control using metamaterials[119, 122], nanostructured surfaces[137, 201], and phase-change materials[58, 65, 202]. Recent experimental work[195-197, 203-210] has succeeded in performing key experiments to address the physics of near-field thermal transport and experimentally demonstrated that significant increases in radiative heat transfer, compared to the far-field, can be achieved when the gap size between plane parallel surfaces is reduced to distances smaller than the thermal wavelength[211] (~10 μm at room temperature[85]). In fact, recent work has shown that heat transfer rates exceeding the blackbody limit by ~100 fold can be achieved when the gap size between plane parallel silica surfaces is reduced to ~55 nm. In spite of these impressive advances, it should be noted that a large body of computational work[1, 24, 69, 70, 76, 200] on near-field based energy conversion and thermal management has highlighted that achieving even smaller gaps sizes of ~30 nm and below is critical for exploring efficient and high power output energy conversion as the energy transfer rate increases dramatically with decreasing gap sizes.

To elaborate on recent progress, researchers have probed NFRHT between parallel planar surfaces in a multitude of experiments that employ either macroscopic[99, 185, 186, 212] (~1 cm × 1 cm) or microscopic[2, 213, 214] planar surfaces (49 μm × 49 μm, as determined by optical microscopy). Probing NFRHT using macroscopically large parallel plates[99, 185, 186, 212] is conceptually simple but practically challenging due to difficulties in both parallelization and in achieving pristine and smooth surfaces over large areas. These challenges have limited the smallest achievable gaps sizes to ~100s of nm. In contrast, microscopic devices[2, 213, 214] have less stringent constraints in parallelization[194] and in characterizing surface characteristics but are more challenging to fabricate. Recently, researchers have employed nanofabricated microdevice

structures to study NFRHT in sub-100 nm gaps[2, 213, 214]. However, in practice, the sophisticated fabrication techniques and achievable geometries have limited systematic exploration of NFRHT-based applications. Here, I describe a key advance that employs a simpler system than previous approaches[2] while achieving smaller vacuum gaps (~25 nm) that result in a >1000-fold enhancement in heat fluxes compared to the far-field limit and an order of magnitude improvement over the largest heat fluxes reported to date.

2.3 Experimental Methods, Results, and Analysis

In this new approach we employ a microscopic emitter/calorimeter device (henceforth just called "emitter"), and a macroscopic plate (Fig. 2.1a). The emitter microdevice (Fig. 2.1b) is fabricated from Si (see Ref.[2] for fabrication details), and features a 20 μm-tall, 50 μm × 50 μm square mesa. The top surface of the mesa, which is the portion that will come into the near-field of the receiver, is coated with a 2 μm-thick SiO_2 layer and is extremely flat and clean with ~10 nm deviation from planarity and ~20 nm particles/roughness, as characterized via atomic force microscopy (Fig. 2.1c, left panel). A serpentine Pt resistor deposited next to the mesa serves two simultaneous purposes: 1) it is used as a heater to elevate the temperature of the emitter by 13 K relative to the ambient, and 2) it is used as a thermometer to measure temperature changes of the emitter. Conversely, the receiver is a macroscopically large (1 cm × 1 cm) plate cut from a pristine Si wafer after a 2 μm-thick layer of SiO_2 had been thermally grown. The surface of the receiver device was also characterized via atomic force microscopy and found to be extremely flat and clean (Fig. 2.1c, right panel).

I parallelized and laterally aligned the emitter and receiver in the configuration shown schematically in Fig. 2.1a using a custom-built nanopositioner[2, 194, 195]. For both the emitter device and receiver plate, this nanopositioner allows for lateral alignment in the *x*- and *y*-

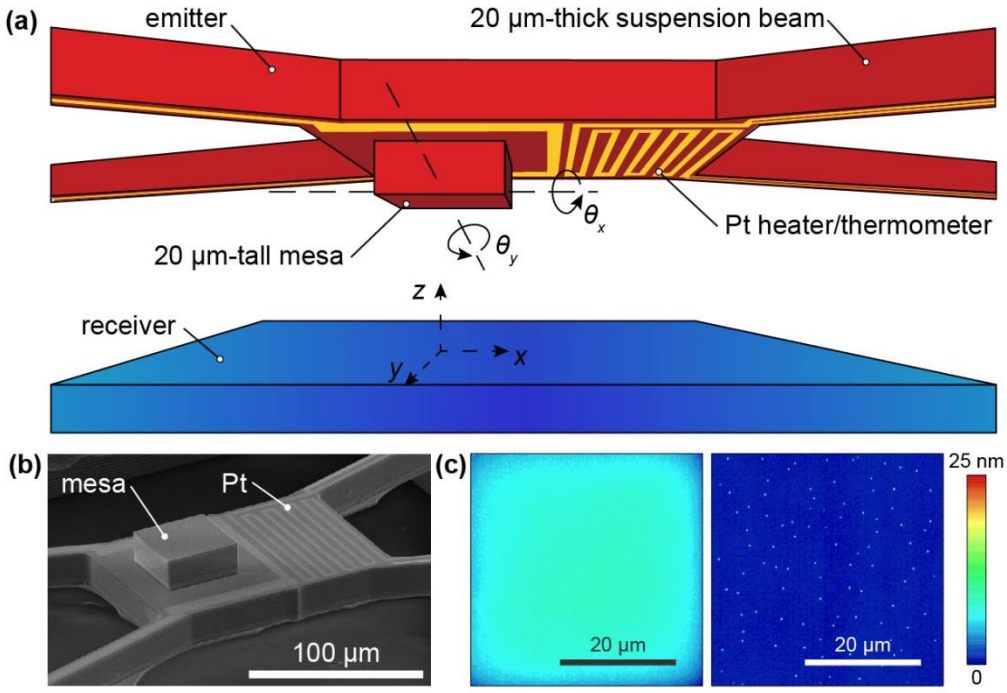

Figure 2.1: Experimental Setup and Devices for Giant Enhancement in Radiative Heat Transfer
(a) Schematic illustration of the NFRHT measurement configuration. The emitter microdevice is comprised of a square mesa and Pt heater/thermometer suspended on a thermally isolated island. The receiver is a macroscopically large (1 cm × 1 cm) plate. (b) Scanning electron micrograph of the emitter device. The 20 μm tall, 49 μm × 49 μm wide mesa is heated to reach a temperature that is 13 K above ambient using the Pt heater. (c) Atomic force micrographs of the top surface of the mesa (left) and the receiver surface (right). Both micrographs share the same color bar for ease of comparison.

directions with a precision of a few micrometers, as well as fine (6 μrad) rotations about the *x* and *y* directions (θ_x and θ_y). Further, the receiver plate can be translated via piezoelectric actuation along the *z*-direction in steps as small as ~2 nm. The process of parallelizing the emitter and receiver plate is broadly carried out in two sequential steps: 1) "coarse" parallelization is carried out under a 50× optical microscope, and later a "fine" parallelization is performed by optimizing the radiative heat transfer between emitter and receiver prior to contact (see section 2.4 for details). Finally, the nanopositioner is located in a high vacuum system to eliminate heat conduction through air, and suspended on an optical table to isolate the system from mechanical vibrations which would otherwise compromise the nanoscale gap between emitter and receiver.

To measure NFRHT between two SiO_2 films (each film was 2 μm thick, which is known to behave like bulk SiO_2 in the near-field[195]), I first raised the emitter temperature to 13 K above the ambient by passing a direct current through the integrated Pt resistive heater. Next, I displaced the receiver plate towards the emitter using a piezoelectric actuator. As the gap size (d) between the two devices is reduced, the emitter temperature changes by an amount $\delta T_e(d)$ (negative values correspond to a temperature reduction of the emitter) relative to the initial value. To quantify δT_e, I superposed a small-amplitude alternating current (436 Hz) onto the dc heating current, and subsequently locked-in to the resulting ac voltage using a lock-in amplifier in a 4-probe scheme. Since the temperature coefficient of electrical resistance (TCR) for the Pt heater/thermometer was determined to be 2.03×10^{-3} K^{-1} in a separate characterization measurement, the change in resistance could be used to directly calculate δT_e. Once δT_e was known, the heat flux q_{gap} across the vacuum gap could be calculated according to the thermal circuit diagram in Fig. 2.2a, giving:

$$q_{gap} = \frac{Q_{in} - G_{beam}(T_{e,i} - T_\infty + \delta T_e)}{A_{mesa}} + q_{far}, \tag{2.1}$$

where Q_{in} is the heat dissipated in the Pt heater, G_{beam} is the thermal conductance of the emitter suspension beams, $T_{e,i}$ is the initial emitter temperature and T_∞ is the ambient temperature (such that $T_{e,i} - T_\infty = 13$ K), A_{mesa} is the area of the emitter mesa (49×49 μm^2), and q_{far} (which cannot be measured directly in our scheme) is the computed radiative heat flux in the far field. Because the emitter cools as the gap size is reduced, δT_e is expected to become more negative as the emitter approaches the surface of the receiver. The heat input Q_{in} was calculated as the product of the heater voltage and the heater current. The thermal conductance of the suspension beams

was characterized to be G_{beam} = 110 μW/K (see section 2.4). Thus, I require only a measurement of δT_e in order to calculate the heat flux through the gap.

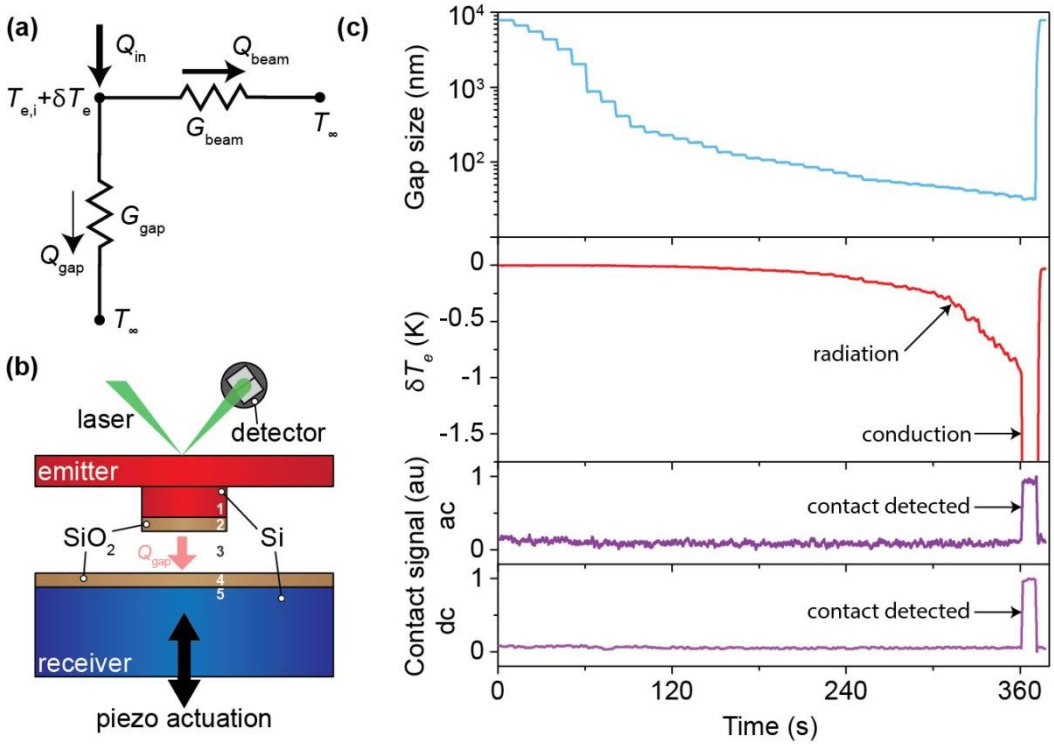

Figure 2.2: Scheme for Measuring Giant Enhancement in Radiative Heat Transfer
(a) Thermal resistance network that depicts the primary heat transfer pathways (G_{beam} is the thermal conductance of the emitter suspension beams and G_{gap} is the thermal conductance of the gap). When the gap is large, Q_{gap} is negligible. As the vacuum gap shrinks, the emitter temperature decreases due to the increased radiative thermal conductance of the vacuum gap. (b) Schematic side view of the devices depicting the key elements of an experiment. The receiver is displaced towards the emitter using piezoelectric actuation. Once the receiver makes mechanical contact with the emitter, a changed deflection of the laser (both ac and dc) is registered at the detector. (c) Time series data acquired during a single experiment. Top panel: Change of the vacuum gap size as a function of time. Second panel: Emitter temperature change δT_e relative to the initial $T_{e,i}$. The decrease in δT_e prior to contact is used to calculate the radiative heat flux q_{gap} across the vacuum gap. Third panel: Mechanical contact between the emitter and receiver is detected optically using a lock-in amplifier to monitor the ac component of the photodetector difference signal. Fourth panel: A step change in the dc component of the optical signal indicates contact.

In an experiment, I first positioned the receiver under the emitter and displaced it towards the emitter via piezoelectric actuation (Fig. 2.2b). I reflected a laser (Fig. 2.2b) off the back of the emitter to detect mechanical contact between the emitter and receiver, similar to the cantilever deflection detection scheme used in an atomic force microscopy (section 2.5). Figure 2.2c shows data acquired over the course of a single experiment. The top panel in Fig. 2.2c

depicts the change of the gap size over time, beginning at 8 μm and gradually decreasing to contact. Far away from contact, coarse steps of 1 μm are used, and the step size is gradually reduced to 2 nm prior to contact. I estimate that the effective gap size immediately prior to contact is ~25 nm based on the size of the largest particles on the emitter device's mesa. The second panel in Fig. 2.2c shows the measured δT_e over the course of the experiment. It can be seen that δT_e grows more negative as the gap size is reduced, indicating radiative cooling of the emitter prior to contact. The sudden drop in δT_e at contact occurs due to conduction. The third and fourth panels show, respectively, the ac and dc optical signals used to detect contact in the experiment (see section 2.4 for a description of contact detection). Both signals remain zero when the gap size is finite, but signals undergo a step change when the receiver and emitter come into mechanical contact.

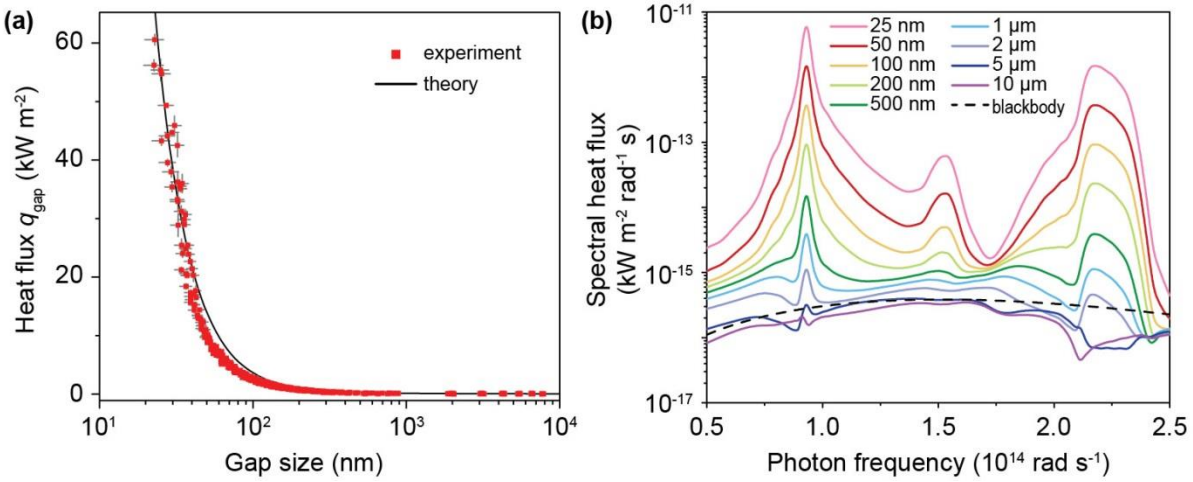

Figure 2.3: Measured and Calculated Giant Enhancement of Radiative Heat Transfer
(a) Heat flux vs. gap size. Measured data (red squares) is plotted directly alongside the theoretically computed expectation (solid black line). Horizontal and vertical error bars (gray lines) quantify uncertainty in the estimated gap size and measured heat flux data, respectively. Their precise meanings are discussed in the main text. (b) Computed spectral heat flux between 2 μm-thick SiO_2 films on semi-infinite Si substrates for selected vacuum gap sizes. The spectrum corresponding to blackbody exchange is also shown for reference.

I combined the gap size and measured δT_e values to extract the heat flux through the gap (q_{gap}) as a function of gap size as depicted in Fig. 2.3a. The red squares in Fig. 2.3a correspond to

the measured values of q_{gap}, which can be seen to increase by 1,200-fold as the gap size is decreased to 25 nm, from ~50 W/m^2 in the far-field to over 60 kW/m^2 at the smallest gap size. Each point represents a mean value for q_{gap} averaged over a 5-second sampling period. Vertical error bars (vertical gray lines) indicate the bound of ±1 standard deviation about the mean of the 5 second sample. Horizontal error bars (horizontal gray lines) indicate uncertainty in the gap position according to the minimum piezo step size (2 nm) plus 1 standard deviation in the measured piezo displacement (typically ~1 nm), for a total gap size uncertainty of ~6 nm. For visual clarity, error bars are only shown for data below 50 nm.

To compare my measured result to the theoretical expectation, I modeled the system by applying the framework of fluctuational electrodynamics[107]. Based on this approach, I approximated the geometry as a five-layer 1D system (layers labeled in Fig. 2.2b) and compute the expected heat flux q_{gap} from emitter to receiver according to

$$q_{gap} = \int_0^\infty \frac{d\omega}{4\pi^2} \cdot \left[\Theta(\omega, T_{e,i}) - \Theta(\omega, T_\infty) \right] \int_0^\infty \mathrm{d}k \cdot k \cdot \left[\tau_s(\omega, k) + \tau_p(\omega, k) \right], \tag{2.2}$$

where ω is the angular frequency of the radiation, Θ is the population term, k is the parallel wavevector, and $\tau_{s(p)}$ is the non-dimensional transmission term for s(p)-polarization. See section 2.4 for more details. If the optical properties of all materials in the 1D system are known, Eqn. 2.2 can be solved for the radiative heat flux. I model the two Si layers (Fig. 2.2b) using a dielectric function model from the literature[215], while the optical properties for the SiO_2 layers are interpolated from tabulated data[216].

I represent the theoretical expectation as a solid black line in Fig. 2.3a. It can be seen that the experimental data are generally explained well by the computed heat flux, as both curves

indicate a dramatic increase in the radiative heat flux below 100 nm. To better understand the source of this dramatic increase in heat flux, I plot in Fig. 2.3b the spectrum for the heat transfer from the emitter to the receiver. Because the heat flux across the gap is proportional to the area under the spectrum, identifying spectral regions for which the heat transfer is high yields information about the physical process driving the enhancement. In Fig. 2.3b I find that two relatively narrow peaks, one at 9.3×10^{13} rad/s and another near 2.2×10^{14} rad/s, dominate the heat flux spectrum. Since SiO_2 is known to support surface phonon polaritons in these two spectral regions[156], this is a good indicator that these surface modes are dominating the radiative heat transfer in our system in agreement with previous reports[22, 23, 32].

2.4 Conclusion

To summarize, I demonstrate a new method for measuring NFRHT between parallel plates for which both heating and thermometry is confined to a single microdevice. Using this novel approach, I achieved extremely small gap sizes (~25 nm) between plane parallel SiO_2 surfaces which in turn results in dramatic enhancements in near-field heat transfer—a 1,200 fold enhancement in radiative heat flux between parallel planar silica surfaces as compared to the far-field value, and a more than 700-fold enhancement relative to the blackbody limit. Because this new method is simpler than previous approaches I expect that it will finally be feasible to systematically conduct experimental studies of near-field enabled energy conversion, which is key to developing a new generation of thermophotovoltaic and solid-state refrigeration devices.

2.5 Methods and Supporting Information

Parallelization of Emitter and Receiver

Parallelization of the emitter and receiver devices is a two-stage process. In the first stage, called "coarse parallelization," I use an optical microscope objective (Zeiss LD EC Epiplan-Neofluar 50×/0.55 HD) with a shallow depth of field (2 μm) to image a region of the receiver chip. By bringing a particular region of the chip into focus, I can determine its relative *z*-position to within ~2 μm. Using the nanopositioner to tip and tilt the receiver until all areas of the chip are simultaneously in focus, I can achieve planarity to within 2 μm across the ~1 cm length of the receiver chip. This parallelism translates to a maximum angular deviation of ~200 μrad, or a ~10 nm deviation across the 50 μm active area length. I use the microscope objective and nanopositioner to repeat the same process with the emitter chip, which is ~8 mm in extent (~250 μrad deviation, or 13 nm across the 50 μm mesa length). Thus, it is in principle possible to achieve effective gap sizes as small as ~23 nm (estimated using 10 nm receiver deviation ± 13 nm emitter deviation) using coarse parallelization alone; in practice, however, the emitter mesa is not perfectly parallel to the rest of the emitter chip, probably due to residual stresses in the beams after fabrication. In order to truly reach gap sizes of ~25 nm, additional alignment is required.

The second stage of the alignment process, called "fine parallelization," is predicated on the idea that, for a given gap size, the radiative heat flux between perfectly planar surfaces is maximized when those planes are perfectly parallel, and is reduced for imperfect alignment. Based on this idea, I displaced the receiver towards the emitter and noted the radiative heat flux immediately prior to contact. I then used the nanopositioner to tip or tilt the emitter in steps of ~120 μrad before initiating another contact, again recording the radiative heat flux immediately prior to contact. By iterating on this approach until an optimum in heat flux was obtained, I

estimate a maximum deviation from parallelism of ~120 μrad per rotation axis, or ~12 nm across the 50 μm active area (2 axes × 150 μrad × 50 μm).

Optical Detection of Mechanical Contact Between Emitter and Receiver.

To detect mechanical contact between the emitter and receiver, I use a laser deflection scheme similar to that employed in atomic force microscopes. As schematically illustrated in Fig. 2.2b, I focused a laser onto the backside of the suspended emitter device and subsequently focused the reflected beam onto a two-piece segmented photodiode. When the receiver chip makes mechanical contact with the emitter device, the relatively compliant emitter device is displaced upwards, causing a sudden change in the difference in output of the two detector segments (which we call the "dc contact signal"), as seen in the bottom panel of Fig. 2.2c. To further confirm that the receiver and emitter are in fact in contact, I also modulated the position of the receiver by ~5 nm at 4 kHz and used a lock-in amplifier to monitor the 4 kHz component of the detector difference signal (called the "ac contact signal"). As can be seen in the third panel of Fig. 2.2c, the ac contact signal reads zero when there is a finite vacuum gap separating the emitter and receiver, but when they are in contact the receiver drives the emitter position at 4 kHz such that the locked-in ac signal suddenly jumps.

Determination of Emitter Beam Conductance

As can be seen in Eqn. 2.1, calculating the heat flux across the vacuum gap requires knowledge of the thermal conductance G_{beam} of the emitter suspension beams. Because I use a sinusoidal current to determine G_{beam}, I also require the thermal time constant of the emitter device, as explained below.

I use a modulation-based approach[217] to measure the temperature rise of the emitter island due to a sinusoidal heat input. I drive an alternating current with amplitude I_{1f} and frequency f through the Pt heater/thermometer on the emitter island. The sinusoidal current drives a sinusoidal temperature rise with amplitude ΔT_{2f} and frequency $2f$. A voltage component at frequency $3f$ develops across the Pt heater/thermometer according to $V_{3f} = \frac{I_f \alpha_0 \Delta T_{2f} R_0}{2}$, where R_0 = 3123 Ω is the electrical resistance and α_0 = 2.03 × 10^{-3} K^{-1} is the temperature coefficient of electrical resistance of the Pt heater/thermometer, each at the reference temperature (300 K). I measured the voltage V_{3f} with a custom-built circuit and lock-in amplifier over a range of frequencies f, as seen in Fig. 2.4a. It can be seen in Fig. 2.4a that for $2f$ > 5 Hz, the V_{3f} signal rolls off because of the thermal time constant of the emitter device. I thus chose $2f$ = 2 Hz to measure the thermal conductance of the beams, so that the attenuation was not more than 3%.

In the absence of near-field radiative heat transfer to the receiver device, heat flow from the emitter island to the environment is dominated by heat conduction through the suspension beams. Thus when I pass current I_{1f} through the Pt heater/thermometer as described above, I use the known power input Q_{2f} and measured sinusoidal temperature oscillations ΔT_{2f} to calculate the beam thermal conductance according to $Q_{\text{in}} = G_{\text{beam}} \times \Delta T_{2f}$. To reduce error, I repeated the measurement for a range of Q_{in} and fit a line to the resulting data (Fig. 2.4b) to determine G_{beam} = 109.8 μW/K. A 95% confidence interval calculated on the best fit curve indicates an error bound of ±0.8 μW/K, or less than 1% of the measured signal.

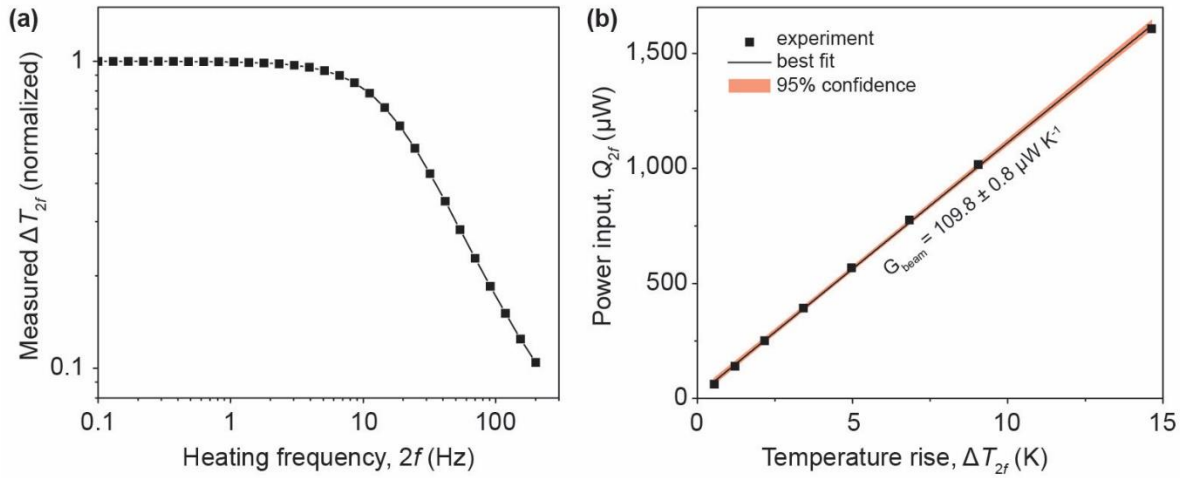

Figure 2.4: Determining Beam Thermal Conductance for Measurement of Giant Radiative Enhancement
(a) Measured thermal frequency response of our emitter microdevice. The data has been normalized to the low-frequency limit. (b) Power input vs. measured temperature rise for the emitter device in vacuum. The best fit line indicates a beam thermal conductance of 109.8 μW K^{-1} and the 95% confidence interval indicates a high degree of certainty.

Theoretical Modeling of Near-Field Radiation

The thermal radiation model used in this study to predict the near-field radiative heat flux is based on Rytov's fluctuational electrodynamics[107, 218]. For a 1-dimensional, 2-body system composed of 5 layers (2 emitter layers, 1 vacuum gap layer, 2 receiver layers, as in Fig. 2.2b), I calculate the radiative heat flux $q_{01\to34}$ from layers 0 and 1 to layers 3 and 4 according to

$$q_{01\to34} = \int_0^\infty \frac{d\omega}{4\pi^2}\left[\Theta(\omega,T_{\mathrm{H}}) - \Theta(\omega,T_{\mathrm{L}})\right]\int_0^\infty dk\cdot k\cdot\left[\tau^{\mathrm{s}}(\omega,k) + \tau^{\mathrm{p}}(\omega,k)\right] \tag{2.3}$$

where ω is the angular frequency, $\Theta(\omega,T) = \dfrac{\hbar\omega}{e^{\hbar\omega/k_{\mathrm{B}}T} - 1}$, $T_{\mathrm{H(L)}}$ is the emitter (receiver) temperature, k is component of the wavevector parallel to the layers, and $\tau^{\mathrm{s(p)}}$ is the transmission term associated with photons with s-(p-)polarization. The transmission terms can be calculated according to

$$\tau^{\alpha=s,p}(\omega,k)=\begin{cases}\dfrac{\left(1-\left|\rho_{20}^{\alpha}\right|^2\right)\left(1-\left|\rho_{24}^{\alpha}\right|^2\right)}{\left|D^{\alpha}\right|^2} & \text{if } k<\dfrac{\omega}{c}\\ \dfrac{4\,\mathrm{Im}\left(\rho_{20}^{\alpha}\right)\mathrm{Im}\left(\rho_{24}^{\alpha}\right)\mathrm{e}^{-2\,\mathrm{Im}(k_{z,2})t_2}}{\left|D^{\alpha}\right|^2} & \text{if } k>\dfrac{\omega}{c}\end{cases} \tag{2.4}$$

where $D^{\alpha}=1-\rho_{20}^{\alpha}\rho_{24}^{\alpha}\mathrm{e}^{2ik_{z,2}t_2}$ is a Fabry-Perot-like denominator, $k_{z,m}=\sqrt{\varepsilon_m\frac{\omega^2}{c^2}-k^2}$ is the perpendicular component of the wavevector in layer *m*, t_m is the thickness of layer *m*, *c* is the light speed in vacuum, and ρ_{ml} is the total Fresnel reflection coefficient for non-adjacent layers *m* and *l*. The latter can be calculated according to

$$\rho_{20}^{\alpha}=\frac{\rho_{21}^{\alpha}+\rho_{10}^{\alpha}\mathrm{e}^{2ik_{z,1}t_1}}{1-\rho_{12}^{\alpha}\rho_{10}^{\alpha}\mathrm{e}^{2ik_{z,1}t_1}}\ \text{ and }\ \rho_{24}^{\alpha}=\frac{\rho_{23}^{\alpha}+\rho_{34}^{\alpha}\mathrm{e}^{2ik_{z,3}t_3}}{1-\rho_{32}^{\alpha}\rho_{34}^{\alpha}\mathrm{e}^{2ik_{z,3}t_3}}. \tag{2.5}$$

The Fresnel reflection coefficients for adjacent layers, ρ_{mn}, in Eqn. 2.5 above can be calculated as

$$\rho_{mn}^{s}=\frac{k_{z,m}-k_{z,n}}{k_{z,m}+k_{z,n}}\ \text{ and }\ \rho_{mn}^{p}=\frac{\varepsilon_n k_{z,m}-\varepsilon_m k_{z,n}}{\varepsilon_n k_{z,m}+\varepsilon_m k_{z,n}}, \tag{2.6}$$

where ε_m is the dielectric function for material comprising layer *m*. For this model, I set $t_1 = t_3 =$ 2 μm and varied the gap size t_2. Layers 0 and 4 are semi-infinite. Once the geometry of all layers is specified (i.e., all thicknesses t_m are fixed), the only free parameter in Eqn. 2.3 is the dielectric function. For the Si layers (0 and 4), I modeled the dielectric function using a modified Drude model[215]. The dielectric function for the SiO_2 layers (1 and 3) was interpolated from tabulated data[216].

2.6 Author Contributions

Pramod Reddy and Edgar Meyhofer conceived of and supervised the work. I, Linxiao Zhu, and Bai Song performed the experiments. I performed the calculations. Dakotah Thompson fabricated the microdevices.

Chapter 3: A Thermal Diode Based on Nanoscale Thermal Radiation

Anthony Fiorino, Dakotah Thompson, Linxiao Zhu, Rohith Mittapally, Svend-Age Biehs, Odile Bezencenet, Nadia El-Bondry, Shailendra Bansropun, Philippe Ben-Abdallah, Edgar Meyhofer, Pramod Reddy

3.1 Abstract

In this work I demonstrate thermal rectification at the nanoscale between doped Si and VO_2 surfaces. Specifically, I show that the metal-insulator transition of VO_2 makes it possible to achieve large differences in the heat flow between Si and VO_2 when the direction of the temperature gradient is reversed. I further show that this rectification increases at the nanoscale, with a maximum rectification coefficient exceeding 50% at ~140 nm gaps and a temperature difference of 70 K. Theoretical modeling indicates that this high rectification coefficient arises due to broadband enhancement of heat transfer between metallic VO_2 and doped Si surfaces, as compared to narrower-band exchange that occurs when VO_2 is in its insulating state. This work demonstrates the feasibility of accomplishing near-field based rectification of heat flow, which is a key component for creating novel nanoscale radiation based information processing devices and thermal management approaches.

3.2 Introduction

In a two terminal device, when the magnitude of the heat flow depends on the direction of the temperature gradient, the device is said to rectify the thermal current. Thermal rectifiers are thus thermal analogues to electrical diodes, and are often referred to as thermal diodes. Although fluid-based thermal diodes that rely on convection (e.g., heat pipes) have long been proposed and studied[220], solid-state thermal diodes based on thermal conduction or thermal radiation have received very little attention. Recently, it has been shown that radiative heat transfer between two bodies can be enhanced by orders of magnitude when the bodies are in the near-field of each other, i.e. when the spatial separation of those bodies is reduced to the nanoscale, well below the thermal wavelength[1, 24, 92, 199, 211] (~10 μm at room temperature). Because near-field radiative heat transfer (NFRHT) depends strongly on the coupling of evanescent modes[156, 199], which in turn depends strongly on the optical properties of the participating materials, it is to be expected that asymmetric systems with temperature-dependent optical properties can exhibit high thermal rectification factors. This approach has been explored in theoretical proposals for thermal diodes based on numerous material pairings, including SiC structures[54], dielectric coatings[56], doped Si films[55], and intrinsic Si and a dissimilar material[215]. However, the above theoretical proposals all required extremely small gaps (<50 nm) and/or large temperature differences (>100 K) to achieve rectification coefficients greater than ~30%.

Recently, the possibility of using phase-transition materials for NFRHT has garnered increased attention[57, 58, 65, 221-226]. Of particular interest has been vanadium dioxide (VO_2), which undergoes a phase transition from insulator below 68°C to a metal above that temperature[227]. This phase change causes a dramatic alteration of the infrared optical properties[228] of VO_2, leading to correspondingly dramatic changes in the NFRHT in response to relatively small

temperature changes of the VO_2 near the transition temperature[57, 202, 221, 229, 230]. Previous experiments[210, 230, 231] have explored rectification between VO_2 and SiO_2, in the far-field, with one study[231] showing that rectification coefficients exceeding 50% can be achieved. In this letter, we explore rectification in the near-field (where heat fluxes are much larger than those in the far-field and can exceed the blackbody limit of far-field thermal radiation) and demonstrate that rectification coefficients between VO_2 and doped Si can exceed 50% in the near-field for moderate temperature differences (70 K) and gap sizes (140 nm).

3.3 Experimental Methods, Results, and Analysis

My thermal diode comprises of two devices separated by a vacuum gap (Fig. 3.1a). The first device (Fig. 3.1b), which was fabricated from Si, features a 15 μm-tall, 80 μm diameter circular mesa. The top surface of the mesa, which comes into the near-field of the opposing VO_2 surface, is clean and flat (as characterized using atomic force microscopy, Fig. 3.1d), where the largest contaminating particles are ~40 nm in size and the surface exhibits negligible roughness. The mesa surface layer is P-doped, ~430 nm deep, to a carrier concentration of $\sim 2.7 \times 10^{20}$ cm^{-3}. Deposited directly next to the mesa is a serpentine Pt resistor, which serves two functions: 1) as a resistive thermometer for measuring temperature changes of the Si mesa, and 2) as a resistive heater for increasing the temperature of the mesa. The entire structure is suspended by long beams to localize temperature changes to the distal end. The second device is a C-sapphire wafer with 350 nm VO_2 deposited by pulsed laser deposition[232], diced to ~1 cm × 1 cm. See section 3.5 for deposition details. The sample was then fixed on top of a suspended glass capillary tube, as shown schematically in Fig. 3.1a and c. Further, I integrated a resistive heater and a thermistor onto the glass tube, in close proximity to the VO_2 sample. The resistor was used to

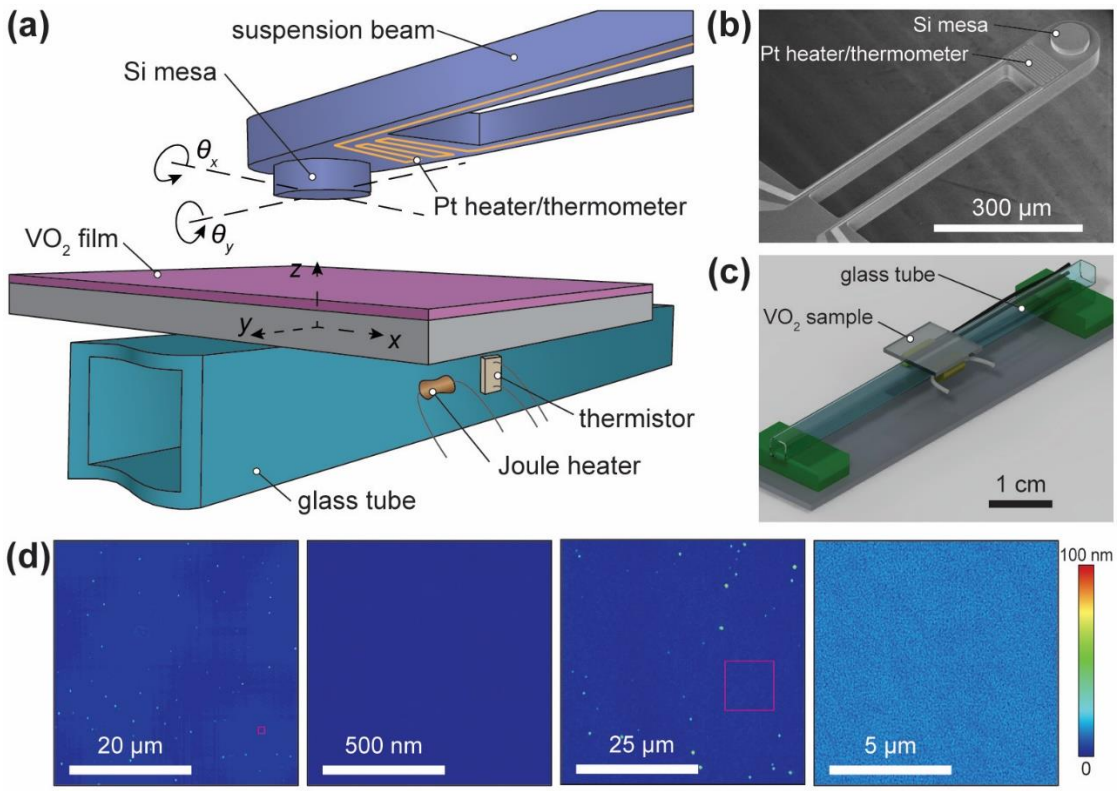

Figure 3.1: Experimental Setup and Devices for Near-Field Thermal Diode
(a) Schematic illustration of the radiative thermal diode with the relevant nanopositioning degrees of freedom indicated (not drawn to scale). (b) Scanning electron micrograph of the Si device, with mesa and Pt heater/thermometer. (c) Rendered image of the VO_2 sample stage, depicting the VO_2 sample at the center of the suspended glass tube. (d) Atomic force micrographs of the surfaces. A large-area scan (40 × 40 μm^2, first panel) of the Si mesa shows particles as large as ~40 nm, while a small-area scan (1 × 1 μm^2, second panel) showed negligible surface roughness. A large-area scan (50 × 50 μm^2, third panel) of the VO_2 sample revealed ~95 nm particles and a small-area scan (10 × 10 μm^2, right panel) displayed peak-to-peak roughness of ~20 nm.

dissipate heat so that the temperature of the VO_2 film could be elevated by values as large as ~100 K, whereas the thermistor was used for measuring the temperature of the VO_2 sample during the experiment. We note that the glass tube itself was suspended in vacuum (1×10^{-7} Torr) to minimize conduction through air and localize the temperature rise to the VO_2 sample only (Fig. 3.1c). I positioned the devices as shown schematically in Fig. 3.1a and parallelized them using a custom-built nanopositioner, which has been reported in detail elsewhere[2, 194, 195]. With this positioner, I simultaneously adjusted the gap size between the Si and VO_2 devices in steps as small as ~2 nm while parallelizing the surfaces such that the deviation from parallelism

is ~25 nm or smaller over the 80 μm diameter region where the Si mesa and the planar VO_2 sample interact via the near-field.

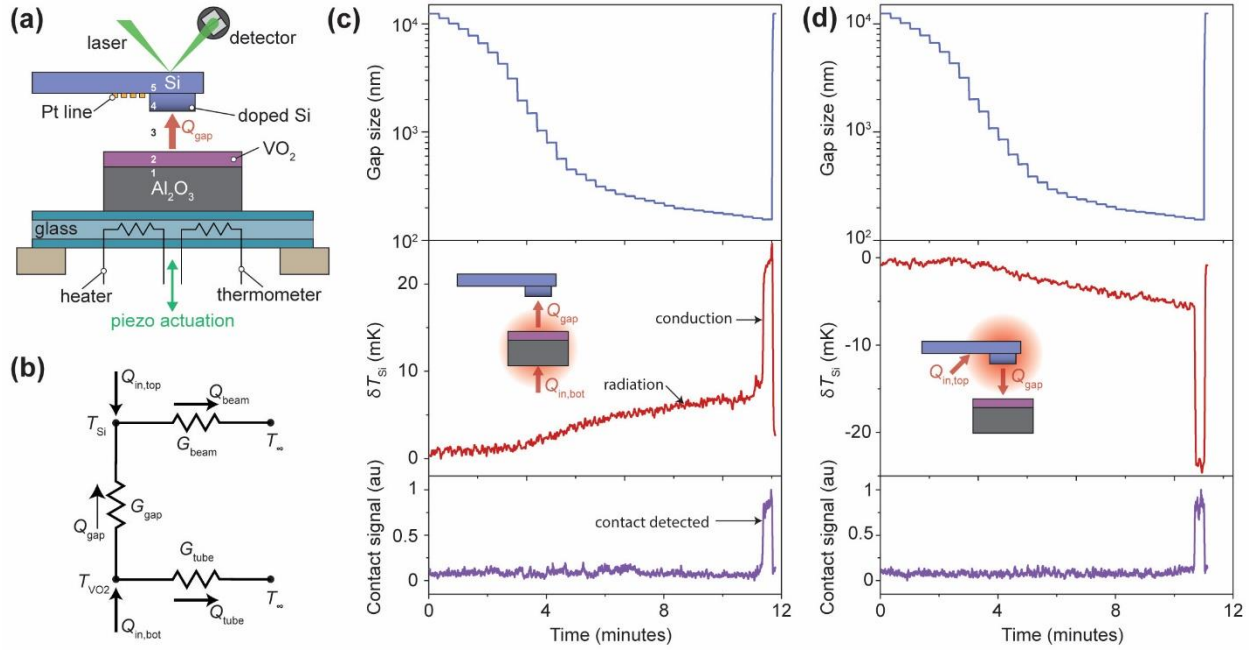

Figure 3.2: Scheme for Measuring Rectification of Heat Flow in Near-Field Thermal Diode
(a) Schematic side view of the suspended, microfabricated device and VO_2 on sapphire suspended on a glass tube (not drawn to scale). The temperature of both devices can be controlled and measured independently. The position of the bottom device is controlled via piezoelectric actuation. Deflection of the top device due to mechanical contact is detected optically. (b) Thermal resistance network showing the major heat transfer pathways in our system. (c) Time series data acquired during a single experiment, for which ΔT = +10 K (forward bias, i.e. $T_{VO2} > T_{Si}$, see middle panel inset). Top panel: Evolution of vacuum gap size over time. Second panel: Temperature rise δT_{Si} of the Si mesa device over time. Lower panel: Optical contact signal over time. (d) Same as in (c), but for an experiment with ΔT = -10 K (reverse bias, i.e. $T_{Si} > T_{VO2}$, see middle panel inset).

When the temperature of the VO_2 sample was elevated, heat flowed from VO_2 to Si, which I define as the *forward bias* case (see Fig. 3.2a). I achieved forward bias conditions by inputting heat $Q_{in,bot}$ (Fig. 3.2b) using a dc current in the resistive heater (Fig. 3.1a, Fig. 3.2a) on the glass tube which increased the temperature T_{VO2} of the VO_2 sample. I measured T_{VO2} using the thermistor mounted to the glass tube. For the first experiment, I chose $Q_{in,bot}$ such that T_{VO2} = 31°C. Reducing the size of the vacuum gap causes an increase in the gap thermal conductance, G_{gap}, due to near-field enhancements resulting in an additional near-field based heat current

$Q_{gap,NF}$ which causes the temperature of the Si device (T_{Si}) to rise by an amount $\delta T_{Si} = Q_{gap,NF}/G_{beam}$. I measured δT_{Si} by monitoring the temperature-dependent resistance of the integrated serpentine thermometer using a small sensing AC current, similar to my previous work[30] (described in Chapter 2), whereas G_{beam} was measured in a separate characterization measurement (see section 3.5). I calculated the near-field heat flow $Q_{gap,\,NF}$ through the vacuum gap from:

$$Q_{gap,\,NF} = G_{beam} \times \delta T_{Si}\,. \tag{3.1}$$

Figure 3.2c depicts time series data for a representative experiment in the forward bias configuration. After optimizing the parallelization of the devices using a two-stage approach[2], I systematically reduced the vacuum gap from ~12 μm to contact (Fig. 3.2c, top panel), using coarse steps (~1 μm) when the gap is large and fine steps (~2 nm) when the devices were in the near-field. I estimate the minimum gap size immediately prior to contact based on VO_2 sample roughness (~20 nm, Fig. 3.1d right panel), particle size on the VO_2 sample (~95 nm, Fig. 3.1d third panel), and parallelization resolution (~25 nm), and I accordingly shifted the minimum gap size by their sum, 140 nm (Fig. 3.2c, top panel). During the approach process, the temperature δT_{Si} of the Si device is continuously measured (Fig. 3.2c, middle panel) and is seen to steadily increase due to near-field radiative heat transfer, before suddenly increasing when the devices come into mechanical contact. To further confirm the contact position, I focused a laser onto the backside of the Si device and directed the reflected beam onto a position sensitive photodiode (Fig. 3.2a) so that deflections of the Si device could be observed in a fashion similar to atomic force microscopes. During experiments, I modulated the position of the VO_2 device with an amplitude of ~5 nm and used a lock-in amplifier to monitor the photodetector output (Fig. 3.2c, lower panel). When the devices were separated by a finite gap, the Si device remained stationary

and the optical signal was zero; at contact, the Si device moves together with the VO_2 device and the optical signal jumps, unambiguously indicating contact.

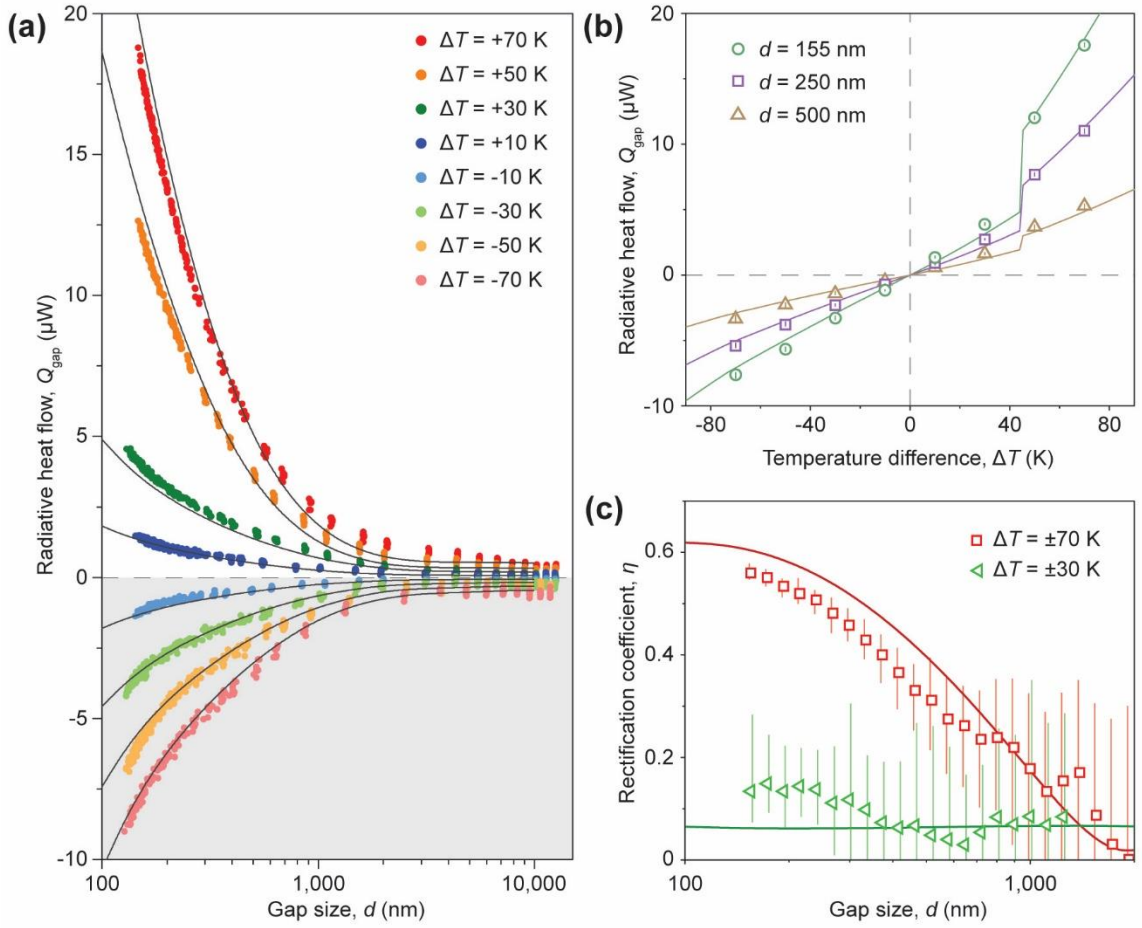

Figure 3.3: Measured and Calculated Heat Flow in Near-Field Thermal Diode
(a) Total radiative heat flow Q_{gap} vs. vacuum gap size d for eight values of $\Delta T = T_{VO2} - T_{Si}$. Data for the forward bias case are bright circles in the white region, while data for reverse bias are pastels in the gray region. Modeling results are represented by black lines. (b) Total radiative heat flow Q_{gap} (points) vs. temperature difference ΔT for three selected values of vacuum gap size d. Vertical error bars contained inside points indicate the maximum/minimum values measured. Modeling results are represented by solid lines. (c) Measured rectification coefficient η (points) vs. vacuum gap size d for $\Delta T = \pm 70$ K and $\Delta T = \pm 30$ K. Vertical error bars depict the full range of calculated values based on the error bars in (b). Modeling results are indicated by solid curves.

To estimate the total Q_{gap}, at a temperature differential of 10 K, I add the $Q_{gap,\ NF}$ (estimated from Eqn. 3.1 and data in Fig. 3.2c) and the far-field thermal conductance estimated from fluctuational electrodynamics[17, 18, 57] based calculations described below. The obtained Q_{gap} is shown as bold blue circles in the upper (white) region of Fig. 3.3a. In total I carried out the

above procedure for four different values of $\Delta T = T_{VO2} - T_{Si}$ (+10, +30, +50, and +70 K, which corresponds to T_{VO2} = 31, 52, 72, and 92°C, respectively), and the results are shown in Fig. 3.3a (bold colors, upper region). Each condition contains data from eight experiments. Importantly, the highest two temperature differences (ΔT = +50, +70 K) correspond to VO_2 temperatures above the phase transition temperature, i.e., the VO_2 is in its metallic phase. For all values of ΔT considered, Q_{gap} is seen to increase as the gap size is reduced (Fig. 3.3a), as expected due to the near-field contribution.

To obtain a quantitative characterization of the rectification in our radiative thermal diode, I next measured heat flow under conditions where $T_{Si} > T_{VO2}$, which I call the *reverse bias* case. For the reverse-biased system, I turned off the heating to the VO_2 sample ($Q_{in,bot}$ = 0) and instead dissipated heat ($Q_{in,top}$) in the Si mesa by superposing a relatively large DC current onto the comparatively small AC sensing current in the Pt heater/thermometer. The AC sensing current enabled me to measure the temperature (T_{Si}) of the Si device[30]. As the gap size is reduced and G_{gap} increases due to near-field effects T_{Si} decreases by a small amount $\delta T_{Si} = Q_{gap,\ NF} / G_{beam}(T_{Si})$. Note that this expression is the same as the forward-biased case, except here G_{beam} is expressed explicitly as a function of T_{Si} because it was found to decrease by as much as ~10% when T_{Si} = 92°C. As can be seen in Fig. 3.2d, the measurement proceeded analogously to the forward-biased case except that the sign of δT_{Si} changed, indicating cooling of the Si mesa device. I calculated $Q_{gap,\ NF}$ for the reverse-biased case from the measured δT_{Si} according to:

$$Q_{gap,\ NF} = G_{beam}(T_{Si}) \times \delta T_{Si} \ . \tag{3.2}$$

I measured the reverse-biased heat flow for four values of $\Delta T = T_{VO2} - T_{Si}$ (–10, –30, –50, and –70 K, which correspond to T_{Si} = 32, 52, 72, and 92°C, respectively). The results are shown

in Fig. 3.3a (pastel colors in the gray shaded region). Each ΔT contains data from eight experiments. For the reverse-biased case, all four values of ΔT correspond to VO_2 in its insulating phase. As was the case for the forward-biased case, the total thermal conductance Q_{gap} (obtained by adding $Q_{gap,\ NF}$ and the computed far-field thermal conductance from calculations described below) in the reverse-biased case is seen to increase in magnitude as the gap size is reduced (Fig. 3.3a) due to near-field radiative heat transfer; however, in contrast to the forward-biased case, for which the heat flow reaches almost 20 μW for ΔT = +70 K, the heat flow in the reverse-biased case does not exceed even half that value when ΔT = –70 K. This asymmetry of heat flow indicates thermal rectification.

To compare the measured results to what is theoretically expected, we computationally modeled our thermal diode using an established fluctuational electrodynamics[17, 18] based approach[57]. We approximated the diode as a one-dimensional system composed of five layers, for which the heat flow can be determined computationally provided that the geometry and optical properties are known. We model our five layers as illustrated schematically in Fig. 3.2a, with the thickness of the VO_2 layer as 350 nm, and the doped Si layer to be 430 nm deep with a P-dopant concentration of 2.7×10^{20} cm^{-3}. The optical properties for VO_2[228], intrinsic Si[215], sapphire[216], and doped Si[233] are taken from models and tabulated data presented in the literature. Calculating Q_{gap} (total thermal conductance) as a function of gap size for each ΔT yields the black curves in Fig. 3.3a, the degree to which these curves track the experimentally measured values indicates fairly good agreement. I note that the computed thermal conductance at 10 μm gap sizes was used to estimate the far-field thermal conductance which was added to the experimentally obtained data as stated earlier.

Because the hallmark of an electrical diode is its asymmetric *I*-*V* curve, it is useful to characterize the Q_{gap}-ΔT curve of our thermal diode. In Fig. 3.3b, I show the computed Q_{gap} vs. ΔT curve for three different values of the vacuum gap size. Experimental points (hollow shapes) in Fig. 3.3b were obtained by linearly interpolating from the experimental data in Fig. 3.3a and averaging over the eight interpolated values. Maxima and minima are indicated by vertical error bars, which are small enough to be contained inside the points. It is clear from Fig. 3.3b that the system exhibits the asymmetry characteristic of a thermal diode. Specifically, the forward heat flow when ΔT = +70 K noticeably exceeds the reverse heat flow when ΔT = -70 K. I overlaid the computationally modeled results onto the Q_{gap}-ΔT curve to aid in a comparison to the theoretical expectation and again find good agreement. The discontinuity in the curve at ΔT = 45 K (T_{VO2} = 68°C) occurs due to the VO_2 phase transition, and this feature appears to be represented well in our data.

I can further quantify the rectification coefficient η according to the definition

$$\eta = \frac{\left|Q_{gap,fwd}\right| - \left|Q_{gap,rev}\right|}{\left|Q_{gap,fwd}\right|}, \tag{3.3}$$

where $Q_{gap,fwd(rev)}$ represents the heat flow through the vacuum gap in the forward (reverse) bias condition. The rectification coefficient defined this way is a positive number that cannot exceed unity (since we define $Q_{gap,fwd} > Q_{gap,rev}$), so I choose to express it as a percentage. I compute η as a function of gap size for ΔT = ±70 K and report the results as red squares in Fig. 3.3c. For ΔT = ±70 K, the VO_2 is in different phases (metallic or insulating) depending on the direction of the temperature gradient, and likewise the rectification is seen to increase with decreasing gap, even exceeding 50% at gaps of ~140 nm. In contrast, when ΔT = ±30 K, the VO_2 phase remains unchanged regardless of the direction of the temperature gradient and almost no rectification is

observed, although a small η ~ 10% is detected due to the temperature dependence of the doped Si optical properties.

To gain insight into the physical mechanisms responsible for thermal rectification in the system, we extracted the spectral heat flux data from the mathematical model of a diode with a vacuum gap size d = 100 nm and a temperature difference ΔT = 70 K (Fig. 3.4a). In the forward bias configuration, the radiative exchange between the metallic VO_2 and the doped Si is seen to be significantly enhanced compared to the blackbody exchange over the entire frequency range of relevance. This enhancement is particularly dramatic at frequencies less than ~1×10^{14} rad/s, for which free electrons in both metallic media (VO_2 in metallic phase and doped Si) strongly absorb according to a Drude model. In the reverse bias configuration, however, the heat flux is significantly enhanced over a narrower frequency band and is strongly suppressed elsewhere, leading to a lower total heat flow through the system. Even though VO_2 in its insulating phase supports surface phonon polaritons in the frequency band from ~0.5×10^{14} to 1.5×10^{14} rad/s, the poor coupling between these modes and the doped Si leads to relatively modest enhancement in the near-field.

It is interesting to consider how changes to the design of the near-field radiative thermal diode would affect its performance. Besides vacuum gap size, we identified VO_2 film thickness and Si doping depth as important free parameters which could in principle be tuned in a relatively straightforward fashion. To ascertain the role played by layer thickness, we again turned to the computational model and calculated the rectification coefficient for VO_2 film thickness between 10 nm and ~1.5 μm, and for Si doping depths between 10 nm and ~15 μm (Fig. 3.4b). Here, I assumed a vacuum gap distance d = 100 nm and a temperature difference of ΔT = 70 K. It can be seen in Fig. 3.4b that thin doping depths are sub-optimal, and doping depths beyond ~300 nm are

effectively infinite. Thus, I expect that increasing the doping depth in our diode from 430 nm would have negligible effect on the rectification we measured in our system. However, an optimum in VO_2 film thickness does exist near 200 nm, which suggests that the design could be further improved by reducing the VO_2 film thickness from 350 nm to 200 nm, which should be addressed in future work. I note that other important parameters for optimizing the design include the doping concentration on the Si side, the choice of substrate on the VO_2 side, and the minimum vacuum gap size, but a comprehensive optimization of these factors falls outside the scope of this work.

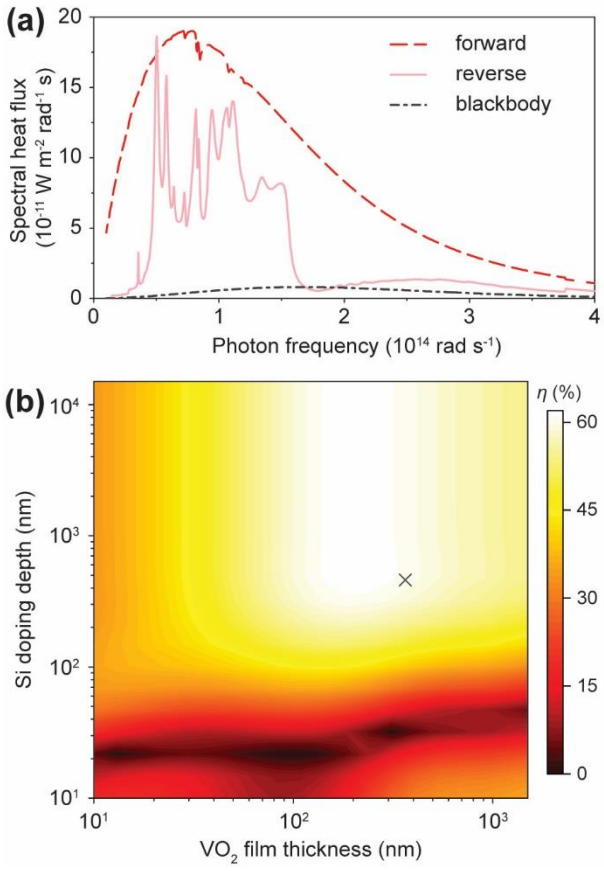

Figure 3.4: Computational Modeling of the Near-Field Radiative Diode
(a) Computed spectral radiative heat flux for both the forward and reverse bias conditions, calculated assuming a vacuum gap of d = 100 nm and a temperature difference of ΔT = 70 K. The calculated blackbody exchange is also shown for reference. (b) Computed rectification coefficient η for varying VO_2 film thicknesses and Si doping depths. The black "×" indicates the approximate conditions of our experiment.

3.4 Conclusions

In summary, I presented the first demonstration a near-field radiative thermal diode comprised of doped Si and a VO_2 film separated by a vacuum gap, and showed that rectification coefficients greater than 50% can be achieved by leveraging near-field radiative heat transfer across the nanoscale gap. Further, these results showed that the heat fluxes in these near-field diodes are much larger than what can be accomplished in the far-field. A mathematical model of the system highlighted the physical mechanisms responsible for this rectification and this model was used to predict the optimal thicknesses at which rectification ratios are maximized. The results and approaches developed here have important implications for probing novel near-field thermal devices such as diodes and transistors, which can significantly impact future heat-based computing and thermal management in nanoscale systems, energy conversion devices, and thermal circuits.

3.5 Methods and Supporting Information

Method for VO_2 Deposition

Films of VO_2 have been deposited by pulsed laser deposition on a substrate of sapphire-C (001). A V_2O_5 target was used for ablation with a KrF excimer laser at 248 nm. Oxygen pressure and temperature of the substrate have been optimized to obtain VO_2 films. X-ray diffraction analysis revealed a (010) preferred orientation. Scanning electron microscopy and atomic force microscopy analysis show a flat surface with a roughness RMS below 2 nm on a 1×1 μm^2 surface. Temperature-dependent Hall measurements have been performed to characterize the transition, which occurs at 68° C. Almost four decades are observed between the resistivity in the insulator state and in the metallic state[232].

Determination of Si Device Beam Thermal Conductance

Knowledge of the thermal conductance G_{beam} of the Si device suspension beams is critical to determining the heat flow through our diode in both the forward (Eqn. 3.1) and reverse (Eqn. 3.2) bias conditions.

The thermal conductance of the suspension beams was characterized at room temperature using a modulation-based scheme[217]. I pass a sinusoidal current with amplitude I_f and frequency f through the Pt heater/thermometer to heat the Si device with amplitude T_{2f} at frequency $2f$. A voltage component $V_{3f} = \frac{I_f \alpha T_{2f} R_0}{2}$ develops at $3f$, where α = 1.92×10^{-3} K^{-1} is the thermometer temperature coefficient of resistance and R_0 = 3755 Ω is the thermometer electrical resistance at 300 K. We measured V_{3f} for f = 1 Hz (chosen to be slow enough so that there is virtually no signal roll-off[234]) and several values of I_f, and obtained the relationship between $Q_{2f} = I_f^2 \times R_0$ and T_{2f} shown in Fig. 3.5. Fitting a line to the data gives a thermal conductance G_{beam} = 247.33 ± 0.86 μW/K, where the uncertainty corresponds to a 95% confidence interval on the fitted line.

In the reverse bias condition, the Si device reaches temperatures exceeding 90° C, and the thermal conductance is expected to deviate from the linear trend in Fig. 3.5 due to the temperature dependence of Si thermal conductivity[235]. Since the α for our Pt thermometer is not expected to remain constant to such high temperatures[236], the thermal conductance of the Si device beams could not be measured directly at elevated temperature using the technique described above. Instead, I extracted the thermal conductivity of the Si beams from previous measurements[234] in which a thermocouple was directly attached to the Si island during heating. Since these devices were fabricated from the same wafer, we assumed that the thermal conductivity in the Si device used in this work varied similarly.

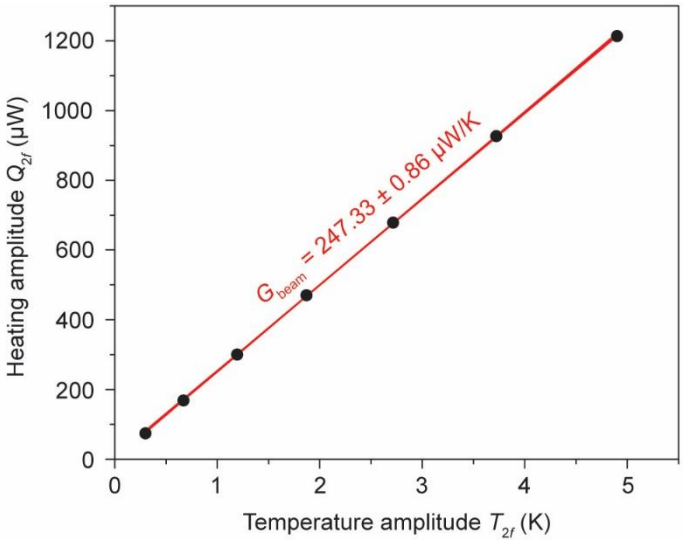

Figure 3.5: Determining Beam Thermal Conductance for Measurement of Near-Field Thermal Diode
Specified heating input amplitude vs. measured temperature amplitude for seven different values of heat input (black circles). A line fit and 95% confidence interval (red shaded area) are used to quantify the magnitude and uncertainty in beam thermal conductance G_{beam} near room temperature.

3.6 Author Contributions

Phillippe Ben-Abdallah, Edgar Meyhofer, and Pramod Reddy conceived the work. Edgar Meyhofer and Pramod Reddy supervised the experimental measurements. I and Linxiao Zhu performed the near-field radiative heat transfer measurements. Dakotah Thompson and Rohith Mittapally fabricated the microdevices. Odile Bezencenet, Nadia El-Bondry, and Shailendra Bansropun prepared the VO_2 sample. Phillippe Ben-Abdallah and Svend-Age Biehs performed the near-field heat flow calculations.

Chapter 4: Nanogap Near-Field Thermophotovoltaics

Reproduced with permission from *Nature Nanotechnology*. See Ref.[234]

Anthony Fiorino, Linxiao Zhu, Dakotah Thompson, Rohith Mittapally, Pramod Reddy and Edgar Meyhofer

4.1 Abstract

Conversion of heat to electricity via solid-state devices is of great current interest and has led to intense research into thermoelectric materials[237, 238]. Solid-state thermophotovoltaic (TPV) systems, where photons from a hot emitter traverse a vacuum gap and are absorbed by a photovoltaic (PV) cell to generate electrical power, have been proposed as an alternative to thermoelectrics, however, the low emitter temperature (<1000 K) typical of these applications severely limits the photon flux to the PV cell and the cell's power output. Hitherto unrealized theoretical proposals[69-71, 79, 80, 239-243] suggest that near-field (NF) effects[1, 20, 24, 199, 211, 244] that arise in nanoscale gaps may be leveraged to increase the photon flux to the PV cell and significantly enhance the power output. Here, using novel microfabricated devices and a custom-built nanopositioner, I describe functional NFTPV devices and show, for the first time, how the power output of TPV devices increases dramatically when the gap size is reduced to nanometers. I systematically characterized this enhancement over a range of gap sizes, emitter temperatures, and for PV cells with two different bandgap energies, and observed a 40-fold enhancement in the

power output at nominally 60 nm gaps relative to the far-field. These results establish how near-field radiation can be used to increase the power output of TPV devices. I anticipate that the technical advances and approaches presented here will spur the development of near-field based TPV devices for waste heat recovery.

4.2 Introduction

The power output of a TPV device is directly limited by the net flux of above-bandgap photons. While the most straightforward way to increase the electrical power output is by increasing the emitter temperature, which both increases the flux and shifts the peak wavelength to higher energies[85], that option is generally not available for waste heat recovery applications. Alternatively, the photon flux between hot and cold bodies can be greatly enhanced by reducing their spacing to less than the thermal wavelength[1, 20, 24, 199, 211], i.e. by placing the bodies in the "near-field" of each other (~10 μm at room temperature). The enhancement is due to evanescent fields associated with surface modes or total internal reflection modes. In fact, for sub-100 nm gaps, the radiative energy flux between parallel plates has been shown to increase by more than 100-fold for certain material systems[2]. The potential for leveraging this near-field radiative exchange in TPV systems has sparked renewed interest in TPV energy conversion and inspired many theoretical studies[69-71, 79, 80, 239-243]. While some qualitative experimental efforts to validate the expected potential of NFTPV have been made[68, 245], systematic studies of near-field based TPV have not been possible owing to the tremendous technical challenges involved in achieving and maintaining large temperature differences and stable nanoscale gaps between parallel planar surfaces. Recent technical advances in studying near-field radiative heat transfer[2, 212, 214] have, however, opened up new avenues to explore NFTPV.

4.3 Experimental Methods, Results, and Analysis

To directly demonstrate the performance enhancement achievable by NFTPV, I leveraged microscale devices for the thermal emitter and the PV cell. I use an emitter custom-fabricated from Si (see section 4.5.3 for fabrication details) with a 15 μm tall, 80 μm diameter circular mesa, seen in Fig. 4.1a. This extremely flat and clean mesa region (see section 4.5.5) is positioned in the near-field of the PV cell, and a serpentine Pt heater located next to the mesa is used to elevate the emitter's temperature up to ~655 K. The emitter structure is suspended by a simply-supported, thermally isolating double-beam 550 μm in length that effectively confines the temperature rise to the emitter island and eliminates buckling that may arise due to thermal expansion in fully-constrained structures as used in previous work[2]. The PV cell (Fig. 4.1b) is a commercially available photodiode (Electro Optical Components Lms36PD-03) with a 0.345 eV bandgap energy. This relatively narrow bandgap was chosen because of its suitability for harnessing power from low-quality waste heat (T ~ 655 K). The cell roughness was determined to be ~5 nm peak-to-peak (see section 4.5.5) via atomic force microscopy.

I parallelized and laterally aligned the emitter and cell using a custom-built nanopositioner, which is described in detail elsewhere[2, 194, 195]. Briefly, the nanopositioner affords several degrees of freedom, as schematically illustrated in Fig. 4.1c. Both the emitter and cell can be translated in the x and y directions and rotated about the x and y axes, (θ_x and θ_y) with ~6 μrad precision. Additionally, the cell can be translated along the vertical z direction via piezoelectric actuation, thus enabling control of the gap between emitter and PV cell to ~2 nm resolution. Parallelization of the emitter and the PV cell was carried out in two stages, first, using a high numerical aperture optical microscope and second, by optimizing the open circuit voltage (see section 4.5.1), achieving parallelism to within ~25 nm across the 80 μm mesa. Finally, the

positioner along with the NFTPV device was located in a high vacuum (~10^{-7} Torr) system and isolated from external vibrations via suspension on an optical table.

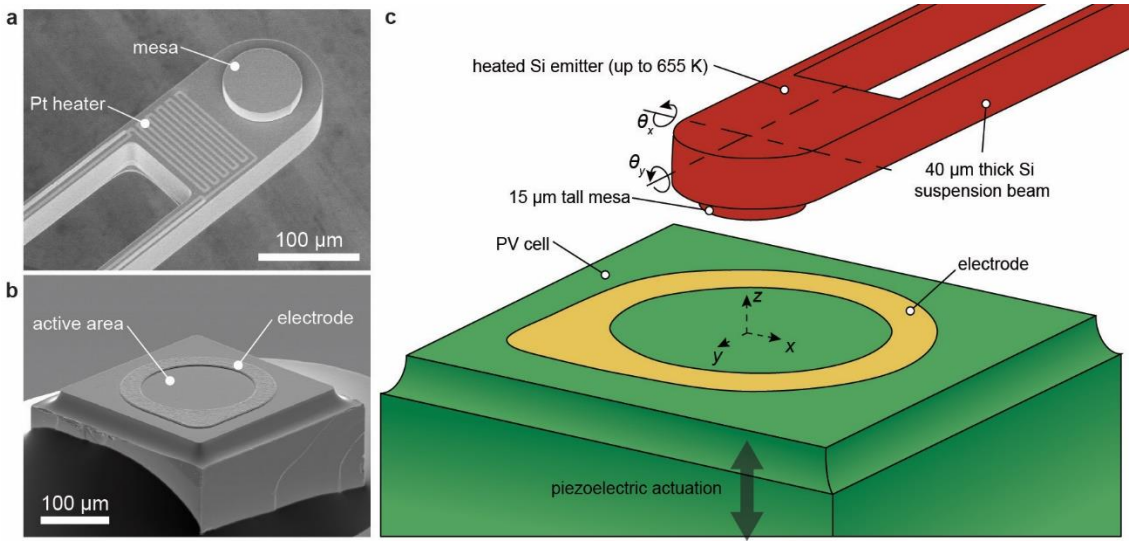

Figure 4.1. Experimental Setup and Devices for Nanogap Near-Field Thermophotovoltaics.
(a), Scanning electron micrograph of the emitter device. The 15 μm tall, 80 μm diameter mesa can be heated to ~655 K via the integrated Pt heater. (b), Scanning electron micrograph of the PV cell device which features a 300 μm × 300 μm active area which is partially obscured by the top electrode. In an experiment, the top electrode is accessed via wire bonding (not shown). (c), Schematic illustration of the TPV device orientation. Both devices can be translated in the *x*- and *y*-dimensions. Angular control of the emitter allows for parallelizing the devices and a piezoelectric actuator is used to precisely control the vacuum gap size.

I first investigated the power output from a TPV system with a bandgap of 0.345 eV. Towards this aim, the emitter was positioned directly above the PV cell (Fig. 4.2a) and a known amount of heat was dissipated in the emitter via Joule heating to systematically raise the emitter temperature, T_E, from room temperature to values as high as 655 K. The temperature rise of the emitter was carefully characterized via independent measurements ensuring that the uncertainty in the temperature rise was small (±5 K, see section 4.5.4). The temperature of the PV cell was not controlled but is estimated to remain near room temperature (temperature rises are ~1 K even for the highest emitter temperature). Next, using a source measure unit (Keithley 2401), I swept the cell current and measured the corresponding cell voltage. This yielded *I-V* curves that shift further into the first quadrant as the emitter temperature is increased, as shown in Fig. 4.2b. The

maximum power point, P_{MPP}, was calculated by locating the point on the *I*-*V* curve for which $I \times V$ is maximized (graphically shown as the shaded area in the inset of Fig. 4.2c).

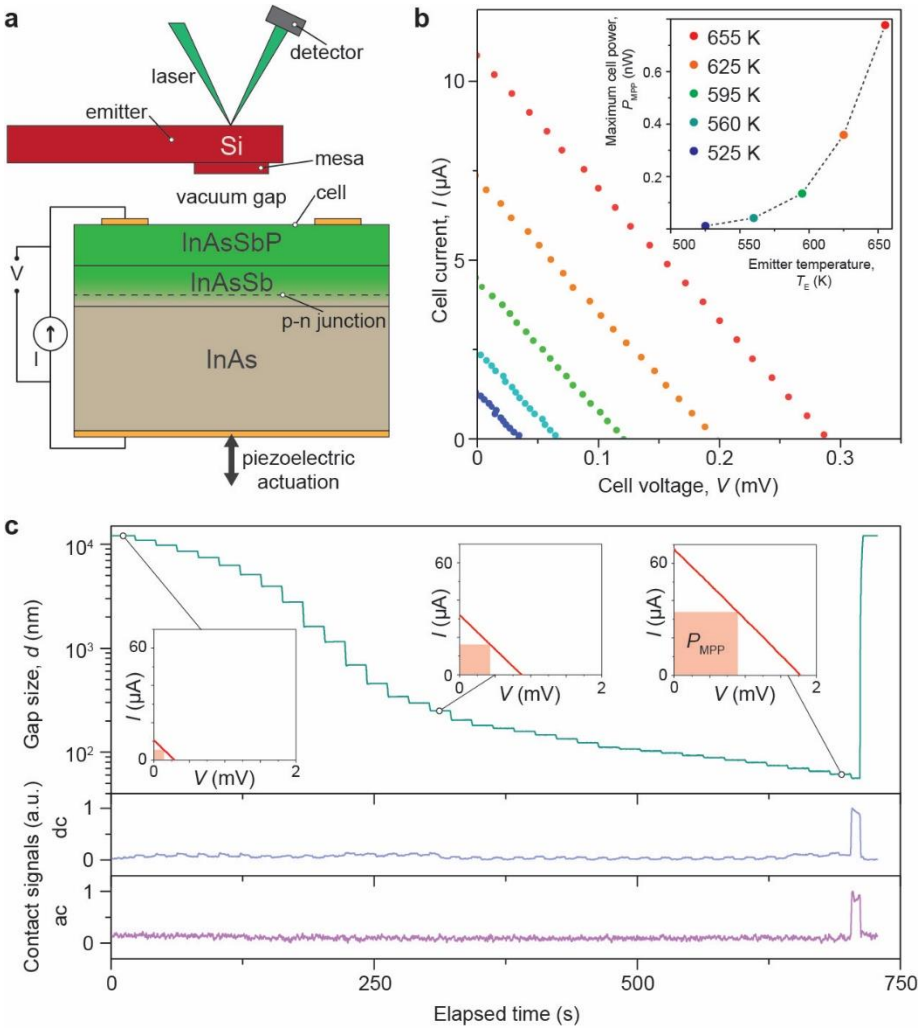

Figure 4.2. Scheme for Measuring Power Enhancement in Nanogap Near-Field Thermophotovoltaics.
(a), Schematic side view depicting the device architecture and measurement scheme. Photons are emitted from the hot Si emitter and absorbed in the InAsSb active layer to generate electron-hole pairs. By sweeping the current *I* and measuring voltage *V*, the cell's *I*-*V* characteristic can be obtained as a function of gap size. Contact is detected via a laser deflection scheme. (b), Cell *I*-*V* characteristic in the far-field for five different emitter temperatures ranging from 525 K to 655 K. As T_E is increased, the curves shift further into the first quadrant. The inset shows the power output at the maximum power point P_{MPP} for each choice of T_E. (c), Time series data for T_E = 655 K. Top panel: Evolution of the vacuum gap size over the course of a single experiment. PV cell *I*-*V* characteristics are taken during each step, and the inset shows three measured *I*-*V* curves at 12 μm, 215 nm, and 60 nm gap sizes (±6 nm). Middle panel: detection of contact based on dc change in the laser deflection. The sudden jump in the signal indicates a deflection of the emitter due to contact with the cell. Bottom panel: detection of contact based on locking-in to the 4 kHz component of the detector output.

To study the effect of gap size on the power output of our TPV devices, I displaced the cell towards the emitter using piezoelectric actuation and acquired *I-V* sweeps, yielding a family of *I-V* curves and maximum power points for each gap size. Figure 4.2c shows data from an experiment where the gap size was systematically reduced from ~12 μm to contact, in discrete steps, where the smallest steps (~4 nm) were taken near contact. At each step, an *I-V* curve was taken as described previously. The curves shift further into the first quadrant as the gap size decreases (inset of Fig. 4.2c top panel), indicating a higher electrical output power P_{MPP} when operating at smaller gaps. An optical detection method with a laser beam incident on the emitter and a split photo-diode, akin to approaches employed in atomic force microscopy, was adopted to detect contact between the emitter and PV cell (see Fig. 4.2a and section 4.5.2). Specifically, the deflection of the emitter was detected using two complementary approaches (see bottom panels of Fig. 4.2a), which sense the optical signal shift due to deflection of the emitter (called dc signal) and the signal due to modulation of the emitter deflection (called ac signal, see section 4.5.2). Both ac and dc optical signals remain unchanged until contact occurs, at which point they undergo a step change. Additionally, a large temperature drop in the emitter is observed as radiative heat transfer gives way to conduction (see section 4.5.6). Given the size of particles on the emitter (~55 nm), the PV cell roughness (~5 nm), and *z*-piezo resolution (~5 nm), I estimate that a minimum gap size of 60 ± 6 nm is achievable. The uncertainty of ±6 nm arises from summing the minimum piezo step size (4 nm), the piezo signal noise (1 nm), and effects from possible deviations from parallelism (1 nm). To reflect the minimum gap size of 60 nm, I offset the gap size at contact by 60 nm (Fig. 4.2c, top panel), consistent with previous work[2].

The measured *I-V* characteristic of our TPV system, at eight selected gap sizes, is reported in Fig. 4.3a. As the gap size was reduced from 12 μm to 60 ± 6 nm, the short circuit

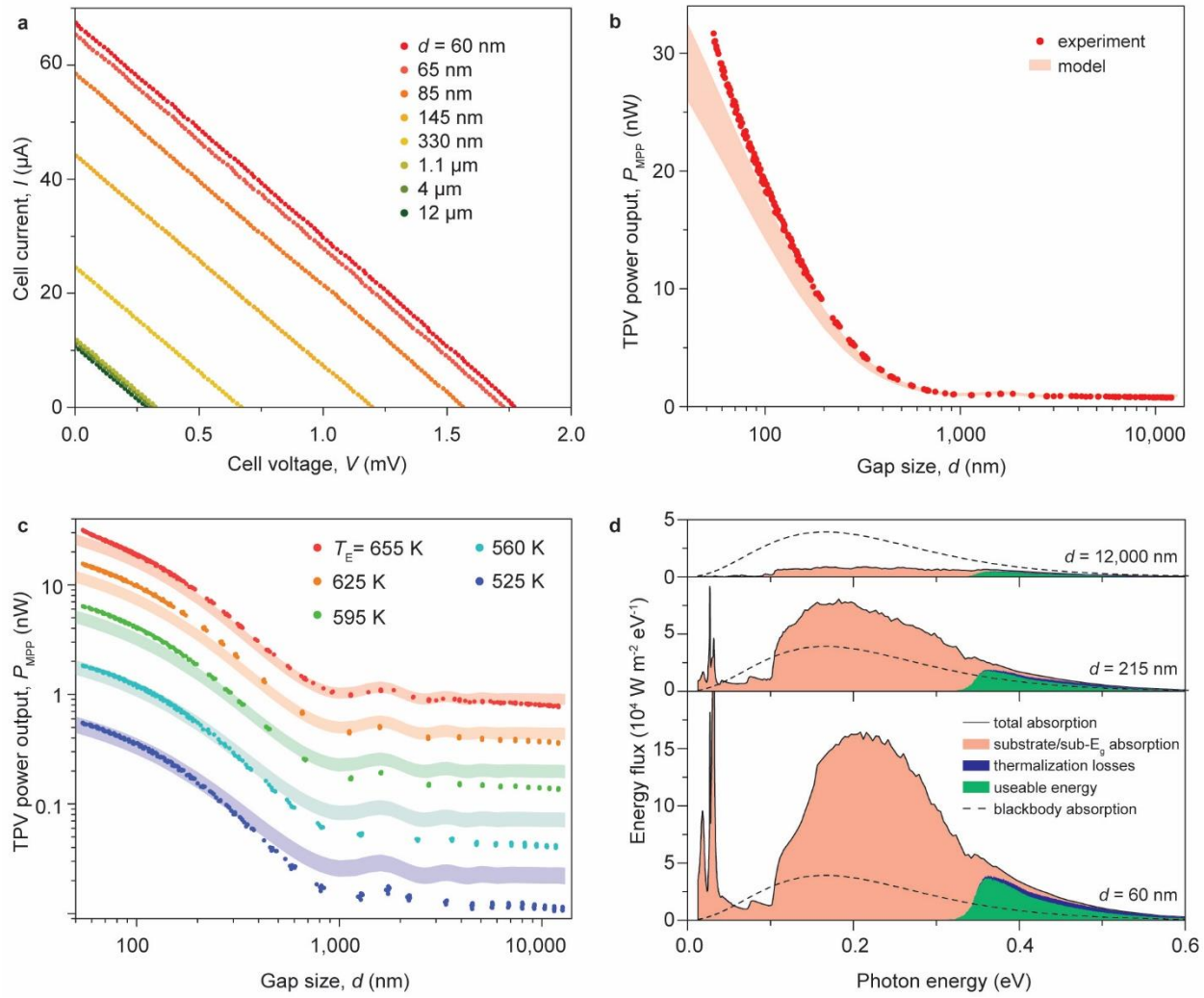

Figure 4.3. Measured and Calculated Performance in Nanogap Near-Field Thermophotovoltaics.
(a), Measured *I-V* curves at various gap sizes for the 0.345 eV-bandgap cell when T_E = 655 K. As the gap size decreases, the curve shifts further into the first quadrant. (b), Measured TPV power output P_{MPP} vs. gap size *d* for the 0.345 eV-bandgap cell when T_E = 655 K. When *d* = 60 ± 6 nm, P_{MPP} is enhanced 40-fold relative to the far-field. The shaded region indicates the theoretically expected values for 650 K < T_E < 660 K (c), Measured P_{MPP} vs. *d* for T_E ranging from 525 K to 655 K. The shaded regions indicate the theoretical expectation for the indicated T_E ± 5 K. (d), Calculated spectral energy flux for emitter temperature T_E = 655 K and gap size *d* = 60 nm (lower panel), 215 nm (middle panel), and 12 μm (upper panel), from our computational modeling. The green shaded region represents, for an ideal cell, the maximum energy extractable from above-bandgap photons absorbed in the active layer, while the blue region represents the excess photon energy lost to thermalization. The red shaded region represents lost energy due to photon absorption in the substrate/cladding layers as well as to below-bandgap absorption in the active layer. In our experiments, additional losses arising from non-radiative recombination are expected to reduce the output power to values below that shown by the green shaded region (see SI, Sec. 6).

current I_{sc} increased from 11 to 67 μA and the open circuit voltage V_{oc} increased from 0.29 to 1.77 mV. P_{MPP} is enhanced ~40 fold as the gap is reduced (Fig. 4.3b), from 0.77 nW in the far-field to 30.2 nW at the smallest gap size of 60 ± 6 nm. In addition, I repeated these

measurements for a range of emitter temperatures (T_E = 525, 560, 595, and 625 K in Fig. 4.3c), which clearly show, for example, that the power output for T_E = 525 K and d = 100 nm exceeds that for T_E = 625 K and d = 12 μm, further emphasizing that NFTPV operation across nanoscale gaps readily outperforms conventional TPV, even at significantly lower temperatures.

To compare our results to the theoretical expectation, we modeled the cell *I*-*V* characteristic by accounting for radiative and non-radiative contributions to the cell current (see section 4.5.9),

$$I(V) = I_{rad}(V) - I_{Auger}(V) - I_{SRH}(V), \tag{4.1}$$

where I_{rad} is the net current generated due to radiation, and I_{Auger} and I_{SRH} represent current lost to Auger and Shockley-Read-Hall (SRH) recombination, respectively. Because calculating I_{rad} requires knowledge of the above-bandgap photon flux, we modeled the system using fluctuational electrodynamics with a numerically-stable scattering matrix formalism (S-matrix)[246, 247] which enables computation of the radiative heat transfer between any pair of layers in a 1D system[153, 214, 248]. In our model we assume that each above-bandgap photon absorbed in the junction creates an electron-hole pair, and make use of the relevant electronic and optical properties (e.g. mobility, doping etc.) of the device materials obtained from previous work[249] (see section 4.5.8). Following the scattering matrix approach, the net photogenerated current I_{rad} is given by:

$$I_{rad}(V) = A_{mesa} e \int_{\omega_g}^{\infty} d\omega \frac{1}{\lambda^2} \left[\phi_{E\to J} \left(\frac{1}{e^{\frac{\hbar\omega}{k_B T_E}} - 1} - \frac{1}{e^{\frac{\hbar\omega - qV}{k_B T_J}} - 1} \right) + \phi_{A\to J} \left(\frac{1}{e^{\frac{\hbar\omega}{k_B T_A}} - 1} - \frac{1}{e^{\frac{\hbar\omega - qV}{k_B T_J}} - 1} \right) \right], \tag{4.2}$$

where $f_{1\to 2}$ is the computed transfer function from body 1 to body 2 (subscripts *E*, *J*, and *A* for emitter, junction, and ambient, respectively), and the meaning of the other variables is specified

in section 4.5.8. Note that this model requires two fitting parameters: the view factor f from the non-mesa region of the emitter to the cell is chosen so that our modeled power output matches the measured values in the far-field, and the surface recombination velocity S is determined by fitting the slope of the I-V curve to the measured data.

Because the model indicates that the TPV performance is sensitive to errors in emitter temperature of a few kelvin, and because our estimate of the emitter temperature has an uncertainty of ±5 K (section 4.5.4), I depict the theoretically computed data in Fig. 4.3b using a shaded region bounding $T_E \pm 5$ K. Comparing the experimentally measured data to the shaded region in Fig. 4.3b, the measured electrical output power (P_{MPP}) from the TPV system operating at 655 K is in reasonably good agreement with the computed expectation at all gaps. Similarly good agreement holds at all other emitter temperatures considered (Fig. 4.3c). Therefore, I believe that the model provides a reasonably accurate description of the experimental findings and further supports my conclusions regarding the enhancements observed in NFTPV. In Fig. 4.3d, I report the modeled energy flux spectrum from emitter to cell. The lower panel of Fig. 4.3d shows the computed spectral energy flux at the smallest gap (d = 60 nm) when the emitter is at 655 K. The green shaded region represents the maximum energy extractable by the TPV at this gap size, while the red and blue regions represent losses. At a 60 nm gap, the energy flux exceeds the limit for blackbodies by more than threefold, which leads to the observed enhancement in P_{MPP}. From investigating the distribution of transmission probabilities between the active layer of the cell and the emitter mesa in the (ω, k) plane (see section 4.5.11), I conclude that the near-field enhancement is due to contributions from frustrated total internal reflection modes that are able to tunnel through the vacuum gap when the gap size is reduced. The middle and upper panels show how the energy flux decreases with increasing gap size. In

the far-field, the energy flux is greatly diminished compared to blackbody exchange (Fig 3.3d, upper panel).

To clarify the effect of bandgap on the TPV performance, I repeated the measurement using a different PV cell with a slightly narrower bandgap, 0.303 eV (Electro Optical Components Lms41PD-03), for which I obtained the results shown in Figs. 3.4a & b. The minimum effective gap size attainable with this PV cell increased to 75 nm due to the increased surface roughness (53 nm peak-to-peak, section 4.5.5), leading to a slightly more modest power output enhancement of ~33-fold. To obtain a quantitative comparison between the 0.303 eV- and 0.345 eV-bandgap cells in our TPV system, I plot I_{sc}, V_{oc}, and P_{MPP} for both cells when T_E = 525 K (Fig. 4.4c) and T_E = 655 K (Fig. 4.4d). It is evident from Fig. 4.4c that at T_E = 525 K, employing the smaller bandgap cell improves the TPV power output: the increase in I_{sc} in the 0.303 eV cell more than compensates for the decrease in V_{oc}, leading to slightly higher P_{MPP} at a given gap. At higher temperatures, however, when the emission shifts to higher energy[85], the higher bandgap cell clearly outperforms its narrower-bandgap counterpart (Fig. 4.4d) in terms of the power output.

While the central goal of this work is to experimentally demonstrate that large power enhancements are possible in nanogap NFTPV devices, an analysis of the effect of gap size on efficiency is important in evaluating the performance of TPV systems. In the context of this work, I define the efficiency of the NFTPV devices as the ratio of electrical power (P_{MPP}) extracted to the net energy radiated from emitter to cell. Since it is not possible to measure the total radiated energy directly in our setup, I relied on the computational model to estimate the energy radiated across the gap and the P_{MPP}, from which I calculated the efficiency (Fig. 4.4e). The data suggest that efficiency is not a monotonic function of gap size in the NFTPV system; a

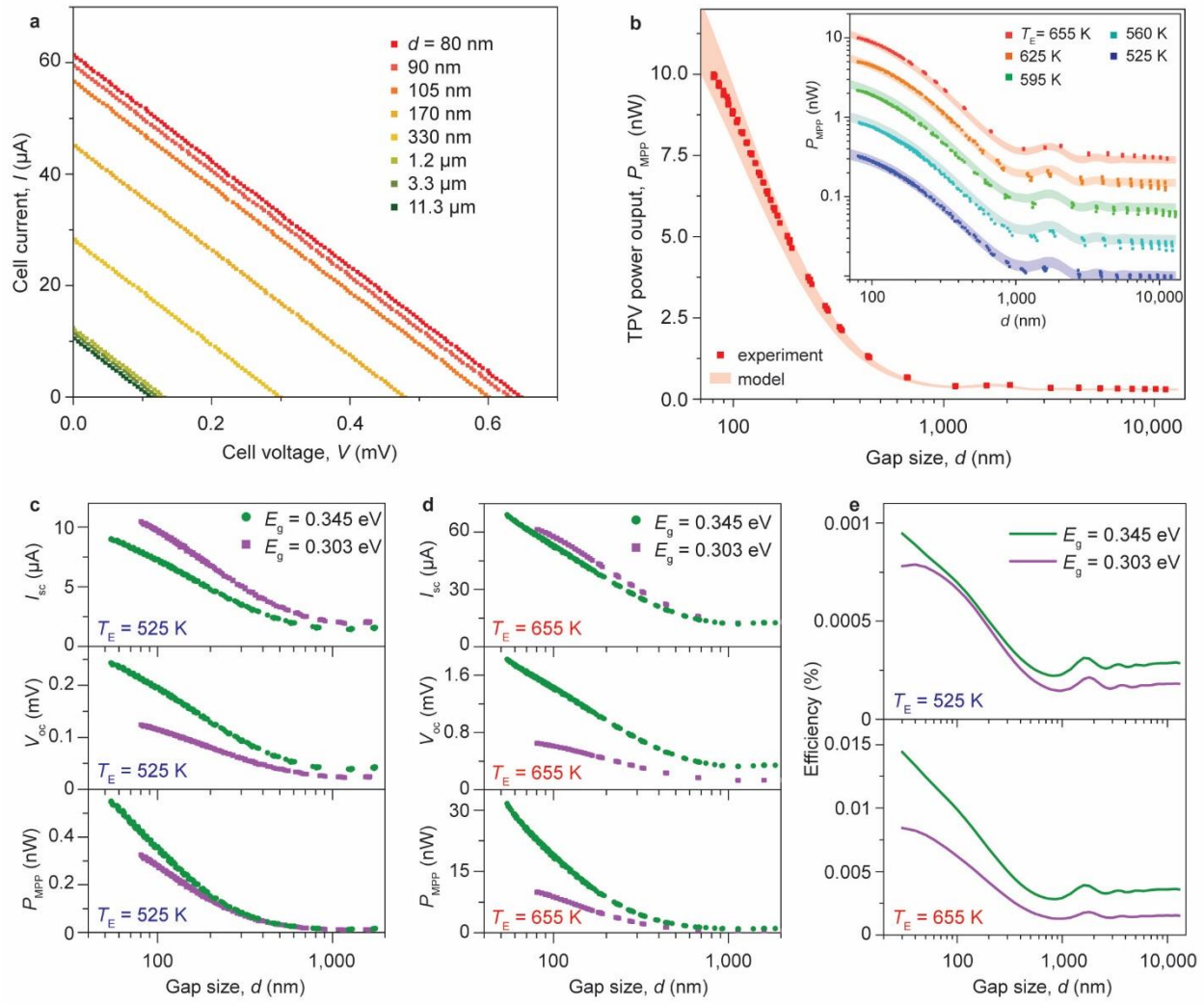

Figure 4.4. Measured and Calculated Performance Comparison Between Nanogap Near-Field Thermophotovoltaic Systems with Differing Bandgap Energies.
(a), Measured *I-V* curves at various gap sizes for the 0.303 eV-bandgap cell when T_E = 655 K. (b), Measured TPV power output P_{MPP} vs. gap size d for the 0.303 eV-bandgap cell when T_E = 655 K. When d = 120 nm, P_{MPP} is enhanced by a factor of 33 relative to the far-field. The shaded region indicates the theoretical expectation for T_E = 655 K ± 5 K from our modeling. Inset: Measured P_{MPP} vs. d for T_E in the range from 525 to 655 K (points), with modeled (shaded region). (c), Measured short circuit current I_{sc} (top panel), open circuit voltage V_{oc} (middle panel), and TPV output power P_{MPP} (lower panel) vs. gap size d for both cells at T_E = 525 K. (d), Same as in (c) but for T_E = 655 K. (e), Modeled TPV efficiency (defined in main text) for both cells when T_E = 525 K (top panel) and 655 K (bottom panel).

minimum in efficiency occurs for $d \approx 1$ μm, and the efficiency increases substantially when $d \lesssim$ 300 nm, suggesting that NFTPVs can achieve much higher efficiency compared to TPVs operating in the far-field. The absolute values of the efficiency of the current NFTPV systems are low (~0.02%) due to the small illuminated cell areas (~5% of cell surface, which diminishes

efficiency due to increased recombination), relatively low emitter temperatures, relatively low PV shunt resistance, and high energy absorption in the substrate. Our modeling (see section 4.5.10) indicates that efficiencies exceeding 6 percent can be achieved by heating the emitters to higher temperatures (~1000 K), fully illuminating the PV cell, and achieving better thermal heat sinking to maintain the cell temperature at moderate values (~25°C). Further improvements in efficiency, in the range 13 – 25%, can be accomplished by engineering selective emitters and using thin film PV cells with reflective back coatings[239, 240]. The experimental approaches developed here should enable systematic testing of all the above stated approaches.

4.4 Conclusion

This work overcomes past experimental challenges[68, 245] and demonstrates a large enhancement of the energy conversion rate in NFTPV devices as the gap size is systematically reduced. I reported a 40-fold enhancement in power output in NFTPV systems, in direct comparison to otherwise identical far-field TPV systems. Further, the comprehensive computational model of the NFTPV system highlighted how the efficiency of NFTPV systems can be improved in future experimental work. This work represents a critical first step towards the development of high-power, and eventually high-efficiency NFTPVs for waste heat recovery, and when combined with recent advances in nanostructured emitters[77] and materials[250] is expected to stimulate intense experimental work into NFTPV energy conversion that may be competitive with thermoelectric energy conversion.

4.5 Methods and Supporting Information

4.5.1 Parallelization of Emitter and Cell

I parallelize the emitter and PV cell in a two-stage process. In the first stage of parallelization, called "coarse parallelization," I use the nanopositioner in conjunction with a 50× objective (Zeiss LD EC Epiplan-Neofluar 50×/0.55 HD) with a shallow depth of field (2 μm). I first parallelize the PV cell to the imaging plane by using the nanopositioner to tip and tilt the cell until its entire surface (375 × 375 μm^2) comes into focus simultaneously. The resulting angular deviation of the cell, 2 μm over a 375 μm distance, is thus expected to be less than 5.3 mrad relative to the imaging plane, or a total height difference less than 425 nm across an 80 μm diameter region. Next, I parallelize the emitter chip (1 × 1 cm^2) to the imaging plane. I bring one region of the chip surface into focus before laterally translating to another region of the chip surface, ~8 mm away from the first position. I can then tip and tilt the emitter chip as needed until both positions are in focus simultaneously, and then iterate this process over another spot on the chip so that the entire chip is in focus everywhere. The resulting angular deviation of ~250 μrad (2 μm/8 mm) leads to less than 20 nm total height difference across the 80 μm mesa. This coarse parallelization thus should enable gaps as small as 450 nm, but additional alignment is required to achieve smaller gaps.

To further improve the parallelization of emitter and cell, I perform a second-stage "fine parallelization" step, based on the idea that the cell open circuit voltage, V_{oc}, always reaches a maximum immediately prior to contact, when the gap size reaches a minimum. While the TPV system is operating at 525 K and the current is fixed at 0, I continuously measure V_{oc} while reducing the gap between devices to contact. Because better alignment enables smaller gaps, a higher V_{oc} for a given tip/tilt of the emitter indicates improved alignment. By systematically

tipping and tilting the emitter to maximize V_{oc} prior to contact, the optimum alignment can be obtained. Emitter angle is adjusted by ~300 μrad per step during this process, so the final parallelism is expected to be within 150 μrad per rotation axis, indicating a 25 nm maximum possible deviation from parallelism (2 axes × 150 μrad × 80 μm).

4.5.2 Optical Detection of Mechanical Contact between Emitter and Cell

I use a laser deflection scheme to detect mechanical contact between the emitter and cell. The basic strategy, illustrated schematically in Fig. 4.2a, involves focusing a laser spot onto the backside of the emitter and focusing the reflected beam onto a segmented photodiode with two active areas. When the emitter displaces due to contact with the cell, this movement causes a change in the laser beam deflection that can be measured as a change in the output difference between the photodiode segments, as seen in Fig. 4.2c (middle panel). To further confirm that contact between emitter and cell has occurred, I modulate the cell position by ~5 nm peak-to-peak at 4 kHz and lock-in to the difference signal at 4 kHz via a lock-in amplifier (SRS 830, Stanford Research). When the two devices are not in contact, the emitter remains stationary and the 4 kHz component of the photodiode difference signal remains zero. When the devices make contact, the cell mechanically drives the emitter at 4 kHz and results in a sudden jump in the locked-in signal, as seen in Fig. 4.2c (lower panel). Importantly, the presence of the 635 nm radiation does not affect the PV response of the TPV cell. This fact was expected based on the cell's responsivity and was confirmed by enabling and disabling the laser and observing no change in the TPV output signal.

4.5.3 Fabrication of Suspended Emitter Microdevice

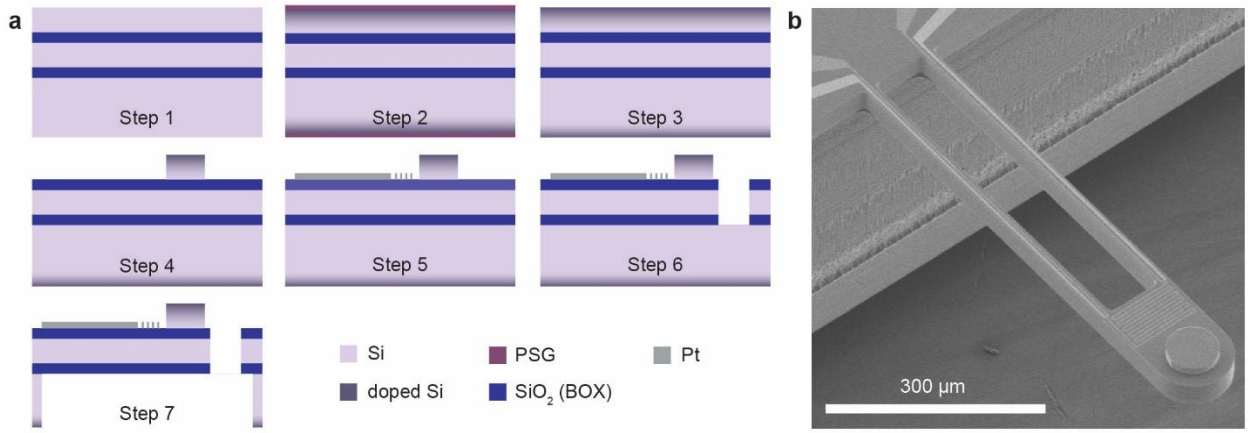

Figure 4.5: Fabrication of the emitter microdevice.
(a) Schematic of the seven-step emitter microdevice fabrication process. (b) Scanning electron micrograph of the fabricated structure.

A schematic diagram of the fabrication process for the emitter device is shown in Fig. 4.5a. The device is fabricated from a double-bonded silicon-on-insulator (SOI) wafer with a 500 µm-thick Si handle layer, a 40 µm-thick middle Si device layer, a 15 µm-thick top Si device layer, and two 1 µm-thick buried oxide (BOX) layers (Step 1). All Si layers are initially lightly doped. The top device layer is first doped to a level of 2.7×10^{20} cm^{-3} via phosphorous diffusion at 975 ºC for 12 minutes (Step 2). A phosphosilicate glass (PSG) layer that forms on the top device layer during the diffusion process is subsequently stripped using a buffered hydrofluoric (BHF) acid solution (Step 3). The top device layer is then etched until the upper BOX layer is revealed using reactive ion etching (RIE) to form a 15 µm-tall mesa (Step 4). Then, a 30 nm-thick Pt heater and 100 nm-thick Pt electrical leads are patterned onto the upper BOX layer using successive liftoff processes (Step 5). The structure of the device is formed by RIE etching through the upper BOX layer, the middle Si device layer, and the lower BOX layer using the same etch mask (Step 6). The Si handle layer is then etched from the backside via deep RIE

(DRIE) to suspend the device (Step 7). A scanning electron microscope (SEM) image of the fabricated device is shown in Fig. 4.5b.

4.5.4 Emitter Temperature Estimate

To model the power output of the NFTPV system, it is important to obtain an accurate estimate for the temperature of the suspended region of the emitter microdevice. Due to the large temperature rise on the suspended region of the emitter, and the fact that both the thermal conductivity of the Si beams[235] and the temperature coefficient of the electrical resistance of the thin-film Pt heater[236] are expected to change significantly as a function of emitter temperature, it was not possible to estimate the emitter temperature based on extrapolating thermal or electrical resistance values from room temperature properties. Instead, we estimated the emitter temperature T_E as a function of heat input Q_E by attaching a K-type thermocouple (Omega CHAL-002) to a representative emitter device using high-temperature epoxy (EPO-TEK 377).

Before the thermocouple is attached, the thermal conductance of the emitter suspension beams is characterized near room temperature in vacuum via a modulation scheme[217], as used previously[2] on comparable devices. In this scheme, I drive a sinusoidal current with amplitude I_f and frequency f through the Pt heater on the emitter. Heating at frequency $2f$ causes a sinusoidal heating Q_{2f} and temperature rise ΔT_{2f}, also at frequency $2f$. A voltage component $V_{3f} = \frac{I_f \alpha_0 \Delta T_{2f} R_0}{2}$ develops across the heater (where α_0 = 0.00197 K^{-1} is the Pt heater temperature coefficient of resistance and R_0 = 3526 Ω is the heater resistance at 300 K, as determined in separate characterization measurements), which can be used to estimate ΔT_{2f}. From knowledge of Q_{2f} and ΔT_{2f} the beam conductance G_{beam} can be computed according to the resistance network in Fig. 4.6a. I measured V_{3f} for a range of frequencies to ensure that our signal

was not attenuated due to the time response of our devices (Fig. 4.6d). With f = 1 Hz, we obtain G_{beam} = 241.67 ± 0.78 μW/K, where the uncertainty represents a 95% confidence interval on the data in Fig. 4.6e (red circles).

I then attached the K-type thermocouple (Omega CHAL-002) to a representative emitter device using a micropositioner stage to place the thermocouple, and high-temperature epoxy (EPO-TEK 377) to achieve strong thermal and mechanical contact. The attached thermocouple is shown in Fig. 4.6c. After the thermocouple was attached, I re-measured the conductance from the emitter island to the surroundings. Note that we expect the measured conductance to increase slightly due to the addition of a conduction pathway through the thermocouple (Fig. 4.6b). To measure the total conductance with the thermocouple attached, I followed the same procedure outlined in the previous paragraph, but because the emitter chip was heated to ~150° C during the epoxy cure, the Pt heater had annealed and it was necessary to again characterize α_1 = 0.00209 K^{-1} and R_1 = 3245 Ω. Furthermore, the added mass of the thermocouple and epoxy required a smaller value for f (Fig. 4.6d), so in this case f = 10 mHz was used. The total measured conductance measured with the thermocouple attached was found to be 247.35 ± 0.78 μW/K, shown in Fig. 4.6e as open blue circles. By computing the difference in conductance before and after attaching the thermocouple, I determined the added conductance due to the thermocouple, but one more measurement is required to quantify $G_{contact}$ and G_{leads} separately.

The last measurement necessary for characterizing $G_{contact}$ and G_{leads} was to record the thermocouple temperature T_{TC}. For this measurement, I used the Pt heater to sinusoidally heat the emitter with f = 10 mHz with the same amplitudes as the previous measurements, and measured the resulting amplitude of the temperature oscillations at the thermocouple junction.

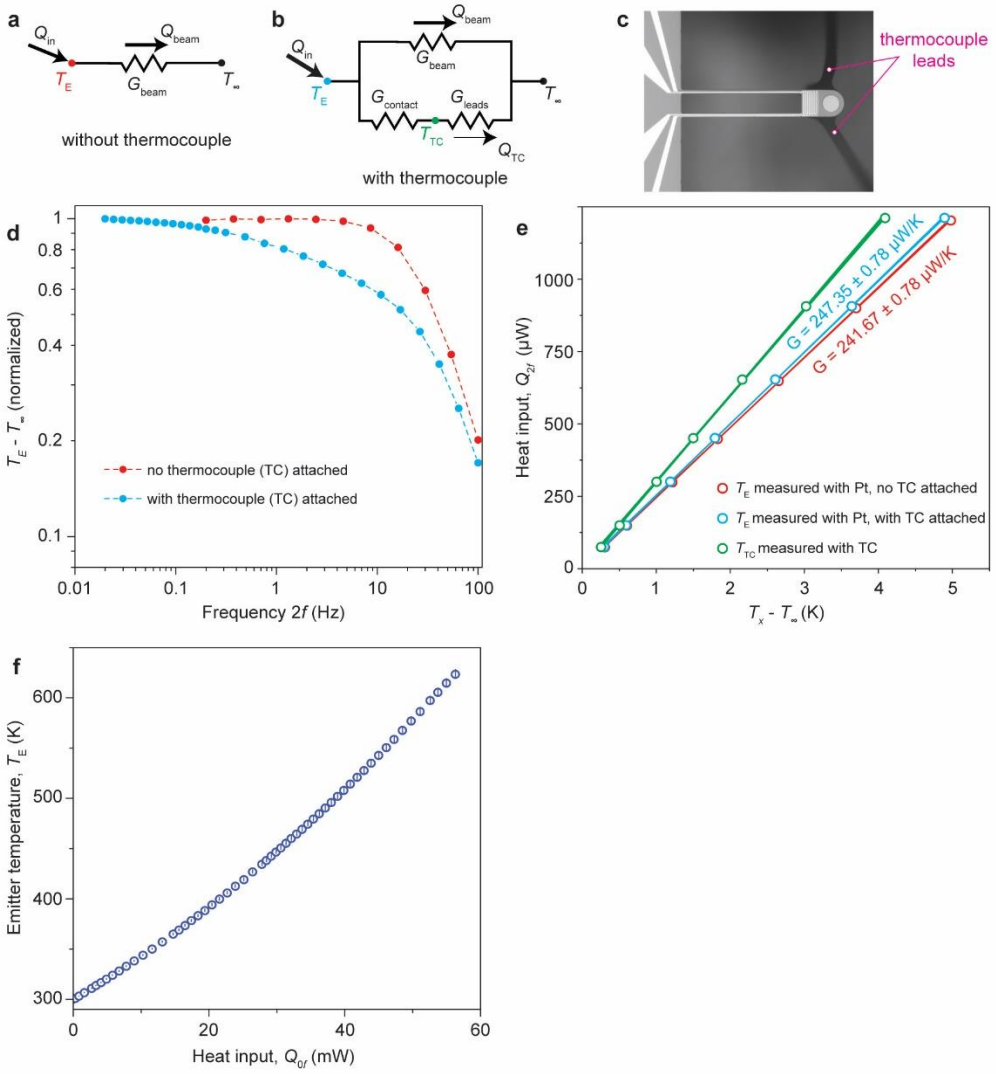

Figure 4.6: Emitter and cell temperature characterization.
(a) Thermal resistance network used to model the emitter when no thermocouple is attached. (b) Thermal resistance network used to model the emitter when a thermocouple is attached to the suspended region using epoxy. (c) Optical microscope image of the emitter with attached thermocouple. (d) Frequency response of the emitter device before and after attaching the thermocouple. (e) Modulated heat input vs. measured temperature oscillation amplitude. f, Estimated emitter temperature vs. dc heat input. (g) Measured cell effective resistance vs. cell temperature for representative cells.

The measured amplitudes $T_{TC} - T_\infty$ (T_∞ is the ambient temperature) are shown in Fig. 4.6e as green circles. Using the measured values for $T_{TC} - T_\infty$, $T_E - T_\infty$, and $\frac{1}{G_{contact}} + \frac{1}{G_{leads}}$ in the thermal resistance network in Fig. 4.6b, I estimate $G_{contact} = 35.79 \pm 2.39$ μW/K and $G_{leads} = 6.76 \pm 0.082$ μW/K near room temperature. Once G_{leads} was determined at room temperature, I estimated how

G_{leads} changes with temperature using temperature-dependent thermal conductivity values for chromel and alumel from the literature[251]. I assumed that $G_{contact}$ remains constant with temperature.

Finally, I heated the emitter to high temperature in vacuum and estimated T_E from the measured T_{TC} according to $T_E = T_{TC} + \frac{G_{leads}}{G_{contact}}(T_{TC} - T_\infty)$. The resulting estimated T_E is shown in Fig. 4.6f as a function of heat input Q_E, with error bars to indicate an uncertainty of ±2 K based on the 95% confidence in $G_{contact}$ and G_{leads}. Note that the device can be heated slightly higher than the range indicated in Fig. 4.6f, but those temperatures were not accessible in my test device because they lie outside the operating range of the epoxy. Because the curve is well-behaved, I fit an exponential to the data and extrapolate to estimate T_E over the full temperature range. I post-processed our data to estimate how G_{beam} is expected to depend on T_E in the emitter device in the absence of the thermocouple, and assumed that G_{beam} in the NFTPV emitter device followed a similar trend. Because there is some variation in the device geometry/properties, I expect that this last assumption expands the uncertainty bounds from ±2 K to ±5 K.

4.5.5 Sample Surface Preparation and Characterization

Particles and/or roughness of the active areas directly limit the minimum vacuum gap size in any near-field measurement between parallel plates. It is therefore imperative to obtain extremely clean and flat surfaces. Because the suspended emitter structure is mechanically more fragile than the cells, separate cleaning procedures were developed for the emitter device as opposed to the cells.

The as-fabricated mesa surface is extremely flat and smooth, with negligible roughness (<1 nm RMS), which is expected because this surface initially was the surface of a pristine wafer (see section 1 for fabrication details). However, contamination by particles of up to several μm in size is introduced during doping and/or during the other fabrication steps. To remove these particles, we use a process developed by us. The emitter chips are pretreated with acetone before being immersed in a hot solvent stripper (Remover PG). The chips are then rinsed with isopropyl alcohol and submerged in piranha solution. As a finishing step, the chips are baked on a hot plate at 120° C. This process succeeds in removing the largest particles but some smaller particles remain, as confirmed by atomic force microscopy (Fig. 4.7a). These particles, which can be up to ~55 nm tall, directly limit the minimum gap size in the TPV measurement.

The PV cells are mechanically more robust than the emitter, allowing for a more aggressive cleaning process. We clean the 0.345 eV cells in a Trilennium wafer and mask cleaner (Solid State Equipment Corporation) by spraying ammonium hydroxide, scrubbing via a rotary polyvinyl alcohol brush, and following up with ultrasonic cleaning. This process removes virtually all particles from the surface, as confirmed by atomic force microscopy (Fig. 4.7b). In addition to being very clean, the 0.345 eV cells display only a few nm roughness over a large (50 μm × 50 μm) area. Therefore, the surface topography of the 0.345 eV cell is not expected to limit the minimum gap size or maximum extracted power in our TPV system. The 0.303 eV cell is cleaned in the same way and is likewise found to be free from particles (Fig. 4.7c). However, this cell displays a latticework-like roughness (presumably resulting from processing during manufacturing of the cell) with peak-to-peak height of 53 nm that effectively adds 20 nm to the minimum achievable gap size, as determined using the proximity approximation. Therefore I shift the data for the 0.303 eV diode by 75 nm.

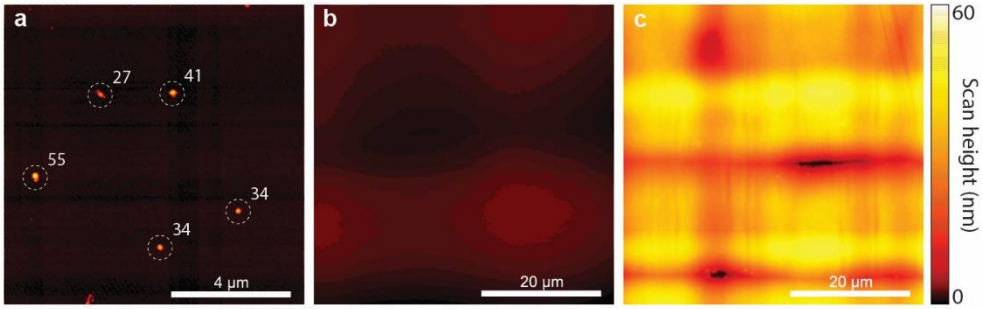

Figure 4.7: Microdevice surface characterization.
(a), Atomic force microscope (AFM) image of a 10 µm × 10 µm area of the emitter mesa. The as-fabricated mesa is extremely flat but does have particles reaching 55 nm in height. The number next to each particle indicates the height of that particle in nm. (b), AFM image of a 50 µm × 50 µm area of the 0.345 eV cell. No particles and <5 nm deviation from flatness is observed. (c), AFM image of a 50 µm × 50 µm area of the 0.303 eV cell, showing a latticework roughness pattern with height of 53 nm peak-to-peak. For ease of comparison between samples, all three panels share the same color bar.

4.5.6 Control Experiments to Demonstrate that the Observed Effects are Due to Photovoltaic Response and Not Thermoelectric Response

One may suspect that the emitter in our system induces a temperature gradient across the p-n junction of the cell, generating current via the thermoelectric rather than photovoltaic effect, so it is important to determine the extent to which thermoelectric effects could contribute to our measured power output. To delineate between these effects I first note that temperature gradients in the PV cell, if any, should be largest when the emitter and the PV cells are in contact with each other. This is because the flow of heat from the emitter to the receiver due to thermal conduction (for devices in contact) is many orders of magnitude greater than heat flow due to radiation across a finite gap. Therefore, I expect any thermoelectric response to be greatest when the two devices are physically touching, which would also imply that the power output (P_{MPP}) from the TPV cell should also increase dramatically when the emitter and PV cell touch each

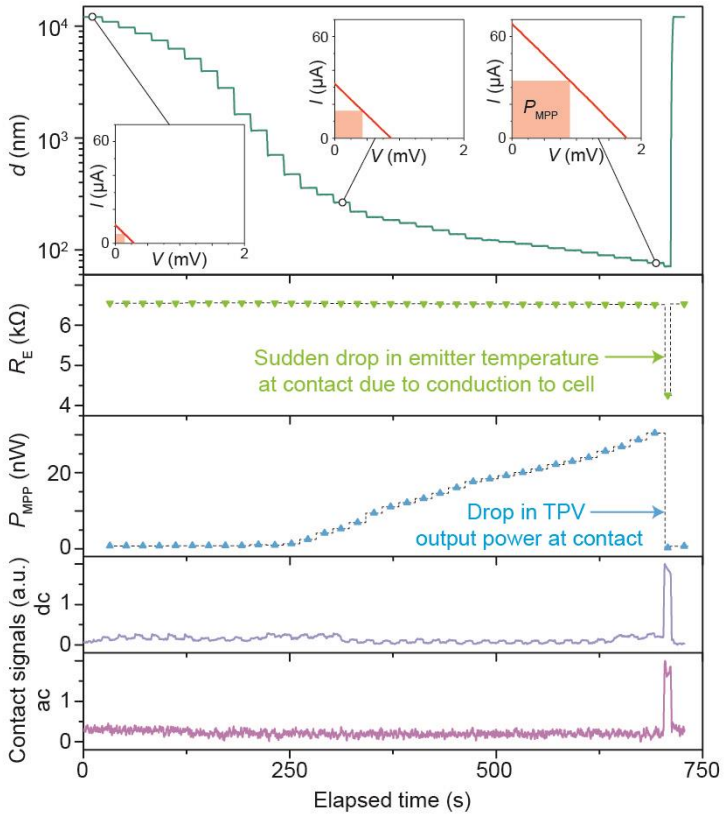

Figure 4.8: Investigation of influence of thermoelectric effect on cell performance.
The top panel and bottom two panels show the evolution of the gap size and optical contact signals over the course of an experiment and are the same as in Fig. 4.2c. The second panel from the top shows the emitter resistance, which is an indicator of emitter temperature, suddenly decreasing when contact is made indicating an increased flow of heat from the emitter to the cell after contact. The third panel shows a sharp decrease in the generated electric power that occurs at precisely the same time, indicating little or no thermoelectric response.

other if the thermoelectric contribution has significant contributions. In order to test for this possibility, I measured the cell's electrical response while the emitter and cell were brought into physical contact with each other. This process is shown in Fig. 4.8. As the gap size d is reduced, the electrical resistance R_E of the emitter heater remains nearly constant, while the cell power output at the maximum power point, P_{MPP} increases. Once the devices reach contact, as indicated by the ac and dc optical signals, R_E suddenly decreases reflecting a temperature drop of the emitter due to heat flow from the emitter to PV cell via conduction. However, contrary to the expectation of increased power output for a thermoelectric response, I find that the power output

becomes negligibly small, clearly demonstrating that that thermoelectric response is insignificant.

4.5.7 Analysis of Enhancement in Power Output Due to Increases in View Factor upon Decreasing Gap Size

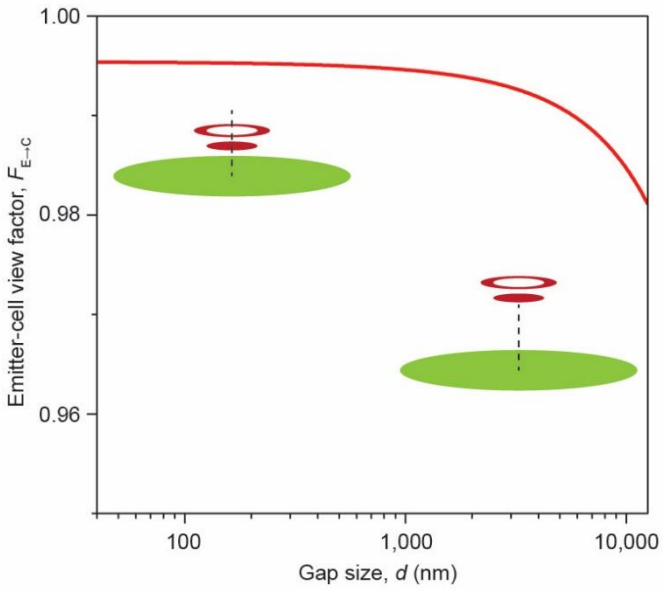

Figure 4.9: Calculation of view factor from emitter to cell.
Approximate view factor $F_{E\rightarrow C}$ from emitter to cell. The view factor is seen to change very little over the gap size range relevant to this work. Inset: Schematic illustration of the approximated geometry (not drawn to scale).

As described in the manuscript, the power output of the PV cell increases as the gap size between the emitter and the PV cell is reduced. This increase has small contributions from changes in the view factor $F_{E\rightarrow C}$ (i.e., the fraction of the radiation leaving the emitter surface that is intercepted by the cell)[252]. To determine to what extent $F_{E\rightarrow C}$ enhanced power output, I computed the view factor $F_{E\rightarrow C}$ from the emitter to the PV cell for various gap sizes (Fig. 4.9). I approximated the system using coaxial parallel disks, for which a simple analytical expression for the view factor exists[252]. The emitter is modeled as an 80 μm-diameter disk situated 12 μm below a 120 μm outer diameter, 80 μm inner diameter annulus (this larger annulus accounts for

the remaining portion of the heated emitter). The cell is approximated as a disk with 375 μm diameter. When varying the distance between emitter and cell from 12.5 μm to 60 nm, the computed view factor $F_{E\rightarrow C}$ is expected to increase from 98.75% to 99.74%. This ~1% increase in the view factor could be expected to lead to an enhancement in I_{sc} of ~1%, and an increase in P_{MPP} of ~2%. Compared to the ~3900% increase due to the near-field enhancement, the expected increase due to changing view factor is negligibly small.

To gain insight into the TPV system's performance, we developed a computational model of the system. In the model we first compute the spectral radiative energy transfer from the emitter to the cell. Next, we use knowledge of the spectral energy transfer to calculate the cell's *I-V* response. Below, we begin by describing our approach to modeling the spectral energy transfer.

4.5.8 Radiative Energy Transfer Modeling

The geometry of the PV cells employed in this work is shown in Fig. 4.10. Both PV cells are based on a double-heterostructure architecture, consisting of an active layer (undoped or lightly doped) sandwiched between a wide bandgap cladding layer and an n-type InAs substrate. The back side of the substrate is vacuum deposited with a Cr/Au/Ni/Au (10/30/50/100 nm) multilayer system to form an ohmic contact. In the electromagnetic modeling, the back-side electrode is treated as being infinitely thick Au. The bandgap energy E_g and the thickness for each individual layer are illustrated in Fig. 4.10 for both PV cells, and were obtained from the data shown in Ref. [253] by the manufacturer. We name each cell by the bandgap of its active layer. For the 0.345 eV cell, the active layer is very nearly pure InAs, and the cladding layer is $InAs_{1-x-y}Sb_xP_y$ where x and y are nominally 0.25 and 0.5, respectively. For the 0.303 eV cell, the active

layer is $InAs_{0.9}Sb_{0.1}$ and the cladding layer is $InAs_{0.51}Sb_{0.21}P_{0.28}$. The substrate for both PV cells is n-type InAs with a sulfur doping concentration of 2×10^{18} cm^{-3}, and we have accounted for the Moss-Burstein effect in the substrate layer in which the effective optical bandgap of a semiconductor which has a small electron effective mass shows blue shift at a large electron doping[254].

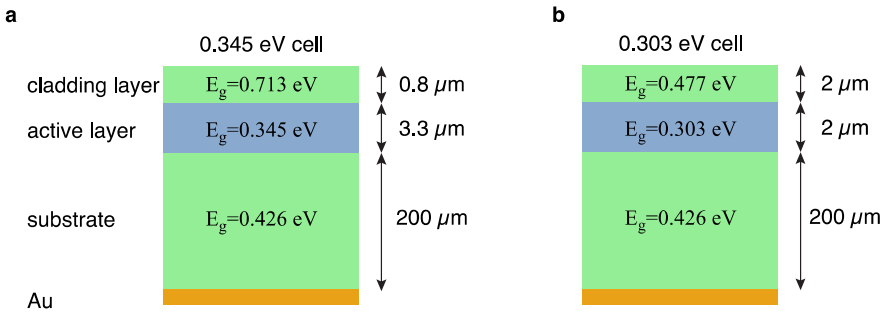

Figure 4.10: Geometry for the PV cells.
(a), Modeled geometry for the 0.345 eV bandgap cell, with parameters including the bandgap energy E_g and thickness for each layer. (b), Same as (a), but for the 0.303 eV bandgap cell.

To model radiative heat transfer we require the optical properties for every layer, but the dielectric properties of the specific semiconductor layers that comprise of our device are largely unavailable from literature. However, because each layer in the cell is primarily composed of InAs, the shape of the permittivity spectrum near bandgap is expected to be very similar to that of InAs[255]. Therefore, we can use the energy-shift model developed elsewhere[255], which allows for relatively accurate modeling of the above-bandgap permittivity for III-V semiconductor alloys by simply introducing an energy shift to the permittivity spectrum of undoped InAs.

To elaborate, the energy-shift model assumes that at frequencies above the bandgap, the dielectric function for a InAs-rich semiconductor alloy is obtained by shifting the above-bandgap permittivity of InAs by an energy shift ($E_{g,Alloy} - E_{g,InAs}$). At frequencies below the bandgap, the permittivity is taken from the data for InAs. We also account for the free-carrier absorption due

to doping by incorporating a Drude term at all frequencies. Therefore, for an InAs-rich semiconductor alloy of bandgap frequency ω_{g}, we have

$$\varepsilon_{\mathrm{Alloy}}(\omega)=\varepsilon_{\mathrm{InAs}}(\omega-\omega_{\mathrm{g}}+\omega_{\mathrm{g,\,InAs}})+\varepsilon_{\mathrm{Drude}}(\omega)\text{ , when }\omega>\omega_{\mathrm{g}} \tag{4.3}$$

and

$$\varepsilon_{\mathrm{Alloy}}(\omega)=\varepsilon_{\mathrm{InAs}}(\omega)+\varepsilon_{\mathrm{Drude}}(\omega)\text{ , when }\omega<\omega_{\mathrm{g}} \tag{4.4}$$

where

$$\varepsilon_{\mathrm{Drude}}=-\frac{N_{\mathrm{e}}e^2}{\varepsilon_0 m_{\mathrm{e}}^*}\frac{1}{\omega^2-i\omega\Gamma_{\mathrm{e}}}-\frac{N_{\mathrm{h}}e^2}{\varepsilon_0 m_{\mathrm{h}}^*}\frac{1}{\omega^2-i\omega\Gamma_{\mathrm{h}}}. \tag{4.5}$$

Here, the electron concentration is given by $N_e=\frac{1}{2}\sqrt{N_{\mathrm{D}}-N_A+\sqrt{\left(N_D-N_A\right)^2+4n_i^2}}$, the hole concentration is given by $N_{\mathrm{h}}=\frac{1}{2}\sqrt{N_A-N_{\mathrm{D}}+\sqrt{\left(N_A-N_D\right)^2+4n_{\mathrm{i}}^2}}$, N_{D} is the n-doping concentration, N_{A} is the p-doping concentration, and the intrinsic carrier concentration n_{i} is obtained from the intrinsic carrier concentration of InAs at room temperature,

$$n_{\mathrm{i}}=10^{15}\,\mathrm{cm}^{-3}\times e^{\left[-\frac{E_{\mathrm{g}}}{2k_{\mathrm{B}}T}+\frac{E_{\mathrm{g,\,InAs}}}{2k_{\mathrm{B}}\cdot 300\,\mathrm{K}}\right]}. \tag{4.6}$$

For the electron and hole effective mass m_e^* and m_h^*, we take the values for InAs (i.e., $m_e^*=0.023\,m_e$, and $m_h^*=0.41\,m_e$). The electron and hole scattering rates $\Gamma_{\mathrm{e}}=\frac{e}{m_{\mathrm{e}}^*\mu_{\mathrm{e}}}$ and $\Gamma_{\mathrm{h}}=\frac{e}{m_{\mathrm{h}}^*\mu_{\mathrm{h}}}$, respectively, where the electron and hole mobilities are $\mu_{\mathrm{e}}=4\times10^4\,\frac{\mathrm{cm}^2}{\mathrm{V\cdot s}}$ and $\mu_{\mathrm{h}}=500\,\frac{\mathrm{cm}^2}{\mathrm{V\cdot s}}$, respectively. The effective mass and carrier mobility are obtained from Ref. [256]. Finally, the permittivity for gold is obtained from Ref.[216].

We now turn to the modeling of the emitter. The circular mesa structure is modeled according to the geometry shown in Fig. 4.11a. It consists of a 430 nm thick layer of n-doped Si with a doping concentration of 2.7×10^{20} cm^{-3}, a 14.57 μm thick layer of undoped Si, a 1 μm thick layer of silicon dioxide and a 40 μm thick layer of undoped Si. During the experiment, the emitter is heated to temperatures as high as 655 K, so temperature-dependent permittivity is used to model both the heavily-doped Si and the intrinsic silicon[233, 257]. The optical properties of the silica layer are not expected to deviate significantly in the temperature range of interest (525 K - 655 K), so we model them using tabulated permittivity at room temperature[216].

Our approach for calculating radiative heat transfer uses fluctuational electrodynamics and is based on a scattering matrix formalism. We treat both the emitter and the PV cells as multilayer structures. In the calculation, correlations in fluctuating currents are determined using the fluctuation dissipation theorem. Then we use a numerically-stable scattering matrix (S-matrix) formalism[258] to solve the electromagnetic fields resulting from these fluctuating currents. Such an approach for computing electromagnetic heat transfer has been used in the past, for example in Refs. [248, 259]. Using this approach we can obtain the absorbed power in any individual layer due to the presence of fluctuating current sources in any other layer.

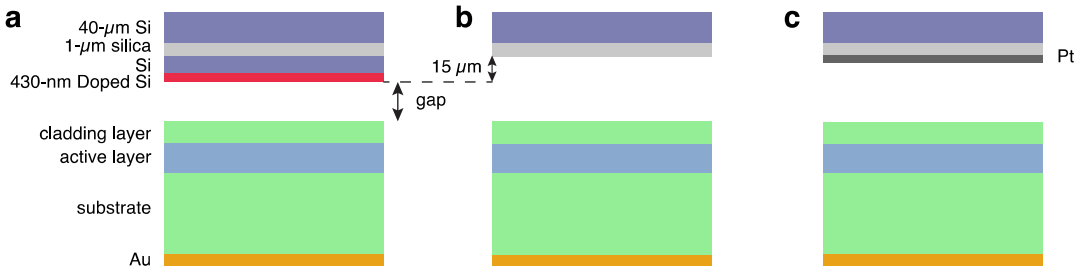

Figure 4.11: Geometry for radiative heat transfer.
(a), Schematic of geometry for mesa, and PV cells. (b), Schematic of geometry for silica covered portion of the suspended island region, and PV cells. (c), Schematic of geometry for Pt-covered portion of the suspended island region, and PV cells.

As described later, our modeling of power output from the PV cell requires us to compute the radiative heat transfer from every emitter layer to the active layer of the PV cell. For the radiative heat transfer between multilayer structures considered here, we can calculate the transmission probability from the emitter to the active layer (p-n junction) for both transverse-electric (TE) and transverse-magnetic (TM) modes, i.e. $\tau_{\mathrm{TE,\,E\to J}}(\omega,k)$ and $\tau_{\mathrm{TM,\,E\to J}}(\omega,k)$ where k denotes the parallel wave-vector. The value for these two transmission probabilities is between 0 and 1. To simplify notation, we introduce the dimensionless transfer function

$$\phi_{\mathrm{E}\to J}=\left(\frac{\lambda}{2\pi}\right)^2\int_0^\infty kdk\left[\tau_{\mathrm{TE,\,E\to J}}(\omega,k)+\tau_{\mathrm{TM,\,E\to J}}(\omega,k)\right], \tag{4.7}$$

where the subscripts E and J denote the emitter and the junction, respectively. To better understand this term, it is worth noting that between two blackbodies in the far field, this transfer function equals unity. In the near-field, due to surface waves or the evanescent fields of waves that undergo frustrated total internal reflection, this transfer function f may exceed unity. Similarly, we denote the transfer function from the ambient to the active layer of the PV cell as $\phi_{\mathrm{amb}\to\mathrm{J}}$.

To assess the energy conversion efficiency, which we define as the ratio of the maximal power generation divided by the total heat transfer from the emitter to the PV cell, we also need to calculate the total energy transfer from all emitter layers to all cell layers. We denote the transfer function between the emitter and the whole PV cell as $\phi_{\mathrm{E}\to\mathrm{cell}}$. This calculation is performed in wavelengths ranging from far infrared to 1 μm.

Finally, since the size of the PV cell is larger than the size of the emitter mesa, we must account for radiation from the other regions of the emitter besides the mesa. Towards this goal,

we modeled these regions as multilayer structures. Figure 4.11b shows the scenario of transfer between the rest of the emitter island and the PV cell. We denote the non-mesa area of the suspended region as A_{susp}. Because a portion of the suspended region is covered in the Pt heater, we also consider the contribution from this region, denoted A_{Pt} and illustrated schematically in Figure 4.11c. Further, we denote the transfer function between these regions to the active layer of the PV cell as $\phi_{\text{susp}\to\text{J}}$ and $\phi_{\text{Pt}\to\text{J}}$, and the transfer function between these regions to the whole PV cell as $\phi_{\text{susp}\to\text{cell}}$ and $\phi_{\text{Pt}\to\text{cell}}$. The transfer functions per unit area of mesa can thus be expressed as:

$$\phi_{\text{E}\to J} = \frac{\phi_{\text{mesa}\to\text{J}} A_{\text{mesa}} + (\phi_{\text{susp}\to\text{J}} A_{\text{susp}} + \phi_{\text{Pt}\to J} A_{\text{Pt}}) \cdot f}{A_{\text{mesa}}} \tag{4.8}$$

$$\phi_{\text{E}\to\text{cell}} = \frac{\phi_{\text{mesa}\to\text{cell}} A_{\text{mesa}} + (\phi_{\text{susp}\to\text{cell}} A_{\text{susp}} + \phi_{\text{Pt}\to\text{cell}} A_{\text{Pt}}) \cdot f}{A_{\text{mesa}}} \tag{4.9}$$

where the subscript *mesa* denotes mesa region, and *f* is the view factor from the rest of the suspended region to the cell. Because the emitter mesa is positioned near the center of the PV cell, the rest of the suspended region is positioned almost directly above the top electrode of the cell. Therefore, the view factor *f* from the non-mesa portion of the emitter island to the PV cell can actually be quite small. Based on fitting our data in the far field, we estimate that *f* ~0.1-0.25 in which the variation may come from the slightly different relative positioning of the emitter to the cell in each experiment.

4.5.9 PV cell I-V Response Modeling

In this section, we discuss our approach to modeling the *I-V* response of the PV cells. In Fig. 4.12, we provide an equivalent circuit for the PV cell where the polarity for the current is defined such that both *V* and *I* are positive when the cell generates electricity. For our system, the

parasitic series resistance is small (R_s < 1.5 Ω) and can be neglected in our calculation (i.e., R_s ~ 0), so we can simplify the circuit such that $V_d = V$. The 0.345 eV bandgap cell develops a shunt resistance R_{sh} = 32 Ω when located in our vacuum system. Similarly, for the 0.303 eV bandgap cell, R_{sh} = 19 Ω in our vacuum system.

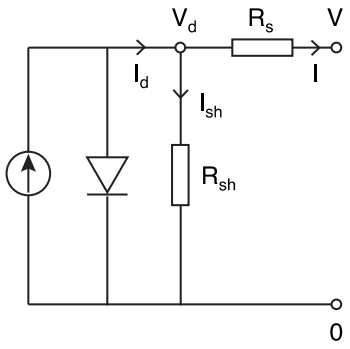

Figure 4.12: Equivalent circuit of the photovoltaic (PV) cell.
Schematic illustration of the equivalent circuit used to model the PV response of our cells.

The current generated in the diode has contributions from both radiative and non-radiative recombination processes. The net current generated by the radiative process (I_{rad}) is:

$$I_{rad}(V) = A_{mesa} e \int_{\omega_g}^{\infty} d\omega \frac{1}{\lambda^2} \left[\phi_{E\to J} \left(\frac{1}{e^{\frac{\hbar\omega}{k_B T_E}} - 1} - \frac{1}{e^{\frac{\hbar\omega - qV}{k_B T_J}} - 1} \right) + \phi_{A\to J} \left(\frac{1}{e^{\frac{\hbar\omega}{k_B T_A}} - 1} - \frac{1}{e^{\frac{\hbar\omega - qV}{k_B T_J}} - 1} \right) \right], \qquad (4.10)$$

where e is the elementary charge, T_J is the temperature of the cell including the junction, T_E is the temperature of the emitter, and T_A is the temperature of the ambient. We assume that each absorbed above-bandgap photon in the active layer generates an electron-hole pair. We note that in deriving Eqn. 3.10, we have used the reciprocal relation for transfer functions, i.e. $\phi_{1\to 2} = \phi_{2\to 1}$.

Several non-radiative processes also play important roles in determining the net current, including Auger recombination and Shockley-Read-Hall (SRH) processes. The net recombination current associated with Auger recombination (I_{Auger}) is given by:

$$I_{\text{Auger}}(V) = A_{\text{J}} C_0 n_{\text{i}}^3 \left[e^{\frac{3qV}{2k_{\text{B}}T_{\text{J}}}} - e^{\frac{qV}{2k_{\text{B}}T_{\text{J}}}} \right] t_{\text{J}}, \tag{4.11}$$

where C_0 is the combined Auger recombination coefficient, n_{i} is the intrinsic carrier concentration, and t_{J} and A_{J} are the thickness and area of the active layer of the PV cell, respectively. As the junction is made of InAs-rich semiconductor alloy, we use the combined Auger recombination coefficient for InAs[260], with $C_0 = 2.2 \times 10^{-27}\,\text{cm}^6/\text{s}$.

The net recombination current associated with SRH process (I_{SRH}) is given by:

$$I_{SRH}(V) = A_{\text{J}} S n_{\text{i}} \left[e^{\frac{qV}{2k_{\text{B}}T_{\text{J}}}} - 1 \right], \tag{4.12}$$

where S is the surface recombination velocity including the effects from both interfaces of the active layer. By combining the effects of radiative and non-radiative recombination in addition to the current flowing $I_{sh}(V) = V / R_{sh}$ through the shunt resistance (R_{sh}), the total current in the device (I) is given by:

$$I(V) = I_{\text{rad}}(V) - I_{\text{Auger}}(V) - I_{\text{SRH}}(V) - I_{sh}(V). \tag{4.13}$$

Equation 3.13 is the master equation we use to model the *I-V* response of the PV cell. Here, the radiative transfer functions in Eqn. 3.10 is calculated from fluctuational electrodynamics. The surface recombination velocity S is obtained from fitting the experimental data, such that the slope of *I-V* curve at small current determined by Eqn. 3.12 matches the experimentally measured slope of *I-V* curve.

4.5.10 Prediction of Performance for Improved Conditions

To show the potential for improved efficiency from future device designs, I use our numerical model to predict the performance of the 0.345 eV cell under more favorable operating conditions. Specifically, I consider the case for which emitter temperature T_E = 1000 K, the cell temperature T_C = 300 K, the emitter area is perfectly matched to the cell area (100% illumination area), and the diode's resistance is maintained at a high value (i.e. by avoiding deterioration of performance in vacuum) which might be achieved by surface passivation and report the efficiency as a function of gap size in Fig. 4.13. I predict that a device operating under these conditions would achieve efficiencies of 3% in the far-field, and efficiencies above 6% could be achieved by decreasing the gap size to less than 100 nm. Theoretical work performed by others[240] suggests that designing thin-film emitters and cells can yield further gains, enabling efficiencies above 30%. The experimental techniques established in this work will enable systematically testing all these possibilities.

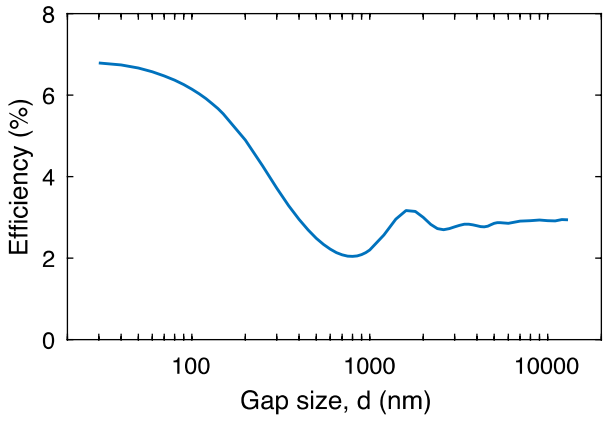

Figure 4.13: Predicted efficiency dependence on gap size for the 0.345 eV cell.
Here, the emitter is assumed to be at 1000 K and have the same area as the PV cell, and the PV cell is assumed to be maintained at 300 K.

4.5.11 Transmission Probability between Mesa and 0.345 eV Bandgap Active Layer

To better understand the contributing modes for the near-field enhancement, we compute the transmission probabilities between the active layer of the 0.345 eV bandgap cell and the mesa at 655 K, at above-bandgap energies, for gaps of 12000 nm, 215 nm, and 60 nm. In Fig. 4.14a-c, we show the transmission probability which is the sum of contributions from TE and TM modes as a function of parallel wavevector k and photon energy $\hbar\omega$. We use a green line to denote the light line, i.e. $\omega = ck$. Modes that are situated on the left of the light line are propagating in the free space. We also use a blue line to denotes $\omega = ck/3.5$, where 3.5 is approximately the refractive index of the cladding layer used in the model. Modes situated between the green line and the blue line are evanescent in free space, but propagating in the cladding layer. These modes are also known as total internal reflection modes.

Figure 4.14a shows that for a large gap of 12 μm, transmission only exists for modes that are propagating in the free space. In this case, the energy transfer will be limited by the far field blackbody limit. In contrast, as the gap reduces, modes that are evanescent in the free space begin to contribute. For example, Fig. 4.14b shows that at 215 nm gap, transmission probability between the light line and $\omega = ck/3.5$ becomes significant. As the gap further reduces to 60 nm, we observe that the transmission probability further increases. Therefore, in this study, the near-field enhancement is due to the frustrated total internal reflection which can tunnel through a vacuum gap when the gap is much smaller than the relevant wavelengths.

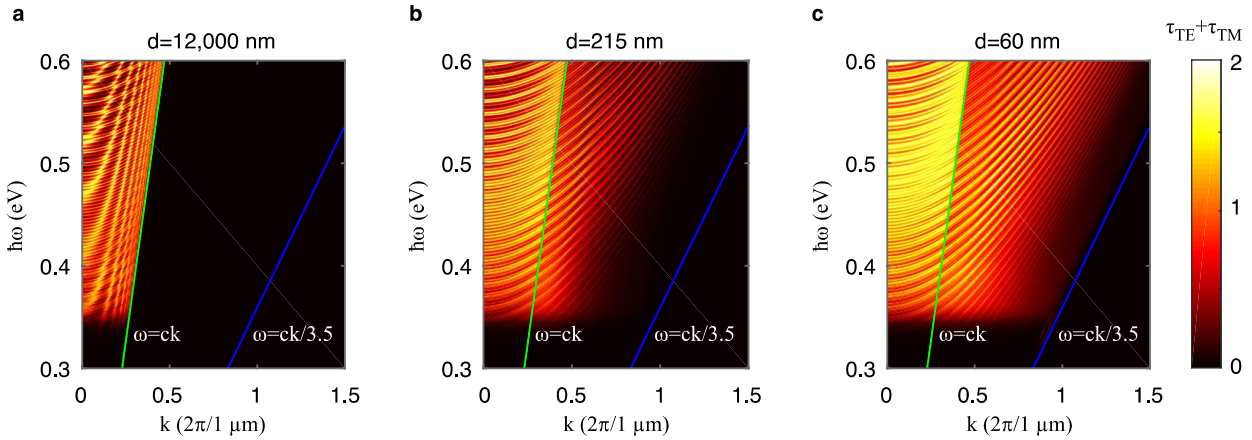

Figure 4.14: Modeled transmission probability between the active layer of a 0.345 eV bandgap cell and an emitter mesa at 655 K.
Transmission probability as a function of parallel wavenumber k and photon energy $\hbar\omega$, at a gap of (a) 12000 nm, (b) 215 nm, and (c) 60 nm. For a, b, and c, the probability includes the contributions from transmission through both TE and TM modes. We also show the light line in vacuum i.e. $\omega = ck$ as a green line, and delimits the guided modes in the cladding layer using the blue line which is described as $\omega = ck/3.5$.

3.6 Author Contributions

Pramod Reddy and Edgar Meyhofer conceived and supervised the work. I and Linxiao Zhu performed the experiments. Linxiao Zhu and I performed the calculations. Dakotah Thompson and Rohith Mittapally fabricated the emitter devices.

Chapter 5: Summary and Outlook

5.1 Summary

In this dissertation I presented a modified method for measuring near-field radiation between parallel planar surfaces which improved on past methods in a few key ways. Namely, in contrast to previous methods[2] which I helped develop, and which employed one microdevice heater and another microdevice thermometer to perform calorimetry, here I heated and performed calorimetry in a single emitter microdevice. This change dramatically expands the variety of samples which could be employed as a receiver device, making our setup suitable for exploring a number of applications which were not possible using our previous approach. Furthermore, this change in approach enables smaller vacuum gaps between emitter and receiver to be obtained, as I demonstrated in a proof-of-principle experiment. In that experiment, I measured NFRHT between an SiO_2-covered microdevice and a macroscopic SiO_2-coated chip using this new technique, and I measured a 1,200-fold enhancement in the radiative heat flux by closing the gap between emitter and receiver from ~8 μm to as small as 25 nm, in good agreement with theory. This represented a heat flow enhancement ~700 times larger than the blackbody limit.

Next, I utilized a similar approach to demonstrate, to my knowledge, the first near-field radiative thermal diode. The diode was composed of a doped Si surface and a VO_2 film separated by a vacuum gap, and I was able to electrically heat either surface and make calorimetric measurements with the Si microdevice. Because the optical properties of VO_2 dramatically

change when it undergoes a metal-insulator-transition at 68° C, a rectification coefficient larger than 50% was achieved at gap sizes of ~150 nm and temperature differences of ~70 K by operating around this transition temperature. A mathematical model was developed and was used to find an optimum in the layer thickness, indicating that slightly better rectification can be achieved by reducing the VO_2 film thickness to 200 nm.

Finally, I adapted the same system to demonstrate, for the first time, enhanced thermophotovoltaic power generation in the near-field. I electrically heated a custom-fabricated Si microdevice emitter to as high as 655 K and positioned it across a vacuum gap from a commercially-available InAs-based photovoltaic cell. Power output enhancements of approximately 40-fold were obtained by reducing the vacuum gap from ~12 μm to ~60 nm. Cells with two different bandgap energies were used and their performance was compared. A comprehensive computational model was presented and used to identify the most promising paths for further development.

5.2 Outlook

In this section I lay out a plan for what I believe are the important steps that experimentalists in this field must take over the next several years. I also provide a longer-term view of where and how I envision near-field thermophotovoltaics fitting into our future energy portfolio.

Near-Field Radiative Heat Transfer Measurements between Parallel Plates

Future measurements of near-field radiative heat transfer between parallel plates should focus on demonstrating some of the more “exotic” predictions made by theorists, specifically with regard to the ability to dynamically tune NFRHT with 2D materials such as graphene, the

ability to enhance NFRHT between dissimilar materials by employing nanostructured surfaces, and the ability to achieve particular spectral characteristics by creating custom-fabricated metamaterials. Ample evidence now exists supporting the theoretical basis for NFRHT, with our results showing very good agreement with theory from ~10 μm to ~25 nm for SiO_2 plates, so future studies should be carried out with a keen eye towards particular applications. For example, the development of metamaterials is perhaps best-served by aiming to demonstrate a material with a sharp plasmon resonance at relatively low energies (0.5 eV), for use in near-field thermophotovoltaics.

There are also a number of ways to improve upon the methodology described in this dissertation. Specifically, developing a more compact and easy-to-use nanopositioning system, with a greater degree of feedback to the user, will dramatically simplify the process for data acquisition and lead to more productive research. Furthermore, an interferometry-based gap size measurement would be extremely beneficial for objectively determining gap size between the planar surfaces, which would be especially useful, for example, in comparing the heat flow rates for different samples at a given gap size.

Near-Field Thermophotovoltaics

I do not believe that near-field thermophotovoltaics will ever replace large-scale, fixed electrical power generators like solar photovoltaic arrays or natural gas-fired power plants. For high temperature differences from steady heat sources, it is unlikely that NFTPV will ever achieve efficiencies that would justify a re-investment in base load power production. But to compare NFTPV to a natural gas-fired plant is to misunderstand what makes NFTPV unique. Specifically, NFTPV devices are quiet, have no moving parts, and can in principle be scaled to

be portable and/or fixed directly to other machinery. These advantages make NFTPVs more comparable to thermoelectric generators (TEGs). And while today's TEGs are *fundamentally* limited[261] (by the figure of merit, *ZT*) to ~14% efficiency for T_H = 1000 K and T_L = 300 K, the theoretical upper limit for NFTPV devices can be much higher. In fact, for the same T_H and T_L, Zhao *et al.*[243] propose a NFTPV system for which they predict 25% efficiency can be obtained.

I therefore believe that NFTPV can carve out a niche in our energy portfolio as a waste heat salvager in industrial and/or automotive applications. Consider, for example, the fact that exhaust gas in an internal combustion engine, like the ones used in personal automobiles, can reach ~1000 K out of the cylinder head, and catalytic converters typically operate in the range 700 – 1000 K. Fixing NFTPVs to these hot spots in our personal vehicles could generate electricity to power the on-board electronics, leading to better fuel economy. Also consider that many industrial processes generate waste heat ripe for energy salvaging, but the temperatures involved are often too low (800 – 1100 K) and not steady enough (intermittent heating) for a traditional steam turbine. These processes include glass-making furnaces, steel production, natural gas flaring, petrochemical cracking, and others. The scalable and portable nature of NFTPVs, and their suitability for low-temperature and intermittent sources, make them promising for these types of applications. However, there remains a number of developments that are required before the technology can become useful.

In the short term, it is necessary to demonstrate an improved NFTPV prototype. Our NFTPV prototypes succeeded in demonstrating an approximately 40-fold increase in electrical power output in the near-field relative to the far-field, and that demonstration was critical for showing the potential of near-field operation in TPVs. But the efficiency of our prototypes, which are estimated to be less than 0.015% based on our modeling, must be improved before

NFTPVs can be adopted. There are a few straightforward improvements that can be made in this regard: fuller illumination of the cell (by enlarging the emitter mesa area from ~5% of the cell area to nearly 100% of the cell area) and higher emitter temperature (by raising the maximum emitter temperature from 655 K to 1000 K) are expected to increase device efficiency to ~7% in the near-field. Although not as simple to solve, improving the design of low-bandgap (0.3-0.6 eV) cells to reduce non-radiative recombination is critical to the further development of TPV technology. Improvements to PV technology to date has focused largely on the 0.7-1.1 eV range because of its suitability in solar applications, but work to improve the efficiency and passivation of low-bandgap cells are required for NFTPV to be successful. Finally, optimizing the materials and geometry can lead to dramatic improvements in NFTPV performance. Employing thin-film cells with back reflectors holds the potential to improve efficiency further by reflecting sub-bandgap photons back at the emitter. Finally, the development of spectrally-selective emitters, which theoretically could be designed to emit photons resonantly at an energy just above the cell bandgap, will be key to maximizing the NFTPV device efficiency.

In addition to improving the device performance through refining the device design, a number of improvements to the experimental methodology will aid researchers in characterizing devices accurately. As mentioned in the previous section, interferometric measurement of the gap size will greatly reduce the uncertainty in the vacuum gap measurement, leading to more confident interpretations of the measured data. Further, in the future more accurate optical properties for both the emitter and cell should be obtained via infrared ellipsometry, which should lend itself to more accurate modeling (although in practice it may yet prove difficult to isolate the optical properties of the cell's active layer). Finally, future experiment designs should

integrate a means to directly measure the efficiency, rather than try to extract it from a fitted computational model.

After future NFTPV prototypes establish the feasibility of the technology in the laboratory, there remain several challenging goals for bringing NFTPVs to market. First, related to the requirement of maintaining sub-micron gaps between emitter and receiver, mechanical robustness and scaling to macroscopic systems will be difficult. The most promising technique that I have encountered so far for maintaining a fixed gap between macroscopic plates is the use of dielectric spacers, which can be specially-fabricated to minimize the parasitic conduction heat flow from emitter to cell.[245] Of course cost is also a crucial parameter, but at this early stage it is difficult to forecast those specifics.

Bibliography

1. Song, B., Fiorino, A., Meyhofer, E. & Reddy, P. Near-field radiative thermal transport: From theory to experiment. *AIP Adv.* **5**, 053503 (2015).

2. Song, B. et al. Radiative heat conductances between dielectric and metallic parallel plates with nanoscale gaps. *Nat. Nanotechnol.* **11**, 509-514 (2016).

3. Barr, E.S. Historical Survey of the Early Development of the Infrared Spectral Region. *American Journal of Physics* **28**, 42-54 (1960).

4. Herschel, W. Experiments on the refrangibility of the invisible rays of the Sun. *Philosophical Transactions of Royal Society of London* **90**, 284-292 (1800).

5. Herschel, W. Experiments on the solar, and on the terrestrial rays that occasion heat; with a comparative view of the laws to which light and heat, or rather rays which occasion them, are subject, in order to determine whether they are the same, or different. Part I. *Philosophical Transactions of Royal Society of London* **90**, 293-326 (1800).

6. Herschel, W. Experiments on the solar, and on the terrestrial rays that occasion heat; with a comparative view of the laws to which light and heat, or rather rays which occasion them, are subject, in order to determine whether they are the same, or different. Part II. *Philosophical Transactions of Royal Society of London* **90**, 437-538 (1800).

7. Planck, M. Über eine Verbesserung der Wien'schen Spectralgleichung. *Verhandlungen der Deutschen Physikalischen Gesellschaft* **2**, 202-204 (1900).

8. Planck, M. Zur Theorie des Gesetzes der Energieverteilung im Normalspectrum. *Verhandlungen der Deutschen Physikalischen Gesellschaft* **2**, 237-245 (1900).

9. Planck, M. The theory of heat radiation, Edn. 2nd. (P. Blakiston's Son & Co., Philadelphia, PA; 1914).

10. Haar, D.t. The old quantum theory, Edn. 1st. (Pergamon Press, Oxford, New York; 1967).

11. Bohm, D. Quantum theory. (Dover Publications, New York; 1989).

12. Kragh, H. Max Planck: the reluctant revolutionary. *Phys World* **13**, 31-35 (2000).

13. Callen, H.B. & Welton, T.A. Irreversibility and Generalized Noise. *Phys. Rev.* **83**, 34-40 (1951).

14. Kubo, R. Fluctuation-Dissipation Theorem. *Rep Prog Phys* **29**, 255-284 (1966).

15. Landau, L.D., Lifshitz, E.M. & Pitaevskii, L.P. Statistical physics, Edn. 3rd, rev. and enl. (Pergamon Press, Oxford; 1980).

16. Eckhardt, W. Macroscopic Theory of Electromagnetic Fluctuations and Stationary Radiative Heat-Transfer. *Phys Rev A* **29**, 1991-2003 (1984).

17. Rytov, S.M. Theory of electric fluctuations and thermal radiation. (Air Force Cambrige Research Center, Bedford, MA; 1953).

18. Rytov, S.M., Kravtsov, Y.A. & Tatarskii, V.I. Principles of statistical radiophysics. (Springer-Verlag, Berlin Heidelberg; 1989).

19. Emslie, A.G. in Aerodynamically Heated Structures. (ed. P.E. Glaser) (Prentice-Hall, Englewood Cliffs, NJ; 1962).

20. Pendry, J.B. Radiative exchange of heat between nanostructures. *J. Phys. - Condens. Mat.* **11**, 6621-6633 (1999).

21. Zhang, Z. Nano/microscale heat transfer. (McGraw-Hill, New York, NY; 2007).

22. Joulain, K., Mulet, J.-P., Marquier, F., Carminati, R. & Greffet, J.-J. Surface electromagnetic waves thermally excited: Radiative heat transfer, coherence properties and Casimir forces revisited in the near field. *Surf. Sci. Rep.* **57**, 59-112 (2005).

23. Volokitin, A.I. & Persson, B.N.J. Near-field radiative heat transfer and noncontact friction. *Reviews of Modern Physics* **79**, 1291-1329 (2007).

24. Basu, S., Zhang, Z.M. & Fu, C.J. Review of near-field thermal radiation and its application to energy conversion. *Int. J. Energy Res.* **33**, 1203-1232 (2009).

25. Dorofeyev, I.A. & Vinogradov, E.A. Fluctuating electromagnetic fields of solids. *Phys Rep* **504**, 75-143 (2011).

26. Jones, A.C., O'Callahan, B.T., Yang, H.U. & Raschke, M.B. The thermal near-field: Coherence, spectroscopy, heat-transfer, and optical forces. *Prog Surf Sci* **88**, 349-392 (2013).

27. Cahill, D.G. et al. Nanoscale thermal transport. II. 2003-2012. *Appl Phys Rev* **1** (2014).

28. Xuan, Y.M. An overview of micro/nanoscaled thermal radiation and its applications. *Photonic Nanostruct* **12**, 93-113 (2014).

29. Volokitin, A.I. & Persson, B.N.J. Radiative heat transfer and noncontact friction between nanostructures. *Physics-Uspekhi* **50**, 879-906 (2007).

30. Girard, C., Joachim, C. & Gauthier, S. The physics of the near-field. *Rep Prog Phys* **63**, 893-938 (2000).

31. Carminati, R. & Greffet, J.J. Near-field effects in spatial coherence of thermal sources. *Phys. Rev. Lett.* **82**, 1660-1663 (1999).

32. Greffet, J.J. et al. Coherent emission of light by thermal sources. *Nature* **416**, 61-64 (2002).

33. Marquier, F. et al. Coherent spontaneous emission of light by thermal sources. *Phys. Rev. B* **69** (2004).

34. Laroche, M. et al. Highly directional radiation generated by a tungsten thermal source. *Opt Lett* **30**, 2623-2625 (2005).

35. Laroche, M., Carminati, R. & Greffet, J.J. Coherent thermal antenna using a photonic crystal slab. *Phys. Rev. Lett.* **96** (2006).

36. Greffet, J.J. & Henkel, C. Coherent thermal radiation. *Contemp Phys* **48**, 183-194 (2007).

37. Henkel, C., Joulain, K., Carminati, R. & Greffet, J.J. Spatial coherence of thermal near fields. *Opt Commun* **186**, 57-67 (2000).

38. Shchegrov, A.V., Joulain, K., Carminati, R. & Greffet, J.J. Near-field spectral effects due to electromagnetic surface excitations. *Phys. Rev. Lett.* **85**, 1548-1551 (2000).

39. De Wilde, Y. et al. Thermal radiation scanning tunnelling microscopy. *Nature* **444**, 740-743 (2006).

40. Kittel, A. et al. Near-field thermal imaging of nanostructured surfaces. *Appl. Phys. Lett.* **93** (2008).

41. Wischnath, U.F., Welker, J., Munzel, M. & Kittel, A. The near-field scanning thermal microscope. *Rev. Sci. Instrum.* **79** (2008).

42. Kryder, M.H. et al. Heat Assisted Magnetic Recording. *P Ieee* **96**, 1810-1835 (2008).

43. Challener, W.A. et al. Heat-assisted magnetic recording by a near-field transducer with efficient optical energy transfer. *Nat Photonics* **3**, 220-224 (2009).

44. Stipe, B.C. et al. Magnetic recording at 1.5 Pb m(-2) using an integrated plasmonic antenna. *Nat Photonics* **4**, 484-488 (2010).

45. Zwol, P.J.v., Joulain, K., Ben-Abdallah, P. & Chevrier, J. Phonon polaritons enhance near-field thermal transfer across the phase transition of VO2. *Phys. Rev. B* **84** (2011).

46. Zwol, P.J.v., Joulain, K., Ben-Abdallah, P., Greffet, J.-J. & Chevrier, J. Fast nanoscale heat-flux modulation with phase-change materials. *Phys. Rev. B* **83** (2011).

47. Svetovoy, V.B., van Zwol, P.J. & Chevrier, J. Plasmon enhanced near-field radiative heat transfer for graphene covered dielectrics. *Phys. Rev. B* **85** (2012).

48. Cui, L.J., Huang, Y., Wang, J. & Zhu, K.Y. Ultrafast modulation of near-field heat transfer with tunable metamaterials. *Appl. Phys. Lett.* **102** (2013).

49. Vassant, S. et al. Electrical modulation of emissivity. *Appl. Phys. Lett.* **102** (2013).

50. Huang, Y., Boriskina, S.V. & Chen, G. Electrically tunable near-field radiative heat transfer via ferroelectric materials. *Appl. Phys. Lett.* **105** (2014).

51. Incardone, R., Emig, T. & Kruger, M. Heat transfer between anisotropic nanoparticles: Enhancement and switching. *Epl-Europhys Lett* **106** (2014).

52. Inoue, T., De Zoysa, M., Asano, T. & Noda, S. Realization of dynamic thermal emission control. *Nat. Mater.* **13**, 928-931 (2014).

53. Nikbakht, M. Radiative heat transfer in anisotropic many-body systems: Tuning and enhancement. *J. Appl. Phys.* **116** (2014).

54. Otey, C.R., Lau, W.T. & Fan, S.H. Thermal Rectification through Vacuum. *Phys. Rev. Lett.* **104** (2010).

55. Basu, S. & Francoeur, M. Near-field radiative transfer based thermal rectification using doped silicon. *Appl. Phys. Lett.* **98** (2011).

56. Iizuka, H. & Fan, S.H. Rectification of evanescent heat transfer between dielectric-coated and uncoated silicon carbide plates. *J. Appl. Phys.* **112** (2012).

57. Ben-Abdallah, P. & Biehs, S.A. Phase-change radiative thermal diode. *Appl. Phys. Lett.* **103** (2013).

58. Huang, J.G., Li, Q., Zheng, Z.H. & Xuan, Y.M. Thermal rectification based on thermochromic materials. *Int. J. Heat Mass Transfer* **67**, 575-580 (2013).

59. Wang, L.p. & Zhang, Z.m. Thermal rectification enabled by near field radiative heat transfer between instrinsic silicon and a dissimilar material

Nanoscale Microscale Thermophys. Eng. **17**, 337-348 (2013).

60. Zhu, L.X., Otey, C.R. & Fan, S.H. Ultrahigh-contrast and large-bandwidth thermal rectification in near-field electromagnetic thermal transfer between nanoparticles. *Phys. Rev. B* **88** (2013).

61. Chen, Z. et al. A photon thermal diode. *Nat. Commun.* **5** (2014).

62. Iizuka, H. & Fan, S.H. Consideration of enhancement of thermal rectification using metamaterial models. *J. Quant. Spectrosc. Radiat. Transfer* **148**, 156-164 (2014).

63. Nefzaoui, E., Drevillon, J., Ezzahri, Y. & Joulain, K. Simple far-field radiative thermal rectifier using Fabry-Perot cavities based infrared selective emitters. *Appl Optics* **53**, 3479-3485 (2014).

64. Messina, R., Antezza, M. & Ben-Abdallah, P. Three-Body Amplification of Photon Heat Tunneling. *Phys. Rev. Lett.* **109** (2012).

65. Ben-Abdallah, P. & Biehs, S.A. Near-Field Thermal Transistor. *Phys. Rev. Lett.* **112**, 044301 (2014).

66. Elzouka, M. & Ndao, S. Near-field NanoThermoMechanical memory. *Appl. Phys. Lett.* **105** (2014).

67. Kubytskyi, V., Biehs, S.A. & Ben-Abdallah, P. Radiative Bistability and Thermal Memory. *Phys. Rev. Lett.* **113** (2014).

68. DiMatteo, R.S. et al. Enhanced photogeneration of carriers in a semiconductor via coupling across a nonisothermal nanoscale vacuum gap. *Appl. Phys. Lett.* **79**, 1894-1896 (2001).

69. Narayanaswamy, A. & Chen, G. Surface modes for near field thermophotovoltaics. *Appl. Phys. Lett.* **82**, 3544-3546 (2003).

70. Laroche, M., Carminati, R. & Greffet, J.J. Near-field thermophotovoltaic energy conversion. *J. Appl. Phys.* **100**, 063704 (2006).

71. Park, K., Basu, S., King, W.P. & Zhang, Z.M. Performance analysis of near-field thermophotovoltaic devices considering absorption distribution. *J. Quant. Spectrosc. Radiat. Transfer* **109**, 305-316 (2008).

72. Dillner, U. Can Thermotunneling Improve the Currently Realized Thermoelectric Conversion Efficiency? *J Electron Mater* **39**, 1645-1649 (2010).

73. Francoeur, M., Vaillon, R. & Mengüç, M.P. Thermal Impacts on the Performance of Nanoscale-Gap Thermophotovoltaic Power Generators. *IEEE T. Energy Conver.* **26**, 686-698 (2011).

74. Messina, R. & Ben-Abdallah, P. Graphene-based photovoltaic cells for near-field thermal energy conversion. *Sci. Rep.* **3** (2013).

75. Zhao, B., Wang, L.P., Shuai, Y. & Zhang, Z.M.M. Thermophotovoltaic emitters based on a two-dimensional grating/thin-film nanostructure. *Int. J. Heat Mass Transfer* **67**, 637-645 (2013).

76. Guo, Y., Molesky, S., Hu, H., Cortes, C.L. & Jacob, Z. Thermal excitation of plasmons for near-field thermophotovoltaics. *Appl. Phys. Lett.* **105**, 073903 (2014).

77. Lenert, A. et al. A nanophotonic solar thermophotovoltaic device. *Nat. Nanotechnol.* **9**, 126-130 (2014).

78. Svetovoy, V.B. & Palasantzas, G. Graphene-on-Silicon Near-Field Thermophotovoltaic Cell. *Phys Rev Appl* **2** (2014).

79. Whale, M.D. & Cravalho, E.G. Modeling and performance of microscale thermophotovoltaic energy conversion devices. *IEEE T. Energy Conver.* **17**, 130-142 (2002).

80. Basu, S., Chen, Y.B. & Zhang, Z.M. Microscale radiation in thermophotovoltaic devices - A review. *Int. J. Energy Res.* **31**, 689-716 (2007).

81. Yang, R.G., Narayanaswamy, A. & Chen, G. Surface-plasmon coupled nonequilibrium thermoelectric refrigerators and power generators. *J Comput Theor Nanos* **2**, 75-87 (2005).

82. Fang, J., Frederich, H. & Pilon, L. Harvesting Nanoscale Thermal Radiation Using Pyroelectric Materials. *J. Heat Trans. - T. of ASME* **132** (2010).

83. Schwede, J.W. et al. Photon-enhanced thermionic emission for solar concentrator systems. *Nat. Mater.* **9**, 762-767 (2010).

84. Lee, J.H., Bargatin, I., Melosh, N.A. & Howe, R.T. Optimal emitter-collector gap for thermionic energy converters. *Appl. Phys. Lett.* **100** (2012).

85. Modest, M.F. Radiative Heat Transfer, Edn. 3rd. (Academic Press, Oxford, UK; 2013).

86. Siegel, R. & R.Howell, J. Thermal radiation heat transfer, Edn. 4th. (Taylor & Francis, New York; 2002).

87. Bijl, D. Note on thermal radiation at low temperatures. *Philos. Mag.* **43**, 1342-1344 (1952).

88. Dalvit, D., Milonni, P., Roberts, D. & da Rosa, F. (Springer-Verlag, Berlin, Heidelberg; 2011).

89. Cravalho, E.G., Tien, C.-L. & Caren, R.P. Effect of Small Spacings on Radiative Transfer between 2 Dielectrics. *J. Heat Transfer* **89**, 351-358 (1967).

90. Olivei, A. Transfert d'energie thermique rayonnante entre deux delectriques aux tres basses temperatures. *Revue de Physique Appliquee* **3**, 225-230 (1968).

91. Boehm, R.F. & Tien, C.L. Small Spacing Analysis of Radiative Parallel Metallic Surfaces. *Mech Eng* **92**, 70-& (1970).

92. Polder, D. & Hove, M.A.V. Theory of Radiative Heat Transfer between Closely Spaced Bodies. *Phys. Rev. B* **4**, 3303-3314 (1971).

93. Caren, R.P. Radiation Energy Density and Radiation Heat-Flux in Small Rectangular Cavities. *J. Heat Transfer* **94**, 289-294 (1972).

94. Caren, R.P. Radiation Heat-Transfer between Closely Spaced Metal-Surfaces at Low-Temperature - Impact of Discrete Modes of Radiation Field. *J. Heat Transfer* **94**, 295-299 (1972).

95. Caren, R.P. Thermal-Radiation between Closely Spaced Metal-Surfaces at Low-Temperature Due to Travelling and Quasi-Stationary Components of Radiation-Field. *Int. J. Heat Mass Transfer* **17**, 755-765 (1974).

96. Levin, M.L., Polevoi, V.G. & Rytov, S.M. Contribution to the theory of heat exchange due to a fluctuating electromagnetic field. *Soviet Physics, JETP* **52**, 1054-1063 (1980).

97. Loomis, J.J. & Maris, H.J. Theory of Heat-Transfer by Evanescent Electromagnetic-Waves. *Phys. Rev. B* **50**, 18517-18524 (1994).

98. Cravalho, E.G., Domoto, G.A. & Tien, C.L. in AIAA 3rd Thermophysics Conference (Los Angeles, CA; 1968).

99. Hargreaves, C.M. Anomalous Radiative Transfer between Closely-Spaced Bodies. *Phys. Lett. A* **A 30**, 491-492 (1969).

100. Domoto, G., Boehm, R.F. & Tien, C.-L. Experimental Investigation of Radiative Transfer between Metallic Surfaces at Cryogenic Temperatures. *J. Heat Transfer* **92**, 412-416 (1970).

101. Hargreaves, C.M. Radiative-Transfer between Closely Spaced Bodies. *Philips Res Rep*, 1-80 (1973).

102. Kutateladze, S.S., Robtsov, N.A. & Baltsevich, Y., A. Effect of magnitude of gap between metal plates on their thermal interaction at cryogenic temperatures. *Soviet Physics Doklady* **23**, 577-578 (1978).

103. Baltsevich, Y.A. & Rubtsov, N.A. Experimental investigation of low-temperature radiative transfer between parallel metallic surfaces as function of the spacing between these surfaces. *Heat Transfer-Soviet Research* **12**, 117-133 (1980).

104. Messina, R. & Antezza, M. Scattering-matrix approach to Casimir-Lifshitz force and heat transfer out of thermal equilibrium between arbitrary bodies. *Phys Rev A* **84** (2011).

105. Kruger, M., Bimonte, G., Emig, T. & Kardar, M. Trace formulas for nonequilibrium Casimir interactions, heat radiation, and heat transfer for arbitrary objects. *Phys. Rev. B* **86** (2012).

106. Rodriguez, A.W., Reid, M.T.H. & Johnson, S.G. Fluctuating-surface-current formulation of radiative heat transfer: Theory and applications. *Phys. Rev. B* **88** (2013).

107. Narayanaswamy, A. & Zheng, Y. A Green's function formalism of energy and momentum transfer in fluctuational electrodynamics. *J. Quant. Spectrosc. Radiat. Transfer* **132**, 12-21 (2014).

108. Otey, C.R., Zhu, L.X., Sandhu, S. & Fan, S.H. Fluctuational electrodynamics calculations of near-field heat transfer in non-planar geometries: A brief overview. *J. Quant. Spectrosc. Radiat. Transfer* **132**, 3-11 (2014).

109. Budaev, B.V. & Bogy, D.B. On the mechanisms of heat transport across vacuum gaps. *Z Angew Math Phys* **62**, 1143-1158 (2011).

110. Budaev, B.V. & Bogy, D.B. Extension of Planck's law to steady heat flux across nanoscale gaps. *Appl Phys a-Mater* **103**, 971-975 (2011).

111. Budaev, B.V. & Bogy, D.B. Computation of radiative heat transport across a nanoscale vacuum gap. *Appl. Phys. Lett.* **104** (2014).

112. Jackson, J.D. Classical electrodynamics, Edn. 3rd. (Wiley, New York; 1999).

113. Kong, J.A. Electromagnetic wave theory. (EMW Publishing, Cambridge, MA; 2008).

114. Joulain, K., Drevillon, J. & Ben-Abdallah, P. Noncontact heat transfer between two metamaterials. *Phys. Rev. B* **81** (2010).

115. Zheng, Z.H. & Xuan, Y.M. Theory of near-field radiative heat transfer for stratified magnetic media. *Int. J. Heat Mass Transfer* **54**, 1101-1110 (2011).

116. Tai, C.-t., IEEE Antennas and Propagation Society. & IEEE Microwave Theory and Techniques Society. Dyadic green functions in electromagnetic theory, Edn. 2nd. (IEEE Press, Piscataway, NJ; 1994).

117. Sipe, J.E. New Green-Function Formalism for Surface Optics. *J Opt Soc Am B* **4**, 481-489 (1987).

118. Biehs, S.A., Rousseau, E. & Greffet, J.J. Mesoscopic Description of Radiative Heat Transfer at the Nanoscale. *Phys. Rev. Lett.* **105**, 4 (2010).

119. Ben-Abdallah, P., Joulain, K. & Pryamikov, A. Surface Bloch waves mediated heat transfer between two photonic crystals. *Appl. Phys. Lett.* **96**, 143117 (2010).

120. Narayanaswamy, A. & Chen, G. Thermal emission control with one-dimensional metallodielectric photonic crystals. *Phys. Rev. B* **70** (2004).

121. Narayanaswamy, A. & Chen, G. Thermal radiation in 1D photonic crystals. *J. Quant. Spectrosc. Radiat. Transfer* **93**, 175-183 (2005).

122. Pryamikov, A., Joulain, K., Ben-Abdallah, P. & Drevillon, J. Role of confined Bloch waves in the near field heat transfer between two photonic crystals. *J. Quant. Spectrosc. Radiat. Transfer* **112**, 1314-1322 (2011).

123. Biehs, S.-A., Ben-Abdallah, P., Rosa, F.D., Joulain, K. & Greffet, J.-J. Nanoscale heat flux between nanoporous materials. *Opt. Express* **19**, A1088-A1103 (2011).

124. Nefedov, I.S. & Simovski, C.R. Giant radiation heat transfer through micron gaps. *Phys. Rev. B* **84** (2011).

125. Bai, Y., Jiang, Y.Y. & Liu, L.H. Role of surface plasmon polaritons on the enhancement of the near-field thermal radiation from fishnet metamaterial. *J. Phys. D: Appl. Phys.* **47** (2014).

126. Liu, X.L., Zhang, R.Z. & Zhang, Z.M. Near-field radiative heat transfer with doped-silicon nanostructured metamaterials. *Int. J. Heat Mass Transfer* **73**, 389-398 (2014).

127. Cui, L.J., Huang, Y. & Wang, J. Near-field radiative heat transfer between chiral metamaterials. *J. Appl. Phys.* **112** (2012).

128. Francoeur, M., Basu, S. & Petersen, S.J. Electric and magnetic surface polariton mediated near-field radiative heat transfer between metamaterials made of silicon carbide particles. *Opt. Express* **19**, 18774-18788 (2011).

129. Volokitin, A.I. & Persson, B.N.J. Radiative heat transfer between nanostructures. *Phys. Rev. B* **63** (2001).

130. Francoeur, M. & Menguc, M.P. Role of fluctuational electrodynamics in near-field radiative heat transfer. *J. Quant. Spectrosc. Radiat. Transfer* **109**, 280-293 (2008).

131. Basu, S. & Wang, L.P. Near-field radiative heat transfer between doped silicon nanowire arrays. *Appl. Phys. Lett.* **102** (2013).

132. Dyakov, S.A., Dai, J., Yan, M. & Qiu, M. Thermal radiation dynamics in two parallel plates: The role of near field. *Phys. Rev. B* **90** (2014).

133. Volokitin, A.I. & Persson, B.N.J. Near-field radiative heat transfer between closely spaced graphene and amorphous SiO2. *Phys. Rev. B* **83** (2011).

134. Ilic, O. et al. Near-field thermal radiation transfer controlled by plasmons in graphene. *Phys. Rev. B* **85** (2012).

135. Lim, M., Lee, S.S. & Lee, B.J. Near-field thermal radiation between graphene-covered doped silicon plates. *Opt. Express* **21**, 22173-22185 (2013).

136. Drosdoff, D., Phan, A.D. & Woods, L.M. Transverse Electric Mode for Near-Field Radiative Heat Transfer in Graphene-Metamaterial Systems. *Adv Opt Mater* **2**, 1038-1042 (2014).

137. Biehs, S.A., Rosa, F.S.S. & Ben-Abdallah, P. Modulation of near-field heat transfer between two gratings. *Appl. Phys. Lett.* **98**, 243102 (2011).

138. Biehs, S.A., Tschikin, M. & Ben-Abdallah, P. Hyperbolic Metamaterials as an Analog of a Blackbody in the Near Field. *Phys. Rev. Lett.* **109** (2012).

139. Guo, Y., Cortes, C.L., Molesky, S. & Jacob, Z. Broadband super-Planckian thermal emission from hyperbolic metamaterials. *Appl. Phys. Lett.* **101** (2012).

140. Biehs, S.A., Tschikin, M., Messina, R. & Ben-Abdallah, P. Super-Planckian near-field thermal emission with phonon-polaritonic hyperbolic metamaterials. *Appl. Phys. Lett.* **102** (2013).

141. Guo, Y. & Jacob, Z.B. Thermal hyperbolic metamaterials. *Opt. Express* **21**, 15014-15019 (2013).

142. Liu, X.L., Zhang, R.Z. & Zhang, Z.M. Near-field thermal radiation between hyperbolic metamaterials: Graphite and carbon nanotubes. *Appl. Phys. Lett.* **103** (2013).

143. Guo, Y. & Jacob, Z. Fluctuational electrodynamics of hyperbolic metamaterials. *J. Appl. Phys.* **115** (2014).

144. Miller, O.D., Johnson, S.G. & Rodriguez, A.W. Effectiveness of Thin Films in Lieu of Hyperbolic Metamaterials in the Near Field. *Phys. Rev. Lett.* **112** (2014).

145. Nefedov, I.S. & Melnikov, L.A. Super-Planckian far-zone thermal emission from asymmetric hyperbolic metamaterials. *Appl. Phys. Lett.* **105** (2014).

146. Basu, S. & Zhang, Z. Maximum energy transfer in near-field thermal radiation at nanometer distances. *J. Appl. Phys.* **105** (2009).

147. Wang, X., Basu, S. & Zhang, Z. Parametric optimization of dielectric functions for maximizing nanoscale radiative transfer. *J. Phys. D: Appl. Phys.* **42** (2009).

148. Ben-Abdallah, P. & Joulain, K. Fundamental limits for noncontact transfers between two bodies. *Phys. Rev. B* **82** (2010).

149. Basu, S. & Francoeur, M. Maximum near-field radiative heat transfer between thin films. *Appl. Phys. Lett.* **98** (2011).

150. Zhao, Y., Tang, G.H. & Li, Z.Y. Parametric investigation for suppressing near-field thermal radiation between two spherical nanoparticles. *Int Commun Heat Mass* **39**, 918-922 (2012).

151. Nefzaoui, E., Ezzahri, Y., Drevillon, J. & Joulain, K. Maximal near-field radiative heat transfer between two plates. *Eur. Phys. J. Appl. Phys.* **63**, 30902 (2013).

152. Simovski, C., Maslovski, S., Nefedov, I. & Tretyakov, S. Optimization of radiative heat transfer in hyperbolic metamaterials for thermophotovoltaic applications. *Opt. Express* **21**, 14988-15013 (2013).

153. Francoeur, M., Menguc, M.P. & Vaillon, R. Solution of near-field thermal radiation in one-dimensional layered media using dyadic Green's functions and the scattering matrix method. *J. Quant. Spectrosc. Radiat. Transfer* **110**, 2002-2018 (2009).

154. Francoeur, M., Mengüç, M.P. & Vaillon, R. Coexistence of multiple regimes for near-field thermal radiation between two layers supporting surface phonon polaritons in the infrared. *Phys. Rev. B* **84** (2011).

155. Zheng, Z.H. & Xuan, Y.M. Near-field radiative heat transfer between general materials and metamaterials. *Chinese Sci Bull* **56**, 2312-2319 (2011).

156. Mulet, J.P., Joulain, K., Carminati, R. & Greffet, J.J. Enhanced radiative heat transfer at nanometric distances. *Microscale Thermophys. Eng.* **6**, 209-222 (2002).

157. Biehs, S.A. & Greffet, J.J. Influence of roughness on near-field heat transfer between two plates. *Phys. Rev. B* **82** (2010).

158. Fu, C. & Zhang, Z. Nanoscale radiation heat transfer for silicon at different doping levels. *Int. J. Heat Mass Transfer* **49**, 1703-1718 (2006).

159. Rousseau, E., Laroche, M. & Greffet, J.J. Radiative heat transfer at nanoscale mediated by surface plasmons for highly doped silicon. *Appl. Phys. Lett.* **95** (2009).

160. Rousseau, E., Laroche, M. & Greffet, J.J. Radiative heat transfer at nanoscale: Closed-form expression for silicon at different doping levels. *J. Quant. Spectrosc. Radiat. Transfer* **111**, 1005-1014 (2010).

161. Liu, B.A., Shi, J.W., Liew, K. & Shen, S. Near-field radiative heat transfer for Si based metamaterials. *Opt Commun* **314**, 57-65 (2014).

162. Chapuis, P.O., Volz, S., Henkel, C., Joulain, K. & Greffet, J.J. Effects of spatial dispersion in near-field radiative heat transfer between two parallel metallic surfaces. *Phys. Rev. B* **77**, 9 (2008).

163. Zheng, Y. & Narayanaswamy, A. Patch contribution to near-field radiative energy transfer and van der Waals pressure between two half-spaces. *Phys Rev A* **89** (2014).

164. Biehs, S.A. Thermal heat radiation, near-field energy density and near-field radiative heat transfer of coated materials. *Eur Phys J B* **58**, 423-431 (2007).

165. Biehs, S.A., Reddig, D. & Holthaus, M. Thermal radiation and near-field energy density of thin metallic films. *Eur Phys J B* **55**, 237-251 (2007).

166. Francoeur, M., Menguc, M.P. & Vaillon, R. Near-field radiative heat transfer enhancement via surface phonon polaritons coupling in thin films. *Appl. Phys. Lett.* **93**, 089901 (2008).

167. Ben-Abdallah, P., Joulain, K., Drevillon, J. & Domingues, G. Near-field heat transfer mediated by surface wave hybridization between two films. *J. Appl. Phys.* **106** (2009).

168. Fu, C.J. & Tan, W.C. Near-field radiative heat transfer between two plane surfaces with one having a dielectric coating. *J. Quant. Spectrosc. Radiat. Transfer* **110**, 1027-1036 (2009).

169. Francoeur, M., Menguc, M.P. & Vaillon, R. Spectral tuning of near-field radiative heat flux between two thin silicon carbide films. *J. Phys. D: Appl. Phys.* **43** (2010).

170. Francoeur, M., Mengüç, M.P. & Vaillon, R. Control of near-field radiative heat transfer via surface phonon-polariton coupling in thin films. *Appl Phys a-Mater* **103**, 547-550 (2011).

171. Wang, L.P., Basu, S. & Zhang, Z.M. Direct and Indirect Methods for Calculating Thermal Emission From Layered Structures With Nonuniform Temperatures. *J. Heat Trans. - T. of ASME* **133** (2011).

172. Carrillo, L.Y. & Bayazitoglu, Y. Nanorod near-field radiative heat exchange analysis. *J. Quant. Spectrosc. Radiat. Transfer* **112**, 412-419 (2011).

173. Carrillo, L.Y. & Bayazitoglu, Y. Sphere Approximation for Nanorod near-Field Radiative Heat Exchange Analysis. *Nanoscale Microscale Thermophys. Eng.* **15**, 195-208 (2011).

174. Mulet, J.-P., Joulain, K., Carminati, R. & Greffet, J.-J. Nanoscale radiative heat transfer between a small particle and a plane surface. *Appl. Phys. Lett.* **78**, 2931-2933 (2001).

175. Chapuis, P.-O., Greffet, J.-J., Joulain, K. & Volz, S. Heat transfer between a nano-tip and a surface. *Nanotechnology* **17**, 2978-2981 (2006).

176. Biehs, S.A., Huth, O. & Ruting, F. Near-field radiative heat transfer for structured surfaces. *Phys. Rev. B* **78** (2008).

177. Chapuis, P.O., Laroche, M., Volz, S. & Greffet, J.J. Near-field induction heating of metallic nanoparticles due to infrared magnetic dipole contribution. *Phys. Rev. B* **77** (2008).

178. Biehs, S.-A. & Greffet, J.-J. Near-field heat transfer between a nanoparticle and a rough surface. *Phys. Rev. B* **81** (2010).

179. Narayanaswamy, A. & Chen, G. Thermal near-field radiative transfer between two spheres. *Phys. Rev. B* **77** (2008).

180. Carrillo, L.Y. & Bayazitoglu, Y. Nanosphere Near-Field Radiative Heat-Exchange Analysis. *J Thermophys Heat Tr* **24**, 309-315 (2010).

181. Sasihithlu, K. & Narayanaswamy, A. Convergence of vector spherical wave expansion method applied to near-field radiative transfer. *Opt. Express* **19**, A772-A785 (2011).

182. Sasihithlu, K. & Narayanaswamy, A. Proximity effects in radiative heat transfer. *Phys. Rev. B* **83** (2011).

183. Roberts, N.A. & Walker, D.G. A review of thermal rectification observations and models in solid materials. *Int J Therm Sci* **50**, 648-662 (2011).

184. Li, N.B. et al. Colloquium: Phononics: Manipulating heat flow with electronic analogs and beyond. *Reviews of Modern Physics* **84**, 1045-1066 (2012).

185. Hu, L., Narayanaswamy, A., Chen, X.Y. & Chen, G. Near-field thermal radiation between two closely spaced glass plates exceeding Planck's blackbody radiation law. *Appl. Phys. Lett.* **92**, 133106 (2008).

186. Ottens, R.S. et al. Near-Field Radiative Heat Transfer between Macroscopic Planar Surfaces. *Phys. Rev. Lett.* **107**, 014301 (2011).

187. Kralik, T. et al. Strong Near-Field Enhancement of Radiative Heat Transfer between Metallic Surfaces. *Phys. Rev. Lett.* **109** (2012).

188. Kralik, T., Hanzelka, P., Musilova, V., Srnka, A. & Zobac, M. Cryogenic apparatus for study of near-field heat transfer. *Rev. Sci. Instrum.* **82** (2011).

189. Feng, C., Tang, Z.A. & Yu, J. A Novel CMOS Device Capable of Measuring Near-Field Thermal Radiation. *Chinese Phys Lett* **29** (2012).

190. Feng, C., Tang, Z.N., Yu, J. & Sun, C.Y. A MEMS Device Capable of Measuring Near-Field Thermal Radiation between Membranes. *Sensors-Basel* **13**, 1998-2010 (2013).

191. St-Gelais, R., Guha, B., Zhu, L.X., Fan, S.H. & Lipson, M. Demonstration of Strong Near-Field Radiative Heat Transfer between Integrated Nanostructures. *Nano Lett.* **14**, 6971-6975 (2014).

192. Joulain, K., Mulet, J.P., Marquier, F., Carminati, R. & Greffet, J.J. Surface electromagnetic waves thermally excited: Radiative heat transfer, coherence properties and Casimir forces revisited in the near field. *Surf. Sci. Rep.* **57**, 59-112 (2005).

193. Polder, D. & van Hove, M.A. Theory of Radiative Heat Transfer between Closely Spaced Bodies. *Phys. Rev. B* **4**, 3303-3314 (1971).

194. Ganjeh, Y. et al. A platform to parallelize planar surfaces and control their spatial separation with nanometer resolution. *Rev. Sci. Instrum.* **83**, 105101 (2012).

195. Song, B. et al. Enhancement of near-field radiative heat transfer using polar dielectric thin films. *Nat. Nanotechnol.* **10**, 253-258 (2015).

196. Rousseau, E. et al. Radiative heat transfer at the nanoscale. *Nat Photonics* **3**, 514-517 (2009).

197. Shen, S., Narayanaswamy, A. & Chen, G. Surface Phonon Polaritons Mediated Energy Transfer between Nanoscale Gaps. *Nano Lett.* **9**, 2909-2913 (2009).

198. Fiorino, A. et al. Giant enhancement in radiative heat transfer in sub-30 nm gaps of plane parallel surfaces. *Submitted for publication at Nano Letters.* (2018).

199. Joulain, K., Mulet, J.P., Marquier, F., Carminati, R. & Greffet, J.J. Surface electromagnetic waves thermally excited: Radiative heat transfer, coherence properties and Casimir forces revisited in the near field. *Surf. Sci. Rep.* **57**, 59-112 (2005).

200. Chen, K.F., Santhanam, P., Sandhu, S., Zhu, L. & Fan, S. Heat-flux control and solid-state cooling by regulating chemical potential of photons in near-field electromagnetic heat transfer. *Phys. Rev. B* **91**, 134301 (2015).

201. Biehs, S.A., Ben-Abdallah, P., Rosa, F.S.S., Joulain, K. & Greffet, J.J. Nanoscale heat flux between nanoporous materials. *Opt. Express* **19**, A1088-A1103 (2011).

202. van Zwol, P.J., Joulain, K., Ben-Abdallah, P. & Chevrier, J. Phonon polaritons enhance near-field thermal transfer across the phase transition of VO2. *Phys. Rev. B* **84**, 161413 (2011).

203. Guha, B., Otey, C., Poitras, C.B., Fan, S.H. & Lipson, M. Near-Field Radiative Cooling of Nanostructures. *Nano Lett.* **12**, 4546-4550 (2012).

204. Worbes, L., Hellmann, D. & Kittel, A. Enhanced Near-Field Heat Flow of a Monolayer Dielectric Island. *Phys. Rev. Lett.* **110**, 134302 (2013).

205. Kittel, A. et al. Near-field heat transfer in a scanning thermal microscope. *Phys. Rev. Lett.* **95**, 224301 (2005).

206. Cui, L.J. et al. Study of radiative heat transfer in angstrom- and nanometre-sized gaps. *Nat. Commun.* **8**, 14479 (2017).

207. Kim, K. et al. Radiative heat transfer in the extreme near field. *Nature* **528**, 387-391 (2015).

208. Narayanaswamy, A., Shen, S. & Chen, G. Near-field radiative heat transfer between a sphere and a substrate. *Phys. Rev. B* **78**, 115303 (2008).

209. van Zwol, P.J., Thiele, S., Berger, C., de Heer, W.A. & Chevrier, J. Nanoscale Radiative Heat Flow due to Surface Plasmons in Graphene and Doped Silicon. *Phys. Rev. Lett.* **109**, 264301 (2012).

210. van Zwol, P.J., Ranno, L. & Chevrier, J. Tuning Near Field Radiative Heat Flux through Surface Excitations with a Metal Insulator Transition. *Phys. Rev. Lett.* **108**, 234301 (2012).

211. Polder, D. & Van Hove, M. Theory of radiative heat transfer between closely spaced bodies. *Phys. Rev. B* **4**, 3303-3314 (1971).

212. Bernardi, M.P., Milovich, D. & Francoeur, M. Radiative heat transfer exceeding the blackbody limit between macroscale planar surfaces separated by a nanosize vacuum gap. *Nat. Commun.* **7**, 12900 (2016).

213. St-Gelais, R., Guha, B., Zhu, L., Fan, S. & Lipson, M. Demonstration of strong near-field radiative heat transfer between integrated nanostructures. *Nano Lett.* **14**, 6971-6975 (2014).

214. St-Gelais, R., Zhu, L., Fan, S. & Lipson, M. Near-field radiative heat transfer between parallel structures in the deep subwavelength regime. *Nat. Nanotechnol.* **11**, 515-519 (2016).

215. Wang, L.P. & Zhang, Z.M. Thermal Rectification Enabled by Near-Field Radiative Heat Transfer Between Intrinsic Silicon and a Dissimilar Material. *Nanoscale Microscale Thermophys. Eng.* **17**, 337-348 (2013).

216. Palik, E.D. Handbook of Optical Constants of Solids. (Academic Press, San Diego; 1998).

217. Cahill, D.G. Thermal-Conductivity Measurement from 30-K to 750-K - the 3-Omega Method. *Rev. Sci. Instrum.* **61**, 802-808 (1990).

218. Rytov, S.M., Kravtsov, I.U.A. & Tatarskii, V.I. Principles of Statistical Radiophysics 2. (Springer-Verlag, Berlin; 1987).

219. Fiorino, A. et al. A thermal diode based on nanoscale thermal radiation. *Submitted for publication at ACS Nano.* (2018).

220. Chi, S.W. Heat pipe theory and practice : a sourcebook. (Hemisphere Pub. Corp., Washington; 1976).

221. Yang, Y., Basu, S. & Wang, L.P. Radiation-based near-field thermal rectification with phase transition materials. *Appl. Phys. Lett.* **103** (2013).

222. Nefzaoui, E., Joulain, K., Drevillon, J. & Ezzahri, Y. Radiative thermal rectification using superconducting materials. *Appl. Phys. Lett.* **104** (2014).

223. Dyakov, S.A., Dai, J., Yan, M. & Qiu, M. Near field thermal memory based on radiative phase bistability of VO2. *J. Phys. D: Appl. Phys.* **48** (2015).

224. Yang, Y., Basu, S. & Wang, L.P. Vacuum thermal switch made of phase transition materials considering thin film and substrate effects. *J. Quant. Spectrosc. Radiat. Transfer* **158**, 69-77 (2015).

225. Ghanekar, A., Ji, J. & Zheng, Y. High-rectification near-field thermal diode using phase change periodic nanostructure. *Appl. Phys. Lett.* **109** (2016).

226. Zheng, Z.H., Liu, X.L., Wang, A. & Xuan, Y.M. Graphene-assisted near-field radiative thermal rectifier based on phase transition of vanadium dioxide (VO2). *Int. J. Heat Mass Transfer* **109**, 63-72 (2017).

227. Mott, N.F. & Friedman, L. Metal-Insulator Transitions in Vo2, Ti2o3 and Ti2-Xvxo3. *Philos. Mag.* **30**, 389-402 (1974).

228. Barker, A.S., Verleur, H.W. & Guggenheim, H.J. Infrared Optical Properties of Vanadium Dioxide above and Below Transition Temperature. *Phys. Rev. Lett.* **17**, 1286-1289 (1966).

229. van Zwol, P.J., Joulain, K., Ben Abdallah, P., Greffet, J.J. & Chevrier, J. Fast nanoscale heat-flux modulation with phase-change materials. *Phys. Rev. B* **83** (2011).

230. Ito, K., Nishikawa, K., Miura, A., Toshiyoshi, H. & Iizuka, H. Dynamic Modulation of Radiative Heat Transfer beyond the Blackbody Limit. *Nano Lett.* **17**, 4347-4353 (2017).

231. Ito, K., Nishikawa, K., Iizuka, H. & Toshiyoshi, H. Experimental investigation of radiative thermal rectifier using vanadium dioxide. *Appl. Phys. Lett.* **105** (2014).

232. Garry, G., Durand, O. & Lordereau, A. Structural, electrical and optical properties of pulsed laser deposited VO2 thin films on R- and C-sapphire planes. *Thin Solid Films* **453**, 427-430 (2004).

233. Basu, S., Lee, B.J. & Zhang, Z.M. Near-field radiation calculated with an improved dielectric function model for doped silicon. *J. Heat Transfer* **132**, 023302 (2010).

234. Fiorino, A. et al. Nanogap near-field thermophotovoltaics. *Submitted for publication at Nature Nanotechnol.* (2018).

235. Glassbrenner, C.J. & Slack, G.A. Thermal conductivity of silicon and germanium from 3 K to melting point. *Phys. Rev.* **134**, 1058-1069 (1964).

236. Lacy, F. Developing a theoretical relationship between electrical resistivity, temperature, and film thickness for conductors. *Nanoscale Res. Lett.* **6**, 1-14 (2011).

237. He, J. & Tritt, T.M. Advances in thermoelectric materials research: Looking back and moving forward. *Science* **357**, 1369-1377 (2017).

238. Snyder, G.J. & Toberer, E.S. Complex thermoelectric materials. *Nat. Mater.* **7**, 105-114 (2008).

239. Bright, T.J., Wang, L.P. & Zhang, Z.M. Performance of near-field thermophotovoltaic cells enhanced with a backside reflector. *J. Heat Trans. - T. of ASME* **136**, 062701 (2014).

240. Tong, J.K., Hsu, W.C., Huang, Y., Boriskina, S.V. & Chen, G. Thin-film 'thermal well' emitters and absorbers for high-efficiency thermophotovoltaics. *Sci. Rep.* **5**, 10661 (2015).

241. Chen, K.F., Santhanam, P. & Fan, S.H. Suppressing sub-bandgap phonon-polariton heat transfer in near-field thermophotovoltaic devices for waste heat recovery. *Appl. Phys. Lett.* **107**, 091106 (2015).

242. Lau, J.Z.J. & Wong, B.T. Thermal energy conversion using near-field thermophotovoltaic device composed of a thin-film tungsten radiator and a thin-film silicon cell. *J. Appl. Phys.* **122**, 084302 (2017).

243. Zhao, B. et al. High-performance near-field thermophotovoltaics for waste heat recovery. *Nano Energy* **41**, 344-350 (2017).

244. Molesky, S. & Jacob, Z. Ideal near-field thermophotovoltaic cells. *Phys. Rev. B* **91** (2015).

245. DiMatteo, R. et al. Micron-gap ThermoPhotoVoltaics (MTPV). *AIP Conf. Proc.* **738**, 42-51 (2004).

246. Whittaker, D.M. & Culshaw, I.S. Scattering-matrix treatment of patterned multilayer photonic structures. *Phys. Rev. B* **60**, 2610 (1999).

247. Yeh, P. *Optical Waves in Layered Media*. (Wiley, New York; 1988).

248. Zhu, L. & Fan, S. Near-complete violation of detailed balance in thermal radiation. *Phys. Rev. B* **90**, 220301 (2014).

249. Stoyanov, N.D., Salikhov, K.M., Kalinina, K.V., Kizhaev, S.S. & Chernyaev, A.V. Super low power consumption middle infrared LED-PD optopairs for chemical sensing. *Proc. SPIE* **8982**, 89821A (2014).

250. Guler, U., Boltasseva, A. & Shalaev, V.M. Refractory Plasmonics. *Science* **344**, 263-264 (2014).

251. Sundqvist, B. Thermal-Diffusivity and Thermal-Conductivity of Chromel, Alumel, and Constantan in the Range 100-450-K. *J. Appl. Phys.* **72**, 539-545 (1992).

252. Incropera, F.P., DeWitt, D.P., Bergman, T.L. & Lavine, A.S. Fundamentals of Heat and Mass Transfer. (2007).

253. Stoyanov, N.D., Salikhov, K.M., Kalinina, K.V., Kizhaev, S.S. & Chernyaev, A.V. Super low power consumption middle infrared LED-PD optopairs for chemical sensing. *Proceedings of SPIE - The International Society for Optical Engineering* **8982**, 89821A (2014).

254. Jain, S.C., McGregor, J.M. & Roulston, D.J. Band-gap narrowing in novel III-V semiconductors. *J. Appl. Phys.* **68** (1990).

255. Snyder, P.G., Woollam, J.A., Alterovitz, S.A. & Johs, B. Modeling AlxGa1-xAs optical constants as functions of composition. *J. Appl. Phys.* **68**, 5925-5926 (1990).

256. Madelung, O. Semiconductors: Data Handbook. (2004).

257. Fu, C.J. & Zhang, Z.M. Nanoscale radiation heat transfer for silicon at different doping levels. *Int. J. Heat Mass Transfer* **49**, 1703-1718 (2006).

258. Whittaker, D.M. & Culshaw, I.S. Scattering-matrix treatment of patterned multilayer photonic structures. *Physical Review B* **60**, 2610-2618 (1999).

259. St-Gelais, R., Zhu, L., Fan, S. & Lipson, M. Near-field radiative heat transfer between parallel structures in the deep subwavelength regime. *Nature Nanotechnology* **11**, 515 (2016).

260. GeFmont, B.L., Sokolova, Z.N. & Yassievich, I.N. *Sov. Phys. Semicond.* **16**, 592-600 (1982).

261. Vining, C.B. An inconvenient truth about thermoelectrics. *Nat. Mater.* **8**, 83-85 (2009).